Time-delay estimation and source localization in radar systems

Jingjing Pan

UNIVERSITE BRETAGNE LOIRE / MATHSTIC

UNIVERSITÉ DE NANTES

THÈSE DE DOCTORAT DE

L'UNIVERSITE DE NANTES

COMUE UNIVERSITÉ BRETAGNE LOIRE

ECOLE DOCTORALE N° 601
Mathématiques et Sciences et Technologies de l'Information et de la Communication
Spécialité : Electronique

Par

Jingjing PAN

Time-delay estimation and source localization in radar systems

Thèse présentée et soutenue à Nantes, le 10 Juillet 2018
Unité de recherche : IETR UMR 6164

Rapporteurs avant soutenance :

Salah BOURENNANE Professeur, École Centrale Marseille
Pascal LARZABAL Professeur, Université Paris Sud

Composition du Jury :

Président :
Jean-Pierre CANCES Professeur, Université de Limoges

Autres membres :
Salah BOURENNANE Professeur, École Centrale Marseille
Pascal LARZABAL Professeur, Université Paris Sud

Directeur de thèse
Yide WANG Professeur, Université de Nantes
Encadrant
Cédric LE BASTARD Chargé de recherche, HDR, Cerema

Acknowledgments

I think I will never forget my first talking with my co-supervisor, Dr. Cédric Le Bastard at IGARSS 2014, when I was still in my master. Now, four year later, in 2018, it is time to finish my Ph.D thesis. Time just flows. I meet many people and experience a lot during these years. Here, I would like to write down something and express all my feelings and gratitudes.

Firstly, I would like to thank my supervisor, Professor Yide Wang, for accepting me as one of his students. I am also grateful to my co-supervisor, Cédric Le Bastard, for his offer to work with him just after IGARSS 2014. Without their professional instruction and warm encouragement, I must have been lost in my early days of Ph.D. I also benefit a lot from their insightful discussions, critical remarks, and patient corrections. It is a pleasure to work with them.

I also would like to express my appreciation to my committee members, Professor Salah Bourennane, Professor Pascal Larzabal, and Professor Jean-Pierre Cances, for their agreements to review my thesis and their participation in the oral defense. I would like to thank them for their valuable comments and feedbacks.

I would like to thank Dr. David Guilbert, Dr. Jean-Michel Simonin, Dr. Vincent Baltazart, and Dr. Xavier Dérobert for the experimental data.

Moreover, I would like to thank Mrs. Sandrine Charlier, Mr. Marc Brunet, and Mr. Guillaume Lirzin for their administrative and technical supports to our research.

During these years, I have many colleagues that enrich my academic life. They are Simei Yang, Ali Mohydeen, Parth Raj Singh, Christophe Bouguet, Irfan Ali Tunio, Yunniel Arencibia Noa, Zhe Fu, Ziwei Xu, Nabil Zaraneh, Taoufik Bouguera, Randa Jaouadi, Julien Weckbrodt, David Roszczypala, Jiajun Pan, Xiao Yangw, Hai Dang Vu, Tien Thanh Nguyen, Jinze Du and the others. We talk about not only academic issues but also a variety of topics. I would like to thank them for bringing about much brightness to my daily life. Special thanks go to Simei Yang for the days that we cook together, travel together, comfort

each other in the lonely foreign Ph.D journey.

I would like to thank China Scholarship Council for the financial funding of my research.

I would like to express my gratitude to my family and my parents, for their support in my unending study. Particularly, I would like to thank my fiancé, Dr. Meng Sun. During these years, whatever happens, he is always there for me.

In the end, I would like to use part of the lyrics of 'Everglow' by Coldplay, which has always reminded me of the people here and the past time:

"Well, they say people come
say people go
This particular diamond was extra special
And though you might be gone, and the world may not know
Still I see you, celestial"

Résumé étendu (French extended abstract)

Introduction

Le traitement d'antenne multicapteurs ainsi que le traitement du signal radar ont beaucoup d'applications pratiques.

Le traitement d'antenne multicapteur peut e utilisec diffnts types d'ondes telles que les ondes sismiques, acoustiques, ctromagnques ou ultrasoniques. Les applications possibles en traitement d'antenne multicapteurs sont nombreuses. On peut en citer quelques-unes comme l'astronomie, les tcommunications (communications sans fil), les raux de microphone, localisation de l'centre d'un tremblement de terre, la location de vide naturel ou enthropique, l'imagerie mcale, la localisation d'objets ou de raux enterr l'imagerie subsurface, etc. Les signaux issus d'un rau de capteurs formant une antenne livrent les informations recherch sur le champ d'onde crar les sources. Ce traitement permet ainsi de dcter et de localiser des tteurs par rapport au rau d'antennes. Dans cette thtique, nous nous sommes principalement intss l'application de l'antenne multicapteurs aux ondes ctromagnques et ceci dans le contexte des tcommunications et du ge civil. A ce jour, de nombreux progront encore attendus en traitement d'antenne multicapteur (tels que la rction de la complexitlculatoire des modes existantes, l'amoration de la rlution et de la prsion des modes), et ceci notamment dans un contexte de sources cohntes. L'objectif de cette th est alors de riser de la localisation de sources, d'objet en champ lointain et/ou en champ proche dans un contexte o les signaux sont cohnts, ayant un faible nombre d'observations.

Le traitement du signal radar s'intsse mesure de l'amplitude des os rodiffusinsi qu'aux temps de retard de ces os. Dans le contexte d'luation et de contrle non destructif (E&CND), le radar, et plus particuliment le radar ghysique, utilise les propris de propagation des ondes ctromagnques (EM) pour drminer la gie et la structure d'un milieu dictrique sondlle

permet ainsi de dcter, de localiser, de caractser et d'identifier des objets ou couches inteur de ce milieu. Ainsi, les permittivitelatives et les isseurs des diffntes couches d'un milieu peuvent e estim. Dans cette thtique, nous nous sommes intss l'auscultation des chauss par radar ghysique pour estimer des isseurs fines. Plus particuliment, nous nous sommes intss l'estimation des temps de retards des os rodiffusans une configuration de mesure en champ lointain et dans le contexte o les signaux sont cohnts et mng. A ce jour, de nombreux progront encore attendus avec le radar ghysique (tels que la rction de la complexitlculatoire des modes existantes, l'amoration de la rlution et de la prsion des modes), et ceci lement dans un contexte de sources cohntes.

Ainsi, cette th a pour objectif de proposer et de dlopper de nouvelles modes de traitement (d'antenne multicapteurs et du signal radar) efficace pour des signaux cohnts, ayant un faible nombre d'observations temporelles. Les modes propos dans cette th ont lu en termes de rlution, du rapport signal sur bruit et du temps de calcul sur des signaux simult rs.

Mod du signal et algorithme

Tout d'abord, le mod de signal utilisur localiser les sources (estimation des directions d'arriv, DDA) et pour estimer les temps de retard en champ lointain est prntection 2.2). Puis, diffntes modes de la littture bas sur un mod de signal *a priori* sont dites. La mode conventionnelle « formation de voies », qui poss une rlution limitar la taille du rau de capteurs, est prnt Les modes bas sur la prction linre qui ont une rlution plus vue les modes conventionnelles sont lement prnt. De plus, une famille de modes (MUSIC, ESPRIT) exploitant les propris de la dmposition en ments propres de la matrice de covariance des observations est lement dite pour estimer les directions d'arriv. Ces modes us-espaces prntent la caractstique de fournir en termes de rlution, des performances asymptotiques illimit et indndantes du rapport signal sur bruit. Nmoins, ces modes us-espaces ne sont pas applicables directement dans un contexte de sources cohntes. En effet, dans ce contexte, des modes de praitement comme la mode SSP (Spatial smoothing preprocessing) sont nssaires. Ensuite, une mode baseulement sur les donn, une mode d'apprentissage automatique supervisppelVR (pour Support Vector Regression) est prnt Cette mode est dite pour la localisation de sources en champ lointain.

Dans un second temps, le mod de signal ainsi que des modes haute rlution sont prntour localiser les sources en champ proche (section 2.3). En champ lointain, une source est

parameulement par sa direction d'arriv Quand les sources sont proches du rau de capteurs et qu'elles se situent dans une situation de champ proche, cette hypoth n'est plus valide. En effet, dans ce cas, le front d'onde du signal est sphque et deux parames sont alors nssaires pour localiser les sources : la direction d'arrivt la distance entre la source et le rau de capteurs.

De nombreuses modes ont d propos dans la littture pour localiser des sources en champ proche comme par exemple la mode du maximum de vraisemblance et 2D-MUSIC. Ces modes sont caracts par une recherche multidimensionnelle. Ces deux modes possnt alors une complexitlculatoire trmportante. Afin de rire cette complexitlculatoire, plusieurs modes de la littture, comme la mode symique, la mode inter-diagonale et la mode de focalisation ont propos rtir de matrice spfique (ne contenant que l'information direction d'arriv. La recherche des parames timer devient alors monodimensionnelle. Les distances entre les sources et le rau de capteurs sont ensuite estim par des modes us-espaces en utilisant les directions d'arriv prablement estim.

Mode propose localisation de sources en champ lointain

Dans ce chapitre, nous proposons de combiner les thies de la mode SVR et des modes de traitement du signal se de mod de signal *a priori* pour estimer les directions d'arriv dans un contexte o les sources sont cohntes. Nous nous sommes intsslus particuliment aux modes de prction linre (PL). Les modes de prction linre sont capables implicitement de drrr les signaux (gr ur formalisme mathtique). De plus, ces modes possnt aussi une rlution plus grande que les modes conventionnelles. En outre, les modes de prction linre ne nssitent pas de dmposition en ments propres de la matrice de covariance des observations. Cependant, les modes de prction linres ne fonctionnent pas lorsque le nombre d'observations devient faible. La mode SVR a d combinvec plusieurs mods linres, comme par exemple le mod autoressif (AR) ou le mod ARMA (mod autoressif et moyenne mobile). Thiquement, le mod autoressif est proche du mod de prction linre direct (ou avant, forward en anglais) (FLP). Mais la prction linre directe-rograde (ou avant-arri, foward-backward en anglais) donne de meilleures performances que la mode de prction avant. Ainsi, nous proposons de combiner la thie de la SVR avec la thie de la prction linre avant-arri. Pour combiner ces deux modes, les variables complexes sont transform en parties rle et imaginaire. La mode des multiplicateurs de Lagrange et les conditions de Karush-Kuhn-Tucker sont utilis pour rudre le probl d'optimisation. Les performances de la mode proposont lu avec diffntes

simulations. La combinaison de la thie de ces deux familles de modes permet d'amorer la robustesse de l'estimation pour des signaux cohnts, ayant un faible nombre d'observations.

Mode proposour l'estimation des temps de retards avec un radar ghysique

Dans ce chapitre, nous proposons d'ndre la mode proposu chapitre 3 pour l'estimation des temps de retards des os rodiffusvec un radar ghysique dans une configuration de mesure en champ lointain et dans le contexte o les signaux sont cohnts. L'objectif est d'estimer les diffnts temps de retard pour estimer dans un second temps les isseurs des diffntes couches d'un milieu stratifie milieu di auscultns cette th est la chauss Contrairement au chapitre 3, les variables complexes de la mode proposont formul directement dans le domaine complexe avec le calcul de Wirtinger. Ce formalisme permet d'utiliser les donn complexes de mani plus naturelle. Les performances de la mode proposont analys avec des donn simul et expmentales. Le comportement de la mode est analysec deux bases de donn de deux expmentations : la premi en laboratoire sur une dalle en PVC et la deuxi sur une chaussu man de fatigue de l'IFSTTAR. Les rltats de simulations et des expmentations ont montr capacit la mode propos estimer des temps de retard des os rodiffusour des signaux cohnts, ayant un faible nombre d'observations. Une analyse de sensibilits diffnts parames est lement ris

Mode propose localisation de sources en champ proche

Dans le chapitre 5, nous proposons une mode de localisation de sources en champ proche dans le contexte o les sources sont cohntes. Quand les sources sont proches du rau de capteurs et qu'elles se situent alors dans une situation de champ proche, le front d'onde du signal est sphque. Deux parames sont alors nssaires pour localiser les sources : la direction d'arrivt la distance entre la source et le rau de capteurs. Par consent, le dasage entre les sources est un mod non linre. Ainsi, afin de drrr les sources, une technique de focalisation est appliquour transformer le mod de signal de champ proche (dasage non linre) en un mod de signal en champ lointain (dasage linre). Ensuite, les modes de praitement comme SSP peuvent e appliqu pour drrr les sources. Une mode us-espaces (ESPRIT, MUSIC, etc) peut ensuite e utilisour estimer les directions d'arriv La distance entre les sources et le rau de capteurs sont quant le estimar la mode du maximum de vraisemblance en util-

isant les directions d'arriv prablement estim. La mode proposst luvec des simulations en fonction du rapport signal sur bruit et du nombre d'observations.

Conclusion et perspectives

Dans cette th, on se focalise sur la localisation de sources en champ lointain et en champ proche ainsi que l'estimation des temps de retard des os rodiffusn champ lointain. Les objectifs de cette th sont de proposer et dlopper de nouvelles modes de traitement (d'antenne multicapteurs et du signal radar) efficaces pour des signaux cohnts, ayant un faible nombre d'antillons. Les modes propos ont lu en termes de rlution, du rapport signal sur bruit, du nombre d'antillons. et du temps de calcul sur des signaux simult rs.

En perspective s travaux, les modes propos pourront e ndues au radar ghysique ayant plusieurs antennes ttrices et rptrices (configuration MIMO).

De plus, la mode M-SVR pour multiple-output SVR pourra lement e utilisour riser de l'estimation multiparames (par exemple temps de retard et rugosit direction d'arrivt distance).

Contents

List of Figures

List of Tables

Mathematical Notations

a: Scalar

a: Vector

A: Matrix

$(.)^*$: Complex conjugate operator

$(.)^T$: Transpose operator

$(.)^H$: Conjugate transpose operator

B: Frequency bandwidth in GHz

$\Delta\tau$: Time-delay between two echoes in second or nanosecond

Δf: Frequency step in GHz

$E(.)$: Expectation operator

$\|\cdot\|_F$: Frobenius norm

$\Re\{a\}$: Real part of a

$\Im\{a\}$: Imaginary part of a

$\mathbb{R}$: Set of real numbers

$\mathbb{C}$: Set of complex numbers

I: Identity matrix

1: Matrix or vector whose elements are 1

$\hat{.}$: Estimated parameter

$diag[\mathbf{a}]$: Diagonal matrix whose diagonal elements are those of vector **a**

$tr(\mathbf{A})$: Trace of matrix **A**

$\det[\mathbf{A}]$: Determinant of matrix **A**

$\odot$: Hadamard product

$\otimes$: Kronecker product

List of Abbreviations

RADAR: RAdio Detection And Ranging

TDE: Time Delay Estimation

SVM: Support Vector Machine

SVR: Support Vector Regression

SVC: Support Vector Classification

EM: ElectroMagnetic

GPR: Ground Penetrating Radar

DOA: Direction Of Arrival

IFFT: Inverse Fast Fourier Transform

MVDR: Minimum Variance Distortionless Response

LP: Linear Prediction

FLP: Forward Linear Prediction

BLP: Backward Linear Prediction

FBLP: Forward–Backward Linear Prediction

AR: AutoRegressive

ARMA : AutoRegressive Moving Average

MEM: Maximum Entropy Method

ML: Maximum Likelihood

MUSIC: MUltiple SIgnal Classification

ESPRIT: Estimation of Signal Parameters via Rotational Invariance Technique

EVD: Eigen Value Decomposition

PM: Propagator Method

SSP: Spatial Smoothing Preprocessing

MSSP: Modified Spatial Smoothing Preprocessing

ULA: Uniform Linear Array

UCA: Uniform Circular Array

SAP: Sub-Array Processing

AGWN: Additive Gaussian White Noise

QP: Quadratic Programming

PSD: Power Spectrum Density

PSE: Probability of Success Estimation

RMSE: Root Mean Square Error

RRMSE: Relative Root Mean Square Error

SNR: Signal-to-Noise Ratio

KKT: Karush-Kuhn-Tucker

VNA: Vector Network Analyser

1

Introduction

Source localization and time-delay estimation (TDE) are of great importance in practical engineering applications. First, we present the fundamental issue and motivation concerning this topic. Then, we summarize the development of key signal processing techniques in localization and estimation problems. In particular, support vector regression (SVR), a sparse machine learning method, and its implementation in signal processing, are specially reviewed. In the end, the main contributions and the organization of this thesis are provided, which is followed by a list of related publications.

1.1 Issue and motivation

Maxwell's equations published in 1865 lay a solid theoretical foundation for the further research and development of electromagnetic (EM) mechanisms. The history spans more than two centuries and nowadays it is still evolving and active. During World War II (1939-1945), the military applied the radio based radar systems to detect and track enemy aircrafts [1, 2, 3]. The term 'radar' is short for RAdio Detection And Ranging, which also indicates its two main tasks: detecting a target and determining its range.

Apart from the pioneering applications of EM theory in military, it also has numerous brilliant representatives in civil and commercial domains, for example, remote sensing, communication, medical imaging, and ground penetrating radar (GPR). Remote sensing

techniques monitor and measure the EM radiation emitted or reflected by the medium (the earth, the atmosphere, the oceans) using satellites, aircrafts or other instruments with a certain distance [4].

Communication systems transfer information between different points in space or time through EM waves and channels [5]. In medical imaging, EM based equipments like computed tomography (CT), magnetic resonance imaging (MRI), contribute efficiently in the detection of a variety of diseases and the interpretation of physical states [6].

GPR is a non-destructive geophysical technique that uses radar pulses to probe media, including pavements, land mines, buried objects [7, 8]. In civil engineering, the information of the vertical structure of the stratified pavements can be extracted from GPR profiles by means of time-delay estimation and amplitude estimation [9].

Theses applications cover the EM spectrum from low-frequency radio waves to the microwave, infrared, visible, x-ray regions. In general, these applications are either to detect signals or to extract the information within the signals. In this thesis, we deal with the common case of signal detection and parameter estimation problem with radar systems, that is, source localization and TDE (especially with GPR).

In radar systems, a single antenna or an array of antennas are used to collect the information of signals. The field in front of the arrays is composed of three regions: the reactive near-field region, the radiating near-field region (also called as the Fresnel region), and the radiating far-field region [10]. Figure 1.1 demonstrates the filed composition, where D is the aperture of the array and λ is the wavelength. The propagation pattern of EM waves varies in different regions. When a source is in far-field, the wavefront received at the array is assumed to be planar. Nevertheless, in near-field (radiating near-field), the plane wave assumption is no longer valid and the wavefront becomes spherical, which shows high nonlinearity. According to the wave propagation schemes, the information of direction of arrival (DOA) is sufficient in the localization of sources in far-field while in near-field, both DOA and range are necessary. Therefore, the positions of the sources with respect to the antennas and the wave propagation schemes should be considered in source localization problems.

Besides, the received signals might be partially correlated even coherent in practical environments. Two signals are assumed to be coherent if one signal is a scaled and delayed replica of the other [11]. In pavement survey using GPR, the received backscattered echoes are the time-shifted and attenuated replicas of the source signals and hence they are coherent [9, 12]. Smart jammers and the multi-path propagation of EM waves are also factors that

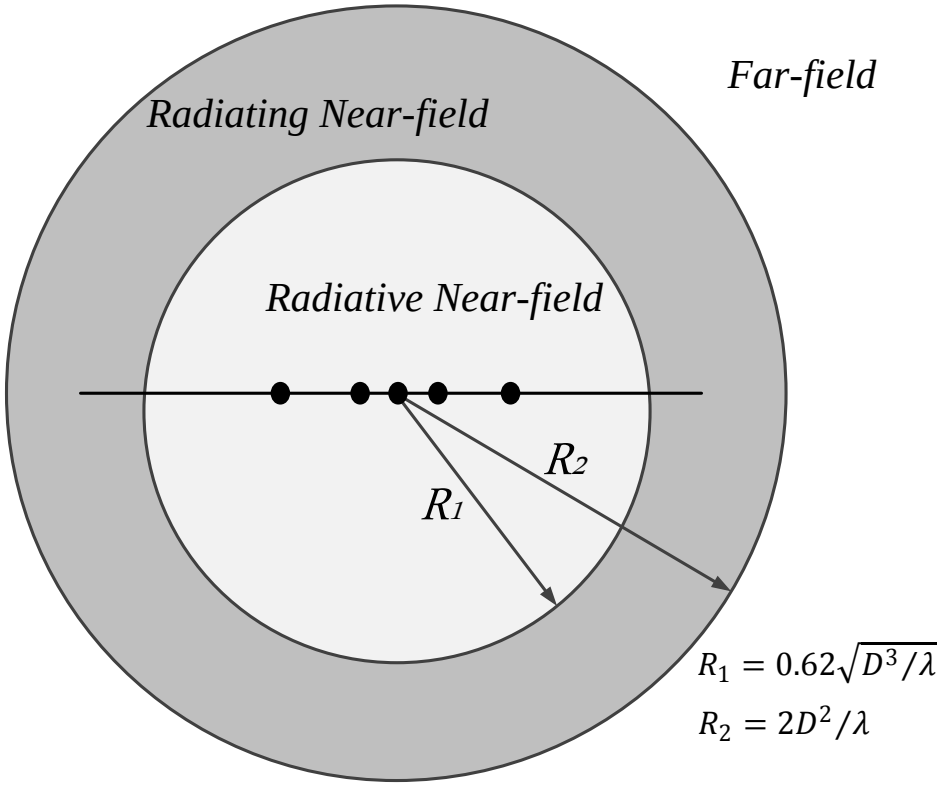

Figure 1.1 – Field composition of array networks.

induce coherency [13]. The coherence between signals degrades the performance of signal processing methods, which adds up to the difficulties in signal detection and estimation, not only in far-field but also in near-field.

Moreover, the performance of source localization and parameter estimation algorithms are affected by imperfect observation [14]. The imperfection can come from the electrical receivers' noise, the environment disturbance, or short observation records. As stated before, the process of signal detection and estimation is to detect and extract the information from the information-bearing signals. A robust signal detection and estimation system against noise, limited observation, and modeling error is therefore important.

An additional problem arises when the signals are too close to each other. In source localization, one goal is to locate closely spaced sources even if they are within the Rayleigh resolution [15]. The same problem exists in TDE when the time-delays are too close. For example, in the probing with GPR of thin pavements, the reflected echoes are overlapped and we can not directly distinguish them. Thus, one of the goals is to improve the resolution of the observation tools. To achieve this goal, we can use more sensors to enlarge the aperture or widen the frequency bandwidth of GPR. However, the improvement of the resolution is more convenient with signal processing algorithms.

1.2 Literature review

This thesis focuses on the source localization (in far-field or near-field) and TDE with high resolution in scenarios where the signals are coherent and the number of snapshots is low.

The signal model in GPR applications is similar to that of source localization in far-field. Therefore, source localization methods in far-field can be applied to TDE. In the following, classical signal processing methods in far-field and near-field will be reviewed and summarized. Furthermore, the applications of SVR, a sparse machine learning method, will be reviewed and discussed in several signal processing problems.

1.2.1 Classical signal processing methods

Fourier-based methods belong to the conventional signal processing methods, for example, classical beamforming [16] for DOA and inverse fast Fourier transform (IFFT) for TDE [9]. However, its performance is limited by the Rayleigh resolution [15]. In order

to go beyond the Fourier limit, Capon beamformer (or minimum variance distortionless response, MVDR) [17] is proposed, which has a better resolution.

Linear prediction (LP) methods are commonly applied in the context of time series analysis. They make use of known observation sequences for the prediction of unknown ones by minimizing the mean square prediction error. In 1967, Burg et al. [18] successfully applied LP theory in the estimation of DOA for the first time, which was also called the maximum entropy method (MEM). Later, there were other developments of LP in source localization and parameter estimation, for example, autoregressive (AR), forward linear prediction (FLP), backward linear prediction (BLP), and forward–backward linear prediction (FBLP) [19, 20]. The principle of AR is closely related to FLP [21]. For comparison, LP methods have higher resolution than conventional signal process methods. They perform spatial smoothing implicitly, which is of great importance with coherent signals [13].

Maximum likelihood (ML) principle has applications in source localization problems. There are two different ML approaches, deterministic maximum likelihood (DML) and stochastic maximum likelihood (SML), according to the assumptions about the emitter signals [15]. The solution of ML leads to a multidimensional (MD) nonlinear optimization problem of which the computational burden is high [15, 22]. But it has asymptotically best performance and can handle not only independent signals but also coherent signals.

In 1979, Schmidt et al. [23] proposed the famous multiple signal classification (MUSIC) method, which opened a new page in the signal processing history with asymptotic infinite resolution and unbiased estimation performance. The principle of MUSIC is based on the assumption of the orthogonality between the noise and signal subspaces. The subspaces are obtained through the eigen value decomposition (EVD) of the covariance matrix of the received signals. However, the implementation of traditional MUSIC has a considerable computational burden through the spectrum searching. A polynomial version of MUSIC, namely, root-MUSIC, was proposed to reduce the computational time in [24]. In 1986, Roy et al. [25] proposed a method exploiting the signal subspace, called as estimation of signal parameters via rational invariance technique (ESPRIT). ESPRIT is a search-free method and its computation burden is close to that of root-MUSIC. There exists also the family of propagator methods (PM) [26]. These methods have high accuracy and resolution. They don't require EVD of the covariance matrix.

Unfortunately, the performance of high resolution methods (MUSIC, ESPRIT, PM, etc) degrades in the presence of highly correlated signals, owing to the rank-loss of the covariance matrix [13, 27, 28].

In 1980s, the spatial smoothing preprocessing (SSP) technique was proposed to restore the rank of covariance matrix in coherent scenarios [13, 29]. Inspired by LP, SSP decorrelates signal by averaging overlapping sub-matrices of covariance matrix. The method in [13, 29] was a single-direction SSP technique in the early stages. Various kinds of improvements were developed thereafter. Like in FBLP, a modified spatial smoothing preprocessing technique (MSSP) was proposed in [30] by making use of forward–backward (FB) submatrices of the covariance matrix to improve the performance of the single-direction one. The authors in [31] developed a computational efficient version of MSSP. In [32], the cross correlation in each sub-matrix was employed along with the auto-correlation information during the processing. The authors in [33] focused on the correlated noise in coherent scenarios using MSSP and spatial differencing method. DOA finding of multi-group coherent signals was considered in [34]. The SSP techniques above were restricted to uniform linear array (ULA) configurations. The authors in [35] presented a modified SSP for uniform circular array (UCA) by transforming the steering vector into a virtual array with Vandermonde structure. The SSP procedure was also extended to other nonlinear configurations of array of antennas by using interpolation [12]. However, SSP suffers aperture loss since the decorrelation is based on the sub-matrices of covariance matrix.

Around 2005, several methods [36, 37] have been proposed to reconstruct new matrices whose ranks are independent of the coherency between signals in the estimation of DOA. In [36], a Toeplitz matrix was reconstructed to estimate DOA. This method is not affected by the coherency and provides satisfactory performance. But it leads to a reduction in array aperture. A non-Toeplitz matrix was introduced in [37] to resolve more sources than the number of sensors under the coexistence of coherent and incoherent signals.

Early implementations of the above signal processing methods (including decorrelation techniques) were dedicated to source localization in far-field. However, near-field source localization is also of high practical importance. In this case, two parameters are necessary: range and DOA. In [38], the extensions of MUSIC and ML were proposed in near-field situations with multidimensional (MD) search (2 dimensional search for MUSIC, 2D MUSIC). The spherical wavefront in near-field has high nonlinearity and the phase shift between elements is nonlinear. For simplification, the nonlinear phase shift expression is approximated by using the second order Taylor series. A lot of methods exploit this approximation and provide good estimation results. In 2005, the authors in [39] presented a weighted linear prediction method, which makes use of the anti-diagonal elements of the covariance matrix. But this method requires the pairing of parameters (both DOA and range). In 2007, the

authors in [40] proposed an efficient near-field source localization method via symmetric sub-arrays without parameter pairing. The symmetric based method requires $K+1$ times 1D search in total, with K the number of sources. However, the maximum number of resolvable sources of [40] in the symmetric based method is N (the ULA is composed of $2N+1$ sensors) [41]. Likewise, in 2012, [42] proposed another $K+1$ times 1D search source localization method. It reconstructed a new matrix with the anti-diagonal elements of the covariance matrix of observations to obtain DOAs. The range of each source can be obtained from the covariance matrix of the whole array and the estimated DOA. This method uses overlapping sub-arrays so that it has reduced aperture. In 2008, the authors in [43] proposed a focusing-based method to transform the near-field signal model into a far-field-like one. This method firstly estimates the DOA of each source and then performs a 1D search with the estimated DOA to obtain the corresponding range. Unlike [40, 42], the focusing-based method doesn't require symmetric array configuration.

The sub-array processing (SAP) technique in [44, 45] also allows to transform the spherical field for the whole array to locally planar field for each sub-array by using array partition. The DOA at each sub-array is estimated with far-field source localization methods. Then, the positions of the sources are obtained with the DOAs at different sub-arrays. The SAP technique works in coherent scenarios. However, the number of array elements should be large because the transform from near-field to far-field greatly reduces the real effective aperture. Besides, SAP can not work with closely located sources.

There are also researches making use of higher order cumulant in source localization problems [46, 47, 48]. The cumulant methods are robust to Gaussian noise and have higher degrees of freedom. However, they are generally more computational expensive than the second-order based methods.

In near-field, the signals are mostly considered as non-coherent in the literature. Conventional far-field decorrelation techniques, like SSP, have limitations in near-field since the phase shifts of signals in near-filed are nonlinear [49].

1.2.2 Support vector regression (SVR)

Support Vector Machine (SVM) is a machine learning method proposed by Vapnik in 1990s [50]. There are two general formulations of SVM: support vector classification (SVC) and support vector regression (SVR). Based on the principle of structural risk minimization, SVM has fantastic generalization ability. They are good sparse machine learning methods able to deal with small samples.

In the literature, SVR has many signal processing applications, which can be classified into two approaches. One is to use the training and testing of SVR to approximate the mapping between the variables to be estimated and known features, which is the typical supervised machine learning process. The features are usually elements of the correlation matrix of the received signals, as in [51, 52, 53, 54]. In this way, models can also be trained off-line to operate efficiently. Details can be found for the estimation of DOA in [51, 52, 53] and time-delay in [54]. The performance of the supervised SVR depends on the learning database.

The other approach combines the theory of SVR with classical signal processing methods. In [55], an SVR-based beamforming method was proposed to control the level of beam sidelobes. Similarly, the authors in [28] combined SVR with Capon and then MUSIC for the estimation of DOA. In coherent scenarios, the proposed method in [28] uses an additional SSP method or a recursive approach. The work in [28] also requires the repetition of the SVR procedure along the DOA spectrum, which needs more computational time.

Besides, there are combinations of SVR with linear signal processing methods. A support vector autoregressive method (AR-SVR) is proposed for frequency estimation problems [56, 57]. The authors in [58] combine autoregressive moving average (ARMA) with SVR for system identification problems.

The theory of SVM is originally developed in the real domain. However, the signals are complex-valued in radar and communication systems. The complex characteristic of signals motivates the complex representation of SVR in signal processing [28, 55, 59]. The complex optimization function of SVR can be formulated in terms of real and imaginary parts [55] or directly in the complex domain [28, 59].

1.3 Main contributions

The main contributions of this thesis are summarized as follows.

1. The first contribution is the formulation of linear SVR equations in the complex domain with Wirtinger's calculus and the quadratic optimization function. We also present the sensitivity analysis of SVR parameters with complex-valued signals (in TDE).

2. The second contribution is the proposal of FBLP-SVR, a combination between SVR and FBLP. Unlike traditional supervised machine learning process (training and testing), we propose to combine the theory of SVR with FBLP in this thesis to calculate

the weight coefficient vector without using covariance matrix of received signals. SVR is a sparse machine learning method and LP methods perform SSP implicitly. The proposed method is applied to estimate DOA in far-field and time-delay. FBLP-SVR shows better performance in the context of low snapshots and coherent signals. Its effectiveness is validated through simulations and experiments.

3. The third contribution is the proposal of near-field source localization method with closely located sources in coherent scenarios. The proposed method firstly uses a focusing technique to transform the near-field situation into far-field. Then, SSP is applied to decorrelate signals and DOA is estimated with a subspace method. From the estimated DOAs, the range of each source is estimated by using ML.

1.4 Thesis organization

The reminder of the thesis is organized as follows. In Chapter 2, we firstly introduce the signal models in far-field and near-field. The signal model to estimate time-delay is also presented, which is very close to the signal model for DOA finding in far-field. Then, the corresponding review of signal processing methods are provided in each field. The theory of SVR is introduced to estimate DOA in far-field by using the supervised learning approach.

Chapter 3 presents the proposed DOA finding method in coherent environment and in far-field. The proposed method combines the theories of SVR and FBLP. FBLP is able to directly deal with coherent signals while SVR is robust with small samples. The proposed method combines the advantages of FBLP and SVR in the estimation of DOA. Its performance is validated with numerical simulations in coherent scenarios, in terms of angle separations, numbers of snapshots, signal-to-noise ratios (SNRs), and steering vector uncertainty. The signals and variables in this chapter are converted from the complex to the real domain for the implementation of SVR. The work in Chapter 3 is published in [60].

In Chapter 4, we propose to extend FBLP-SVR in TDE with GPR signals. Here, SVR is directly formulated in the complex domain with Wirtinger's calculus to deal with complex data in a more natural way. The proposed method is tested with numerical and experimental data in coherent scenarios with overlapping, non-overlapping echoes and limited snapshots. The results demonstrate the effectiveness of the proposed method. The work in Chapter 4 is published in [61].

Chapter 5 presents the localization of two closely located sources in near-field and co-

herent scenarios. The sources in near-field are parameterized with both the DOA and the range. In the proposed method, the estimation of DOA is performed by using the focusing technique, SSP and a subspace method. Then, the range of each source is estimated by using ML with the obtained DOAs. The performance of the proposed method is evaluated with several simulations.

Chapter 6 gives the conclusion, perspectives and future work.

1.5 Publications

Journal

1. Cédric Le Bastard, ***Jingjing Pan***, Yide Wang, et al. A linear prediction and support vector regression based debonding detection method using step-frequency ground penetrating radar. *Submitted to IEEE Geoscience and Remote Sensing Letters*.
2. ***Jingjing Pan***, Cédric Le Bastard, Yide Wang, and Meng Sun. Time-delay estimation using ground-penetrating radar with a support vector regression-based linear prediction method. IEEE Transactions on Geoscience and Remote Sensing, 56(5):2833-2840, 2018. [61]
3. ***Jingjing Pan***, Yide Wang, Cédric Le Bastard, and Tianzhen Wang. DOA finding with support vector regression based forward–backward linear prediction. Sensors, 17(6):1225, 2017. [60]

Conference

1. ***Jingjing Pan***, Yide Wang, Cédric Le Bastard. Support vector regression based linear prediction for direction-of-arrival estimation. The forth Sino-French Workshop on Information and Communication Technologies SIFWICT 2017, June 6, 2017, Qingdao, China.

2

Signal model and algorithms

2.1 Introduction

This chapter presents the signal models for the source localization in far-field and near-field. Then, several signal processing methods are reviewed in each filed. Moreover, the signal model to estimate the time-delay is also presented and compared with that in far-field source localization. Particularly, SVR, a machine learning method, is presented to estimate DOA in far-field.

2.2 Far-field

The assumption for the far-field condition is that the distance between the source and sensors is larger than $2D^2/\lambda$, with D the aperture of the array and λ the wavelength of the imcoming signals. The wavefronts of signals in far-field are considered as planar. In consequence, only DOA is necessary in far-field source localization.

2.2.1 Signal model

Consider a ULA with M isotropic antenna elements, as shown in Figure 2.1. There are K far-field narrow band incoming signals impinging on the sensors, which are corrupted

by an additive Gaussian white noise (AGWN). The output of sensor m can be expressed as:

$$x_m(t) = \sum_{k=1}^{K} s_k(t) e^{-j2\pi \frac{d}{\lambda}(m-1)\sin(\theta_k)} + n_m(t) \tag{2.1}$$

where $s_k(t)$ denotes the kth incoming signal received at the first antenna; θ_k is the corresponding DOA of the kth signal (with respect to the normal line of the array); $n_m(t)$ is the AGWN at the mth antenna with zero mean and variance σ^2; d denotes the distance between two adjacent sensors.

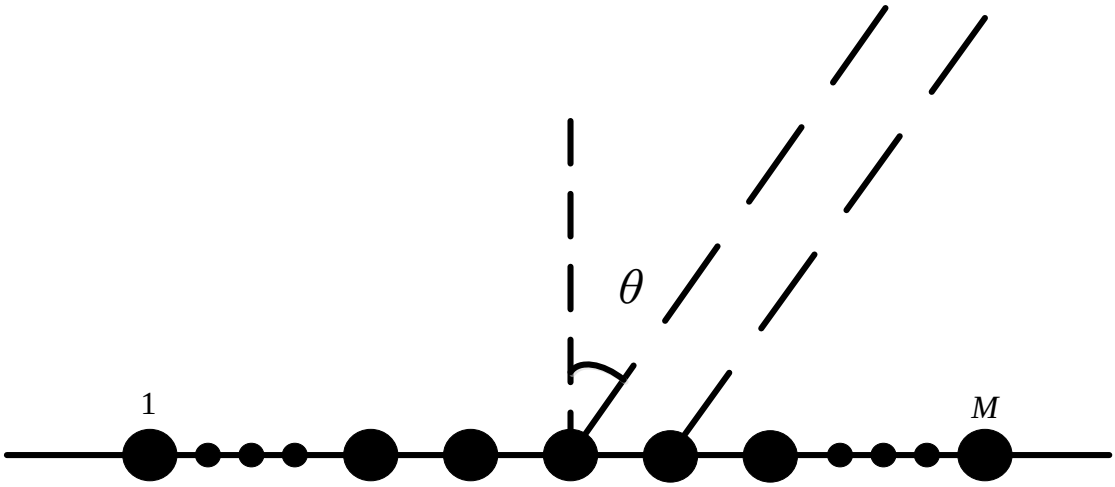

Figure 2.1 – Uniform linear array configuration in far-field source localization.

In vector form, the output of sensors $\mathbf{x}(t) = [x_1(t), \ldots, x_M(t)]^T$ can be formulated as follows:

$$\mathbf{x}(t) = \mathbf{A}\mathbf{s}(t) + \mathbf{n}(t) \tag{2.2}$$

with the following notations:

- $\mathbf{s}(t) = [s_1(t), \ldots, s_K(t)]^T$, is the vector of received signals; the superscript T denotes transpose operation;
- $\mathbf{n}(t) = [n_1(t), \ldots, n_M(t)]^T$, is the noise vector;
- $\mathbf{A}$ is the mode matrix, $\mathbf{A} = [\mathbf{a}(\theta_1), \ldots, \mathbf{a}(\theta_K)]$; each column of $\mathbf{A}$ is given by $\mathbf{a}(\theta_k) = [1, \ldots, e^{-j2\pi \frac{d}{\lambda}(M-1)\sin(\theta_k)}]^T$.

The theoretical covariance matrix is $\mathbf{R} = E[\mathbf{x}(t)\mathbf{x}(t)^H] = \mathbf{A}\mathbf{R}_s\mathbf{A}^H + \sigma^2\mathbf{I}$, where $E[.]$ denotes ensemble average; $\mathbf{R}_s$ is the covariance matrix of the received signals; the superscript H denotes transpose conjugate operation and $\mathbf{I}$ is the $M \times M$ identity matrix.

The exact covariance matrix of received signals in not available in practical applications. But it can be approximated by the sample covariance matrix as follows:

$$\mathbf{R} \approx \frac{1}{L} \sum_{t=1}^{L} \mathbf{x}(t)\mathbf{x}(t)^H. \tag{2.3}$$

where L is the number of snapshots.

The larger the number of snapshots L is, the closer the approximated covariance matrix is to the theoretical one.

Now, we present an extension of the signal model to TDE within a stratified medium. Here, we propose to use GPR to probe the stratified medium, as shown in Figure 2.2.

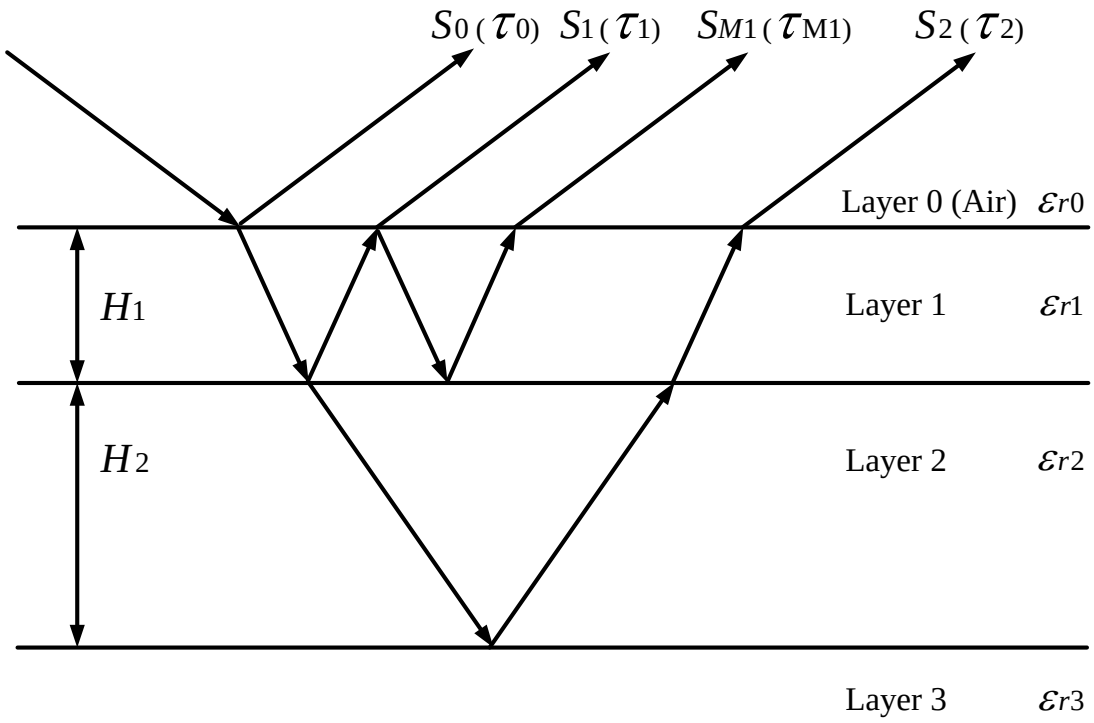

Figure 2.2 – Profile of a stratified medium.

Assume the GPR observations are conducted with M discrete frequencies. The frequency f_m is defined as $f_m = f_1 + (m-1)\Delta f$, with f_1 the beginning of the bandwidth and Δf the frequency difference between two adjacent frequencies, $m = 1, \ldots, M$. The received signal at frequency f_m can be expressed in frequency domain as [9, 62, 63]

$$g_m = \sum_{k=1}^{K} e_m s_k e^{-j2\pi f_m \tau_k} + n_m \tag{2.4}$$

where K is the number of backscattered echoes, which can be primary and multiple reflection echoes; s_k denotes the amplitude of the kth backscattered echo; τ_k is the kth time-delay corresponding to the kth echo; e_m represents the radar pulse in the frequency domain at frequency f_m; n_m is an AGWN with zero mean and variance σ^2.

In frequency bandwidth B, the received backscattered echoes can be written as follows:

$$\mathbf{x} = \mathbf{\Lambda A s} + \mathbf{n} \tag{2.5}$$

with the following notations:

- $\mathbf{x} = [g_1, \ldots, g_M]^T$ is the received GPR signals;
- $\mathbf{s} = [s_1, \ldots, s_K]^T$ is the source vector composed of echo amplitudes;
- $\mathbf{n} = [n_1, \ldots, n_M]^T$ is the complex noise vector;
- $\mathbf{\Lambda} = diag[e_1, \ldots, e_M]$ is a diagonal matrix and the elements are the Fourier transform of the radar pulse;
- $\mathbf{A} = [\mathbf{a}(\tau_1), \ldots, \mathbf{a}(\tau_K)]$ is called mode matrix whose columns are defined as $\mathbf{a}(\tau_k) = \left[e^{-j2\pi f_1 \tau_k}, \ldots, e^{-j2\pi f_M \tau_k}\right]^T$, $k = 1, \ldots, K$.

Table 2.1 shows the summary of the signal models for DOA and TDE in far-field. It is obvious that the variables and expressions of signal models are close to each other. In TDE, M becomes the number of frequencies and K the number of echoes.

Table 2.1 – Summary of signal models in far-field.

	DOA	TDE
Configuration	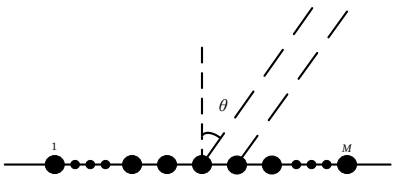	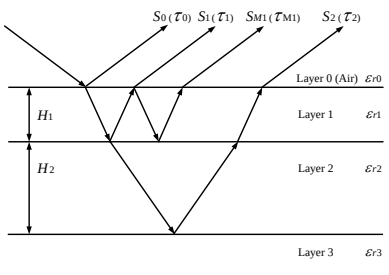
Parameter	θ	τ
Signal Model	$\mathbf{x}(t) = \mathbf{A s}(t) + \mathbf{n}(t)$	$\mathbf{x} = \mathbf{\Lambda A s} + \mathbf{n}$
M	Number of sensors	Number of frequencies
K	Number of sources	Number of echoes

In the following, we will present the signal processing methods only for DOA. But the extensions of the DOA estimation metods to TDE remain valid by taking into account the radar pulse in the model.

2.2.2 Capon beamforming

The objective of Capon beamforming [17] is to minimize the output power with respect to a spatial filter $\boldsymbol{\omega}_{Capon}$, under a unit constraint to the steering direction:

$$\min_{\boldsymbol{\omega}_{Capon}} \ \boldsymbol{\omega}_{Capon}^{H}\mathbf{R}\boldsymbol{\omega}_{Capon} \tag{2.6}$$

$$\text{s. t. } \boldsymbol{\omega}_{Capon}^{H}\mathbf{a}(\theta) = 1.$$

The solution of (2.6) is given by:

$$\boldsymbol{\omega}_{Capon} = \frac{\mathbf{R}^{-1}\mathbf{a}(\theta)}{\mathbf{a}^{H}(\theta)\mathbf{R}^{-1}\mathbf{a}(\theta)}. \tag{2.7}$$

The DOAs can be estimated by searching the following 1D spectrum:

$$P_{Capon}(\theta) = \frac{1}{\mathbf{a}^{H}(\theta)\mathbf{R}^{-1}\mathbf{a}(\theta)}. \tag{2.8}$$

The peak positions indicate the estimated DOAs of the sources.

2.2.3 Linear prediction (LP)

LP is built on a predictive filter and a prediction error filter [27]. The function of the predictive filter is to predict unknown values with known observations while the prediction error filter is to adjust the filter weights according to the errors between the true values and the estimations.

FBLP makes use of the observations from both the forward and backward sensor observation sequences in the estimation. The observation sequence of sensor m with L snapshots can be expressed as follows:

$$\mathbf{r}_m = [x_m(1), x_m(2), \ldots, x_m(L)]^T. \tag{2.9}$$

When the order of the prediction filter is P, the prediction equation can be written in matrix form [19, 27]:

$$\underbrace{\begin{bmatrix} \mathbf{r}_P & \mathbf{r}_{P-1} & \cdots & \mathbf{r}_1 \\ \vdots & \vdots & & \vdots \\ \mathbf{r}_{M-1} & \mathbf{r}_{M-2} & \cdots & \mathbf{r}_{M-P} \\ & \cdots\cdots\cdots\cdots & & \\ \mathbf{r}_2^* & \mathbf{r}_3^* & \cdots & \mathbf{r}_{P+1}^* \\ \vdots & \vdots & \vdots & \\ \mathbf{r}_{M-P+1}^* & \mathbf{r}_{M-P+2}^* & \cdots & \mathbf{r}_M^* \end{bmatrix}}_{\mathbf{Z}} \begin{bmatrix} \omega_1 \\ \omega_2 \\ \vdots \\ \omega_P \end{bmatrix} = \underbrace{\begin{bmatrix} \mathbf{r}_{P+1} \\ \vdots \\ \mathbf{r}_M \\ \cdots \\ \mathbf{r}_1^* \\ \vdots \\ \mathbf{r}_{M-P}^* \end{bmatrix}}_{\mathbf{y}}. \tag{2.10}$$

FLP and BLP can be expressed with the first and second halves (above and below the dotted line) of (2.10), respectively. In a more compact way, (2.10) can be rewritten as:

$$\mathbf{Z}\boldsymbol{\omega}_{FBLP} = \mathbf{y} \tag{2.11}$$

where $\mathbf{y} \in \mathbb{C}^{N_T \times 1}$, $\mathbf{Z} \in \mathbb{C}^{N_T \times P}$ and $\boldsymbol{\omega}_{FBLP} \in \mathbb{C}^{P \times 1}$, $N_T = 2(M-P)L$.

The weight coefficient vector $\boldsymbol{\omega}_{FBLP}$ is estimated by the following least-squares approach:

$$\boldsymbol{\omega}_{FBLP} = \mathbf{R}_{FBLP}^{-1}\mathbf{r}_{FBLP} \tag{2.12}$$

where $\mathbf{R}_{FBLP} = \mathbf{Z}^H\mathbf{Z}/L$ and $\mathbf{r}_{FBLP} = \mathbf{Z}^H\mathbf{y}/L$. The reverse of $\mathbf{R}_{FBLP}$ requires the inequality: $N_T \geqslant P$ so that $\mathbf{R}_{FBLP}$ is a non-singular matrix. Hence we have the constraint for the number of snapshots L: $L \geqslant P/[2(M-P)]$.

According to [19], the order of the prediction filter P should satisfy: $K \leqslant P \leqslant M - K/2$.

With the estimated weight vector $\boldsymbol{\omega}_{FBLP}$, the power spectrum density (PSD) of FBLP can be expressed as:

$$P_{FBLP}(\theta) = \frac{1}{\left| \boldsymbol{a}^H(\theta) \begin{bmatrix} 1 \\ -\boldsymbol{\omega}_{FBLP} \end{bmatrix} \right|^2}. \tag{2.13}$$

Thanks to the mathematical formulation, LP methods are able to decorrelate coherent signals. Besides, they have higher resolution than the conventional Fourier-based methods.

2.2.4 High resolution methods

MUSIC

The general idea of MUSIC is based on the assumption of the orthogonality between the noise subspace and signal subspace. The covariance matrix $\mathbf{R}$ can be formulated in terms of eigenvalues and eigenvectors as follows:

$$\mathbf{R} = \mathbf{U}\boldsymbol{\Sigma}\mathbf{U}^H \tag{2.14}$$

where $\boldsymbol{\Sigma} = diag[\lambda_1, \ldots, \lambda_M]$, a $M \times M$ diagonal matrix with the eigenvalues in descending order ($\lambda_1 \geq \cdots \geq \lambda_K > \lambda_{K+1} = \cdots = \lambda_M = \sigma^2$) and $\mathbf{U} = [\mathbf{u}_1, \ldots, \mathbf{u}_M]$, a $M \times M$ matrix of the corresponding eigenvectors.

Define the first K largest eigenvalues as the signal subspace eigenvalues $\boldsymbol{\Sigma}_s$ and the associated eigenvectors as the signal subspace eigenvectors $\mathbf{U}_s$. Define the rest eigenvalues $\boldsymbol{\Sigma}_n$ and eigenvectors $\mathbf{U}_n$ as the eigenvalues and eigenvectors of the noise subspace, respectively. The matrices $\mathbf{U}$ and $\boldsymbol{\Sigma}$ can be rewritten as:

$$\mathbf{U} = \begin{bmatrix} \mathbf{U}_s & \mathbf{U}_n \end{bmatrix} \tag{2.15}$$

$$\boldsymbol{\Sigma} = \begin{bmatrix} \boldsymbol{\Sigma}_s & \mathbf{0} \\ \mathbf{0} & \boldsymbol{\Sigma}_n \end{bmatrix}. \tag{2.16}$$

According to the above definitions and the properties of EVD, we have:

$$\mathbf{R}\mathbf{U}_n = \sigma^2\mathbf{U}_n = (\mathbf{A}\mathbf{R}_s\mathbf{A}^H + \sigma^2\mathbf{I})\mathbf{U}_n. \tag{2.17}$$

Therefore, we deduce:

$$\mathbf{A}\mathbf{R}_s\mathbf{A}^H\mathbf{U}_n = \mathbf{0}_{K\times(M-K)}. \tag{2.18}$$

Since $\mathbf{A}$ is a Vandermonde matrix and $\mathbf{R}_s$ has full-rank, (2.18) implies:

$$\mathbf{A}^H\mathbf{U}_n = \mathbf{0}_{K\times(M-K)}. \tag{2.19}$$

It is obvious in (2.19) that the noise subspace is orthogonal to the actual steering vector. Consequently, the DOAs can be estimated by searching the peaks of the following 1D

spectrum:

$$P_{MUSIC}(\theta) = \frac{1}{\mathbf{a}^H(\theta)\mathbf{U}_n\mathbf{U}_n^H\mathbf{a}(\theta)}. \tag{2.20}$$

ESPRIT

ESPRIT is developed with two overlapping sub-arrays. The first sub-array is composed of the first $M-1$ sensors in the ULA, while the latter is with the last $M-1$. The corresponding source steering matrices of the two sub-arrays, $\mathbf{A}_1$ and $\mathbf{A}_2$, can be expressed as:

$$\mathbf{A}_1 = \begin{bmatrix} 1 & \dots & 1 \\ \vdots & \vdots & \vdots \\ e^{-j2\pi\frac{d}{\lambda}(M-2)\sin(\theta_1)} & \dots & e^{-j2\pi\frac{d}{\lambda}(M-2)\sin(\theta_K)} \end{bmatrix} \tag{2.21}$$

$$\mathbf{A}_2 = \begin{bmatrix} e^{-j2\pi\frac{d}{\lambda}\sin(\theta_1)} & \dots & e^{-j2\pi\frac{d}{\lambda}\sin(\theta_K)} \\ \vdots & \vdots & \vdots \\ e^{-j2\pi\frac{d}{\lambda}(M-1)\sin(\theta_1)} & \dots & e^{-j2\pi\frac{d}{\lambda}(M-1)\sin(\theta_K)} \end{bmatrix}. \tag{2.22}$$

$\mathbf{A}_1$ and $\mathbf{A}_2$ are related with a diagonal matrix as follows:

$$\begin{aligned} \mathbf{A}_2 &= \mathbf{A}_1 \underbrace{\begin{bmatrix} e^{-j2\pi\frac{d}{\lambda}\sin(\theta_1)} & \dots & 0 \\ \vdots & \vdots & \vdots \\ 0 & \dots & e^{-j2\pi\frac{d}{\lambda}\sin(\theta_K)} \end{bmatrix}}_{\mathbf{\Phi}} \\ &= \mathbf{A}_1\mathbf{\Phi}. \end{aligned} \tag{2.23}$$

The diagonal elements of $\mathbf{\Phi}$ in (2.23) contain all the information about the DOAs.

According to the signal model (2.2), there exists a $K \times K$ full-rank matrix $\mathbf{T}$ satisfying $\mathbf{A} = \mathbf{U}_s\mathbf{T}$. As the whole array is partitioned into two parts, the signal subspace $\mathbf{U}_s$ can be split as:

$$\mathbf{U}_s = \begin{bmatrix} \mathbf{U}_{s1} \\ \text{last row} \end{bmatrix} = \begin{bmatrix} \text{first row} \\ \mathbf{U}_{s2} \end{bmatrix}. \tag{2.24}$$

Likewise, we have:

$$\mathbf{A}_1 = \mathbf{U}_{s1}\mathbf{T} \tag{2.25}$$

and

$$\mathbf{A}_2 = \mathbf{U}_{s2}\mathbf{T}. \tag{2.26}$$

Combining (2.23), (2.25), and (2.26), we have:

$$\begin{aligned}\mathbf{U}_{s2} &= \mathbf{U}_{s1}\underbrace{\mathbf{T}\mathbf{\Phi}\mathbf{T}^{-1}}_{\mathbf{\Psi}} \\ &= \mathbf{U}_{s1}\mathbf{\Psi}.\end{aligned} \tag{2.27}$$

The diagonal matrix $\mathbf{\Phi}$ is composed of the eigenvalues of matrix $\mathbf{\Psi}$. The matrix $\mathbf{\Psi}$ can be obtained by the least-squares approach as follows:

$$\mathbf{\Psi} = (\mathbf{U}_{s1}^H\mathbf{U}_{s1})^{-1}\mathbf{U}_{s1}^H\mathbf{U}_{s2}. \tag{2.28}$$

Then, we can estimate the DOAs through the eigenvalues of $\mathbf{\Psi}$.

Spatial smoothing preprocessing (SSP)

Subspace methods, like MUSIC and ESPRIT, provide unbiased estimation and high resolution. However, the properties of subspace method hold only when the rank of $\mathbf{R}_s$ is K (or $\mathbf{R}_s$ is non-singular). If the input signals are fully correlated, $\mathbf{R}_s$ will be singular and the rank of $\mathbf{R}_s$ is less than the number of sources.

Spatial smoothing preprocessing (SSP) techniques are proposed to solve this problem with overlapping sub-arrays. In general, M identical observing sensors are arranged into Q overlapping subsections. The number of sensors O in each subsection is associated with Q by $Q = M - O + 1$. According to (2.2), the output of the qth subsection can be expressed as:

$$\mathbf{x}_q(t) = \mathbf{A}_M\mathbf{\Phi}^{q-1}\mathbf{s}(t) + \mathbf{n}_q(t),\ q = 1, \ldots, Q \tag{2.29}$$

where $\mathbf{A}_M$ is a $O \times K$ mode matrix and $\mathbf{\Phi} = diag[e^{-j2\pi\frac{d}{\lambda}\sin(\theta_1)}, \ldots, e^{-j2\pi\frac{d}{\lambda}\sin(\theta_K)}]$.

The covariance matrix of the qth subsection is:

$$\mathbf{R}_q = E[\mathbf{x}_q\mathbf{x}_q^H] = \mathbf{A}_M\mathbf{\Phi}^{q-1}\mathbf{R}_s(\mathbf{\Phi}^{q-1})^H\mathbf{A}_M^H + \sigma^2\mathbf{I}_{O\times O}. \tag{2.30}$$

According to [13], the averaged covariance matrix by using SSP can be formulated as:

$$\mathbf{R}_{SSP} = \frac{1}{Q}\sum_{q=1}^{Q}\mathbf{R}_q. \tag{2.31}$$

The forward–backward averaged covariance matrix is expressed as [30]:

$$\mathbf{R}_{MSSP} = \frac{1}{2Q}\sum_{q=1}^{Q}(\mathbf{R}_q + \mathbf{J}\mathbf{R}_q^*\mathbf{J}) \tag{2.32}$$

where $\mathbf{J}$ is the exchange matrix.

With restored rank, the new covariance matrices $\mathbf{R}_{SSP}$, $\mathbf{R}_{MSSP}$ can be applied with subspace methods like MUSIC or ESPRIT to estimate DOAs in coherent scenarios.

2.2.5 SVR (training and learning)

In supervised learning, the objective of the SVR method is to determine the mapping between the variable (for example, θ, τ) and known features. The features can be extracted from the covariance matrix $\mathbf{R}$ as in [51, 52, 53, 54]. $\mathbf{R}$ is a complex hermitian matrix. Therefore, only the upper triangular elements of $\mathbf{R}$ are used to form the feature vector $\mathbf{v}$. In order to apply SVR, each diagonal element is transformed in terms of real and imaginary parts as follows:

$$\begin{aligned}\mathbf{v} = (&\mathbf{R}_{11},\ldots,\mathbf{R}_{MM},\Re(\mathbf{R}_{12}),\ldots,\Re(\mathbf{R}_{(M-1)(M)}),\Re(\mathbf{R}_{13}),\ldots,\Re(\mathbf{R}_{1M}),\\ &\Im(\mathbf{R}_{12}),\ldots,\ \Im(\mathbf{R}_{(M-1)(M)}),\Im(\mathbf{R}_{13}),\ldots,\Im(\mathbf{R}_{1M}))^T\end{aligned} \tag{2.33}$$

where $\Re(.)$ and $\Im(.)$ denote the real and imaginary parts, respectively. The vector $\mathbf{v}$ is normalized to $[0,1]$ for the implementation of SVR.

Given dataset $\{(\mathbf{v}_1,\theta_1),(\mathbf{v}_2,\theta_2),\ldots,\ (\mathbf{v}_n,\theta_n)\}$, the linear regression function for the estimation of DOA can be expressed as:

$$\boldsymbol{\theta} = \mathbf{V}\boldsymbol{\omega} + b \tag{2.34}$$

where $\mathbf{V} = [\mathbf{v}_1^T,\ldots,\mathbf{v}_n^T]^T$, $\mathbf{V}\in\mathbb{R}^{n\times M^2}$; $\boldsymbol{\theta} = [\theta_1,\ldots,\theta_n]^T$, $\boldsymbol{\theta}\in\mathbb{R}^{n\times 1}$; $\boldsymbol{\omega}\in\mathbb{R}^{M^2\times 1}$.

Figure 2.3 gives a simplified example of SVR in x-y plane.

In general, the goal of the regression problem is to obtain two unknown variables $\boldsymbol{\omega}$ and b. In the theory of SVR, two terms are considered in the optimization: the regularization term which indicates the complexity of the model, and the empirical risk term which quantifies the residuals according to the loss-function. The ϵ-intensive loss function is adopted

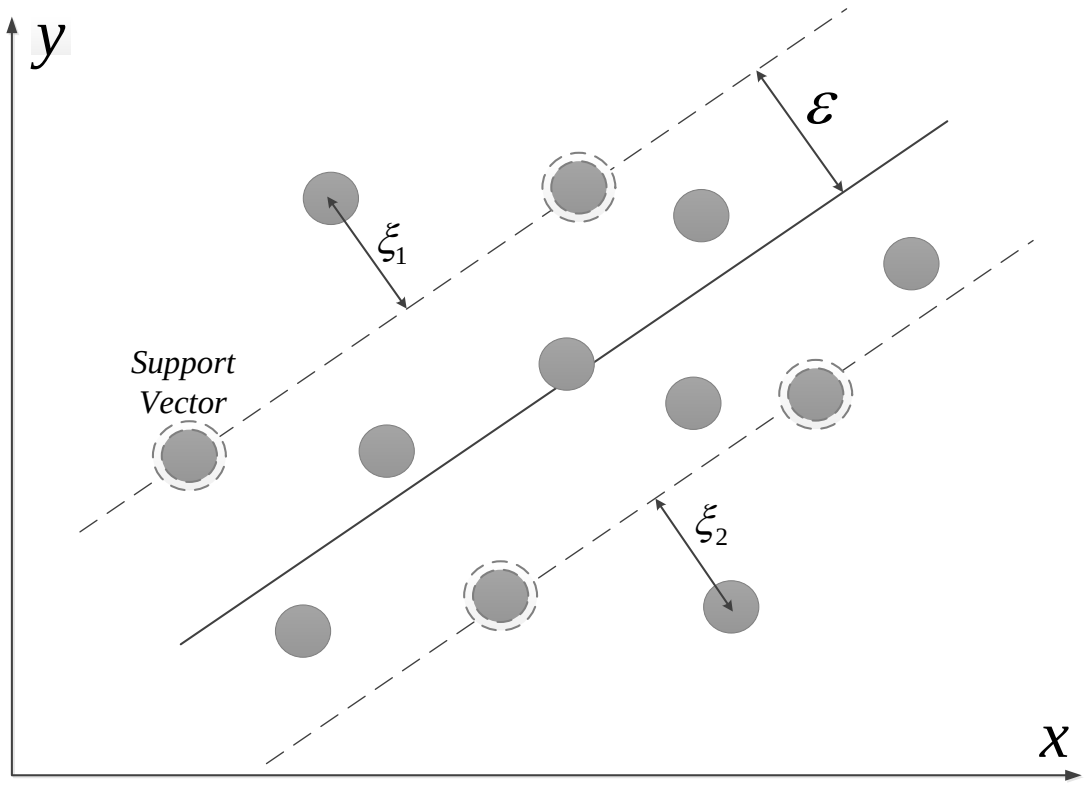

Figure 2.3 – Framework of linear ϵ-SVR in x-y plane. Points with dashed circles represent the support vectors.

here:

$$L_\epsilon(\theta,\hat{\theta}) = \begin{cases} 0 & if|\theta-\hat{\theta}| \leqslant \epsilon \\ |\theta-\hat{\theta}| - \epsilon & otherwise \end{cases} \tag{2.35}$$

The primal optimization problem is to minimize the regression error both structurally and empirically:

$$\min_{\boldsymbol{\omega},b,\boldsymbol{\xi}^{(*)}} L_p = \frac{1}{2}\|\boldsymbol{\omega}\|^2 + C\sum_{i=1}^{n}(\xi_i+\xi_i^*) \tag{2.36}$$

$$\text{s.t.} \begin{cases} \theta_i - \mathbf{v}_i^T\boldsymbol{\omega} - b \leqslant \epsilon + \xi_i, i = 1,\ldots,n \\ -\theta_i + \mathbf{v}_i^T\boldsymbol{\omega} + b \leqslant \epsilon + \xi_i^*, i = 1,\ldots,n \\ \xi_i, \xi_i^* \geqslant 0, i = 1,\ldots,n \end{cases}$$

where $\|.\|$ is the Frobunius norm; ξ_i and ξ_i^* are slack variables to compensate for errors that are larger than the ϵ-tolerance (like the ξ_1 and ξ_2 in Figure 2.3). C is a hyper-parameter which allows to balance the model complexity and the empirical fitting errors.

The solution of (2.36) is to construct a Lagrange function from the objective function and the constraints by introducing a dual set of variables. Therefore, we deduce the following primal–dual objective function

$$\begin{aligned} L_{pd} = \frac{1}{2}\|\boldsymbol{\omega}\|^2 + C\sum_{i=1}^{n}(\xi_i+\xi_i^*) + \sum_{i=1}^{n}\alpha_i(\theta_i - \mathbf{v}_i^T\boldsymbol{\omega} - b - \xi_i - \epsilon) \\ + \sum_{i=1}^{n}\alpha_i^*(-\theta_i + \mathbf{v}_i^T\boldsymbol{\omega} + b - \xi_i^* - \epsilon) - \sum_{i=1}^{n}(\eta_i\xi_i + \eta_i^*\xi_i^*) \end{aligned} \tag{2.37}$$

where α_i, α_i^*, η_i and η_i^* are Lagrange multipliers.

(2.37) is a convex quadratic optimization problem. Thus, there is a saddle point that minimizes the optimization function with respect to the primal variables $\boldsymbol{\omega}, b, \boldsymbol{\xi}^{(*)}$ and maximizes over the dual variables $\boldsymbol{\alpha}^{(*)}$ and $\boldsymbol{\eta}^{(*)}$ [50]. The optimal solution can be obtained according to the Karush-Kuhn-Tucker (KKT) conditions [64]:

$$\begin{cases} \frac{\partial L}{\partial \boldsymbol{\omega}} = \boldsymbol{\omega} - \sum_{i=1}^{n}(\alpha_i - \alpha_i^*)\mathbf{v}_i = 0 \\ \frac{\partial L}{\partial b} = -\sum_{i=1}^{n}(\alpha_i - \alpha_i^*) = 0 \\ \frac{\partial L}{\partial \xi_i^{(*)}} = C - \alpha_i^{(*)} - \eta_i^{(*)} = 0, i = 1,\ldots,n \end{cases} \tag{2.38}$$

According to (2.38), $\boldsymbol{\omega}$ can be reformulated by means of the Lagrange multipliers. Sub-

stituting (2.38) into (2.37), we have the dual optimization problem:

$$L_d = -\frac{1}{2}(\boldsymbol{\alpha} - \boldsymbol{\alpha}^*)^T(\mathbf{V}\mathbf{V}^T + \gamma\mathbf{I})(\boldsymbol{\alpha} - \boldsymbol{\alpha}^*) - \epsilon\mathbf{1}_{n\times 1}^T(\boldsymbol{\alpha} + \boldsymbol{\alpha}^*) + \boldsymbol{\theta}^T(\boldsymbol{\alpha} - \boldsymbol{\alpha}^*) \quad (2.39)$$

$$\text{s. t. } 0 \leqslant \alpha_i,\ \alpha_i^* \leqslant C,\ \sum_{i=1}^{n}(\alpha_i - \alpha_i^*) = 0.$$

where $\boldsymbol{\alpha} = [\alpha_1, \alpha_2, \ldots, \alpha_n]^T$ and $\boldsymbol{\alpha}^* = [\alpha_1^*, \alpha_2^*, \ldots, \alpha_n^*]^T$; $\mathbf{1}_{n\times 1}$ is an all-one column vector with n elements.

In (2.39), $\boldsymbol{\alpha}$ and $\boldsymbol{\alpha}^*$ are the coefficient vectors maximizing the quadratic objective function, which can be calculated using any quadratic programming (QP) solvers. A small identity term $\gamma\mathbf{I}$ is added in the dual objective function in case of ill-conditional matrix of $\mathbf{V}\mathbf{V}^T$ in (2.39) [65]. Then, the variables $\boldsymbol{\omega}$ and b are calculated. Once the model is trained, we can make prediction of DOAs with new inputs. The robustness of the model in the supervised learning process depends on the database.

Nevertheless, the relationship between the variables to be estimated and the features might be nonlinear. In the nonlinear context, we can use kernel functions to transform the data samples into a higher dimensional space without explicit computation of mapping [52, 54]. In this thesis, we mainly deal with linear models.

In the processing of SVR, the data samples are divided into 3 groups, as shown in Figure 2.3. The first group is within the hyperplane (the dashed lines in Figure 2.3). The second and third group are on and outside the hyperplane, respectively. The data points in the first group are also called as 'non-support vectors (nSVs)', which occupy the largest part of the data samples, and the corresponding Lagrange multipliers equal to 0. The samples outside the hyperplane, or 'standard support vectors', contribute to the residuals, and their Lagrange multipliers are C. Only a small number of data samples are on the boundary, like the points with dashed circles in Figure 2.3. These data samples are the 'support vectors (SVs)', which construct the framework of SVR. Thanks to the sparsity of the SVs, this method is of great beneficial in modeling.

2.2.6 Summary

Table 2.2 summarizes the source localization methods in far-field in terms of resolution, decorrelation ability, and method computation.

Table 2.2 – Summary of source localization methods in far-field.

	Main methods	Resolution	Coherent signals	Computation
Conventional method	beamforming...	Rayleigh resolution	Yes	1D search
Super resolution	LP...	<Rayleigh resolution	Yes	1D search
High resolution	MUSIC	Asymptotic resolution	No	EVD, 1D search
	ESPRIT...			EVD
Supervised learning	SVR...	Depend on the database	Yes	Training, testing

2.3 Near-field

We have seen that if the distance between the source and the observation array is larger than $2D^2/\lambda$, the source is in far-field. If the distance is within $\mathbf{r}_F = [0.62(D^3/\lambda)^{1/2},\ 2D^2/\lambda]$, the source is considered as in near-field. The near-field in this thesis refers to the radiating near-field in Figure 1.1. In this region, the wavefronts are spherical and two parameters are necessary to localize the source: DOA and range.

2.3.1 Signal model

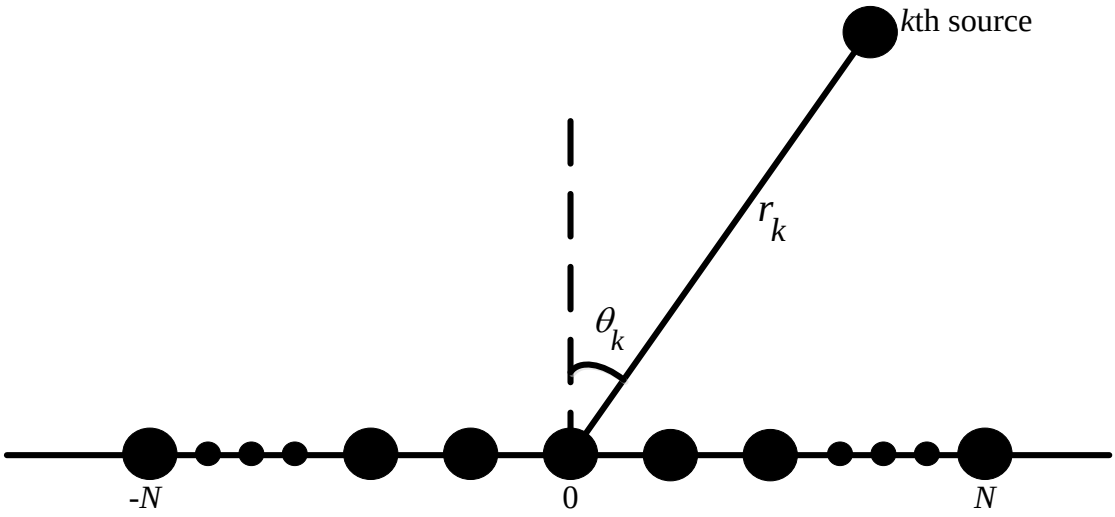

Figure 2.4 – Uniform linear array configuration in near-field source localization.

Consider K sources in near-field in incoherent scenarios and a ULA with $M = 2N + 1$

elements, as shown in Figure 2.4. The sensors are indexed as $-N, \ldots, N$. The distance between two adjacent elements is d. Taking the 0th element of ULA as reference, the received output of the ith sensor can be expressed as:

$$x_i(t) = \sum_{k=1}^{K} s_k(t) e^{j\phi_{ik}} + n_i(t), t = 1, \ldots, L \tag{2.40}$$

where $i \in [-N, N]$, $n_i(t)$ is the AGWN at the ith sensor with zero mean and variance σ^2, $s_k(t)$ is the signal emitted from the kth source and received by the 0th sensor. ϕ_{ik} is the phase difference of signal $s_k(t)$ between sensor i and 0, which can be expressed as:

$$\phi_{ik} = \frac{2\pi}{\lambda}(\sqrt{r_k^2 + (id)^2 - 2r_k id \sin(\theta_k)} - r_k) \tag{2.41}$$

with θ_k the DOA of the kth source and r_k the range of the kth source with respect to the reference point.

The phase shift ϕ_{ik} in (2.41) is a nonlinear function of the source parameters r_k and θ_k, which can be approximated by the second-order Tayler expansion:

$$\phi_{ik} = (-2\pi \frac{d \sin(\theta_k)}{\lambda}) i + (\frac{\pi d^2}{\lambda r_k} \cos^2 \theta_k) i^2 + o' \tag{2.42}$$

where o' is the remainder of the Taylor series.

With the previous expressions, the output of sensors $\mathbf{x}(t) = [x_{-N}(t), \ldots, x_N(t)]^T$ can be written in vector form as:

$$\mathbf{x}(t) = \mathbf{A}\mathbf{s}(t) + \mathbf{n}(t) \tag{2.43}$$

where $\mathbf{s}(t) = [s_1(t), \ldots, s_K(t)]^T$ is the received signal vector; $\mathbf{n}(t) = [n_{-N}(t), \ldots, n_N(t)]^T$ is the noise vector; $\mathbf{A}$ is the mode matrix given by $\mathbf{A} = [\mathbf{a}(r_1, \theta_1), \ldots, \mathbf{a}(r_K, \theta_K)]$, with the steering vector $\mathbf{a}(r_k, \theta_k)$:

$$\begin{aligned} \mathbf{a}(r_k, \theta_k) &= \begin{bmatrix} a_{k,-N} \\ \vdots \\ a_{k,N} \end{bmatrix} \\ &= \begin{bmatrix} e^{j(2\pi \frac{d}{\lambda} \sin\theta_k)N + j(\frac{\pi d^2}{\lambda r_k} \cos^2 \theta_k)N^2} \\ \vdots \\ e^{j(2\pi \frac{d}{\lambda} \sin\theta_k)(-N) + j(\frac{\pi d^2}{\lambda r_k} \cos^2 \theta_k)N^2} \end{bmatrix}. \end{aligned} \tag{2.44}$$

The covariance matrix of the received signals is $\mathbf{R} = E[\mathbf{x}(t)\mathbf{x}^H(t)] = \mathbf{A}\mathbf{R}_s\mathbf{A}^H + \sigma^2\mathbf{I}$. For non-coherent sources, the EVD of $\mathbf{R}$ yields:

$$\mathbf{R} = \mathbf{U}_s\mathbf{\Sigma}_s\mathbf{U}_s^H + \mathbf{U}_n\mathbf{\Sigma}_n\mathbf{U}_n^H \tag{2.45}$$

where $\mathbf{\Sigma}_s$ contains the K largest eigenvalues of $\mathbf{R}$, and $\mathbf{U}_s$ contains the corresponding eigenvectors spanning the signal subspace of $\mathbf{R}$; $\mathbf{\Sigma}_n$ contains the rest $M-K$ eigenvalues, while $\mathbf{U}_n$ contains the corresponding eigenvectors spanning the noise subspace.

2.3.2 Maximum likelihood (ML)

Under the Gaussian hypothesis, the probability density function of the observation $\mathbf{x}(t)$ can be formulated as [66]:

$$p(\mathbf{A}, \mathbf{s}(t), \sigma^2) = \frac{1}{\pi \det[\sigma^2\mathbf{I}]} \exp\left[-\|\mathbf{x}(t) - \mathbf{A}\mathbf{s}(t)\|^2/\sigma^2\right] \tag{2.46}$$

where $\det[.]$ denotes the determinant.

Since the observations are independent and identically distributed (i.i.d.) random variables, the likelihood function of the L snapshots is:

$$f(\mathbf{A}, \mathbf{s}(t), \sigma^2) = \prod_{t=1}^{L} \frac{1}{\pi \det[\sigma^2\mathbf{I}]} \exp\left[-\|\mathbf{x}(t) - \mathbf{A}\mathbf{s}(t)\|^2/\sigma^2\right]. \tag{2.47}$$

The log likelihood function of (2.47) (ignoring constant terms) is:

$$g(\mathbf{A}, \mathbf{s}(t), \sigma^2) = -LM\log\sigma^2 - \frac{1}{\sigma^2}\sum_{t=1}^{L}\|\mathbf{x}(t) - \mathbf{A}\mathbf{s}(t)\|^2. \tag{2.48}$$

The objective of ML is to maximize the likelihood function g with respect to all unknowns. Fixing $\mathbf{A}$ and $\mathbf{s}(t)$ and maximizing g with respect to σ^2, we deduce:

$$\hat{\sigma}^2 = \frac{1}{LM}\sum_{t=1}^{L}\|\mathbf{x}(t) - \mathbf{A}\mathbf{s}(t)\|^2. \tag{2.49}$$

Substituting (2.49) into (2.48), we get:

$$\max_{\mathbf{A},\mathbf{s}(t)} -LM\log\left(\frac{1}{LM}\sum_{t=1}^{L}\|\mathbf{x}(t) - \mathbf{A}\mathbf{s}(t)\|^2\right). \tag{2.50}$$

In fact, (2.50) is equivalent to the following minimization problem:

$$\min_{\mathbf{A},\mathbf{s}(t)} \sum_{t=1}^{L} \|\mathbf{x}(t) - \mathbf{A}\mathbf{s}(t)\|^2 \tag{2.51}$$

which is actually a classical least-squares problem.

To find the optimal solution, we fix $\mathbf{A}$ and minimize (2.51) with respect to $\mathbf{s}(t)$ and we deduce:

$$\hat{\mathbf{s}}(t) = (\mathbf{A}^H\mathbf{A})^{-1}\mathbf{A}^H\mathbf{x}(t). \tag{2.52}$$

Substituting (2.52) into (2.51), we obtain the following minimization task:

$$\min_{\mathbf{A}} \sum_{t=1}^{L} \|\mathbf{x}(t) - \mathbf{A}(\mathbf{A}^H\mathbf{A})^{-1}\mathbf{A}^H\mathbf{x}(t)\|^2. \tag{2.53}$$

Considering the properties of Frobenius norm, we have a more suitable expression of (2.53) as follows

$$\max_{\mathbf{A}} \; tr(\mathbf{\Pi}_\mathbf{A}\mathbf{R}) \tag{2.54}$$

where $\mathbf{\Pi}_\mathbf{A} = \mathbf{A}(\mathbf{A}^H\mathbf{A})^{-1}\mathbf{A}^H$; $tr(.)$ is the trace operator.

Theoretically, the solution of ML belongs to a multidimensional nonlinear optimization problem. The range and DOA of each source can be estimated with a searching procedure. However, the matrix $\mathbf{A} = [\mathbf{a}(r_1, \theta_1), \ldots, \mathbf{a}(r_K, \theta_K)]$ is composed of $2K$ unknowns and $r_k \in \mathbf{r}_F$, $\theta_k \in [-\pi/2, \pi/2]$, $k = 1, \ldots, K$. The search with $2K$ dimensions is computational demanding. However, ML can deal with coherent signals.

2.3.3 2D MUSIC

The extension of MUSIC in near-field is also based on the orthogonality property between the signal steering vector and the noise eigenvectors. Since the signal steering vector is parameterized with two variables, range and DOA, the estimation of sources should be conducted in two dimensions, which is called as 2D MUSIC [38]. The searching spectrum of 2D MUSIC is defined as follows:

$$P_{MUSIC}(\theta, r) = \frac{1}{\mathbf{a}(r, \theta)^H\mathbf{U}_n\mathbf{U}_n^H\mathbf{a}(r, \theta)} \tag{2.55}$$

where $\theta \in [-\pi/2, \pi/2]$ and $r \in \mathbf{r}_F$.

Figure 2.5 shows an example of near-field source by using 2D MUSIC. The two peaks indicate their positions.

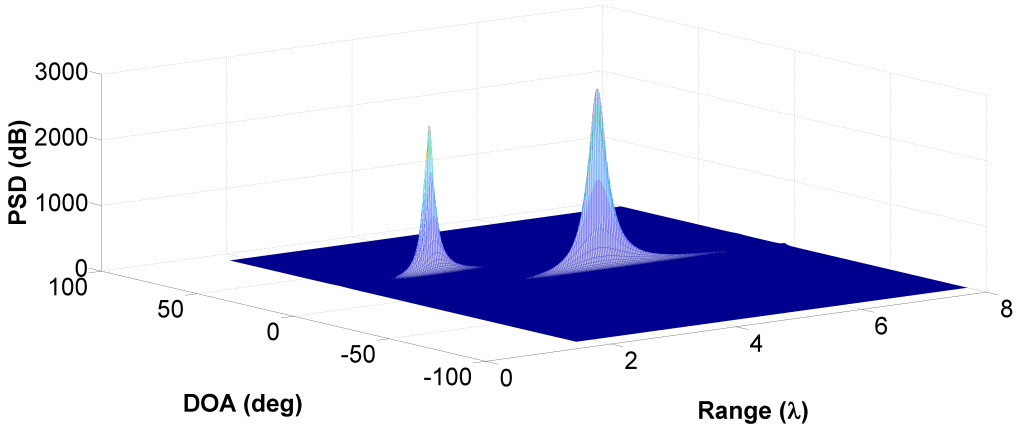

Figure 2.5 – An example of near-field source localization by using 2D MUSIC.

2.3.4 Symmetric method

The authors in [40] propose a symmetric-based method in near-field source localization problems. The whole array is partitioned into two sub-arrays. Each sub-array contains O elements, $K < O < 2N + 1$. Sub-array 1 consists of sensor $-N$ to sensor $-N + O - 1$. Sub-array 2 is made up of sensor N to sensor $N - O + 1$. Therefore, the received signal vectors of sub-arrays 1 and 2 can be written as:

$$\begin{aligned} \mathbf{x}_1(t) &= [x_{-N}(t), \ldots, x_{-N+O-1}(t)]^T \\ &= \mathbf{A}_1\mathbf{s}(t) + \mathbf{n}_1(t) \end{aligned} \tag{2.56}$$

$$\begin{aligned} \mathbf{x}_2(t) &= [x_{N}(t), \ldots, x_{N-O+1}(t)]^T \\ &= \mathbf{A}_2\mathbf{s}(t) + \mathbf{n}_2(t) \end{aligned} \tag{2.57}$$

where $\mathbf{n}_1 = [n_{-N}(t), \ldots, n_{-N+O-1}(t)]^T$, $\mathbf{n}_2 = [n_N(t), \ldots, n_{N-O+1}(t)]^T$ are the noise vectors of sub-arrays 1 and 2, respectively; $\mathbf{A}_1$ and $\mathbf{A}_2$ are the corresponding steering matrices.

Let $\mathbf{A}_1 = [\mathbf{a}_1(r_1, \theta_1), \ldots, \mathbf{a}_1(r_K, \theta_K)]$ and $\mathbf{a}_1(r_k, \theta_k) = [a_{k,-N}, \ldots, a_{k,-N+O-1}]^T$. The symmetric property gives:

$$\mathbf{A}_2 = [\mathbf{D}(\theta_1)\mathbf{a}_1(r_1, \theta_1), \ldots, \mathbf{D}(\theta_K)\mathbf{a}_1(r_K, \theta_K)] \tag{2.58}$$

with $\mathbf{D}(\theta_k) = diag[e^{-j(4\pi\frac{d}{\lambda}\sin\theta_k)N}, \ldots, e^{-j(4\pi\frac{d}{\lambda}\sin\theta_k)(N-O+1)}]$.

Similarly, there exists a $K \times K$ full-rank matrix $\mathbf{G}$ satisfying $\mathbf{U}_s = \mathbf{AG}$. The partitioned signal subspaces $\mathbf{U}_{s1}$ and $\mathbf{U}_{s2}$ can be expressed as:

$$\mathbf{U}_{s1} = \mathbf{A}_1\mathbf{G} \tag{2.59}$$

and

$$\mathbf{U}_{s2} = \mathbf{JA}_2\mathbf{G}. \tag{2.60}$$

Define $\mathbf{F}(\theta)$ as follows:

$$\mathbf{F}(\theta) = \mathbf{JU}_{s2} - \boldsymbol{\psi}(\theta)\mathbf{U}_{s1} \tag{2.61}$$

where $\boldsymbol{\psi}(\theta) = diag[e^{-j(4\pi\frac{d}{\lambda}\sin\theta)N}, \ldots, e^{-j(4\pi\frac{d}{\lambda}\sin\theta)(N-O+1)}]$.

Accordingly, the kth column of $\mathbf{F}(\theta)$ will reach zero when $\theta = \theta_k$. Therefore, we can find the DOAs by searching the following spectrum:

$$P(\theta) = \frac{1}{\det[\mathbf{F}(\theta)^H\mathbf{F}(\theta)]}. \tag{2.62}$$

The peaks of $P(\theta)$ represent the estimated angle $\hat{\theta}_k$, $k = 1, \ldots, K$.

The range of each source r_k can be estimated by using MUSIC and the estimate $\hat{\theta}_k$:

$$\hat{r}_k = \arg\max_{r\in\mathbf{r}_F} \frac{1}{\mathbf{a}^H(r,\hat{\theta}_k)\mathbf{U}_n\mathbf{U}_n^H\mathbf{a}(r,\hat{\theta}_k)},\ k = 1, \ldots, K. \tag{2.63}$$

For K sources, this method needs $K + 1$ 1D search. Besides, the maximum number of detectable sources is N [41].

2.3.5 Anti-diagonal method

The authors in [42] use the anti-diagonal elements of $\mathbf{R}$ for the estimation of DOAs in near-field source localization. Without noise, the (i, j)th element of $\mathbf{R}$, $r(i, j)$, can be expressed as:

$$\begin{aligned} r(i,j) &= E[x_i(t)x_j^*(t)] = E[\sum_{k=1}^{K} s_k(t)a_i(r_k,\theta_k) \times \sum_{k=1}^{K} s_k^*(t)a_j^*(r_k,\theta_k)] \\ &= \sum_{k=1}^{K} \delta_{sk}^2 a_i(r_k,\theta_k)a_j^*(r_k,\theta_k) \end{aligned} \tag{2.64}$$

where $a_i(r_k, \theta_k)$ is the (i, j)th element of the mode matrix $\mathbf{A}$; δ_{sk}^2 is the power of the kth source.

According to (2.64) and the symmetric property of the array configuration, the anti-diagonal elements of $\mathbf{R}$ can be written as:

$$r(i, 2N + 2 - i) = \sum_{k=1}^{K} \delta_{sk}^2 e^{-j(N+1-i)2w_k}, \; i = 1, \ldots, 2N + 1 \tag{2.65}$$

where $w_k = -2\pi \frac{d}{\lambda} \sin(\theta_k)$.

Thus, we can form a $(2N + 1) \times 1$ vector with all the anti-diagonal elements as follows:

$$\mathbf{y} = [r(1, 2N + 1), \ldots, r(2N + 1, 1)]^T = [\sum_{k=1}^{K} \delta_{sk}^2 e^{-jN2w_k}, \ldots, \sum_{k=1}^{K} \delta_{sk}^2 e^{jN2w_k}]^T. \tag{2.66}$$

Divide $\mathbf{y}$ into Q overlapping subsections. Each subsection contains O elements, where $O = M - Q + 1 = 2N + 2 - Q$. Then, the data corresponding to the qth subsection $(q = 1, \ldots, Q)$ can be formulated as:

$$\begin{aligned}
\mathbf{y}_q &= [\mathbf{y}(q), \ldots, \mathbf{y}(q + O - 1)]^T \\
&= [\sum_{k=1}^{K} \delta_{sk}^2 e^{j(q-1-N)2w_k}, \ldots, \sum_{k=1}^{K} \delta_{sk}^2 e^{j(q+N-Q)2w_k}]^T \\
&= \begin{bmatrix} e^{j(-1-N)2w_1} & \ldots & e^{j(-1-N)2w_K} \\ \vdots & \vdots & \vdots \\ e^{j(N-Q)2w_1} & \ldots & e^{j(N-Q)2w_K} \end{bmatrix} \begin{bmatrix} \delta_{s1}^2 e^{jq2w_1} \\ \vdots \\ \delta_{sK}^2 e^{jq2w_K} \end{bmatrix} \\
&= [\mathbf{b}(\theta_1), \ldots, \mathbf{b}(\theta_K)]\mathbf{p}_q \\
&= \mathbf{B}(\theta)\mathbf{p}_q.
\end{aligned} \tag{2.67}$$

A new covariance matrix $\mathbf{R}_y$ is computed by combining the Q subsections:

$$\begin{aligned}
\mathbf{R}_y &= \frac{1}{Q} \sum_{q=1}^{Q} \mathbf{y}_q \mathbf{y}_q^H \\
&= \frac{1}{Q} \sum_{q=1}^{Q} \mathbf{B}(\theta)\mathbf{p}_q \mathbf{p}_q^H \mathbf{B}(\theta)^H.
\end{aligned} \tag{2.68}$$

The DOAs are estimated by searching the peaks of the following spectrum:

$$\hat{\theta}_k = \arg\max_{\theta} \frac{1}{\mathbf{b}^H(\theta)\mathbf{U}_{yn}\mathbf{U}_{yn}^H\mathbf{b}(\theta)} \tag{2.69}$$

where $\mathbf{U}_{yn}$ is the noise subspace of $\mathbf{R}_y$ in (2.68).

The range estimation is the same as in (2.63). Since this method uses subsections, its effective aperture is limited and it can localize N sources at most. To sum up, the anti-diagonal method needs $K+1$ 1D search.

2.3.6 Focusing method

The focusing technique is widely applied in wide band array processing problems. In [43], it is modified for near-field source localization with narrow band signals. In the focusing method, the second term of the phase shift in (2.42) is approximately eliminated by the focusing matrix, which allows to transform the near-field signal model into a far-field-like one. The focusing matrix is obtained from a rough pre-estimation method, for example, beamforming.

Two different cases are considered: the particular case (closely located sources), and the general case (well-separated sources).

Particular case (closely located sources)

Assume K sources are closely located. Let r_e and θ_e be the corresponding pre-estimates of range and DOA. In this case, the second order in (2.42) can be expressed as follows:

$$(\frac{\pi d^2}{\lambda r_1}\cos^2\theta_1)i^2 \approx (\frac{\pi d^2}{\lambda r_k}\cos^2\theta_k)i^2, k = 2, \ldots, K. \tag{2.70}$$

We can build a diagonal focusing matrix $\mathbf{C} \in \mathbb{C}^{M\times M}$ as follows:

$$\mathbf{C} = diag[e^{-j(\frac{\pi d^2}{\lambda r_e}\cos^2\theta_e)(-N)^2}, \ldots, e^{-j(\frac{\pi d^2}{\lambda r_e}\cos^2\theta_e)(N)^2}]. \tag{2.71}$$

The covariance matrix $\mathbf{R}$ is therefore focused as:

$$\begin{aligned}\mathbf{R}' &= \mathbf{C}\mathbf{R}\mathbf{C}^H \\ &= \mathbf{C}(\mathbf{A}\mathbf{R}_s\mathbf{A}^H + \sigma^2\mathbf{I})\mathbf{C}^H \\ &= \mathbf{C}\mathbf{A}\mathbf{R}_s\mathbf{A}^H\mathbf{C}^H + \sigma^2\mathbf{I} \\ &= (\mathbf{C}\mathbf{A})\mathbf{R}_s(\mathbf{C}\mathbf{A})^H + \sigma^2\mathbf{I}.\end{aligned} \tag{2.72}$$

Let $\mathbf{CA} = [\mathbf{Ca}(r_1, \theta_1), \ldots, \mathbf{Ca}(r_K, \theta_K)]$. The kth column of $\mathbf{CA}$, noted $(\mathbf{CA})_k$, is expressed as:

$$\begin{aligned}(\mathbf{CA})_k &= \mathbf{Ca}(r_k, \theta_k) \\ &= \begin{bmatrix} e^{j(2\pi\frac{d}{\lambda}\sin\theta_k)N + j(\frac{\pi d^2}{\lambda r_k}\cos^2\theta_k)N^2 - j(\frac{\pi d^2}{\lambda r_e}\cos^2\theta_e)N^2} \\ \vdots \\ e^{j(2\pi\frac{d}{\lambda}\sin\theta_k)(-N) + j(\frac{\pi d^2}{\lambda r_k}\cos^2\theta_k)N^2 - j(\frac{\pi d^2}{\lambda r_e}\cos^2\theta_e)N^2} \end{bmatrix} \\ &\approx \begin{bmatrix} e^{j(2\pi\frac{d}{\lambda}\sin\theta_k)N} \\ \vdots \\ e^{j(2\pi\frac{d}{\lambda}\sin\theta_k)(-N)} \end{bmatrix}.\end{aligned} \tag{2.73}$$

Consequently, far-field source localization methods in Section 2.2 can be applied to estimate DOA. The range estimation procedure in (2.63) can also be used here.

General case

In general case, the sources might be well separated, and (2.70) is not valid. Then, we can divide the sources into different sub-areas and apply focusing technique to each sub-area separately as in the particular case.

2.3.7 Summary

Table 2.3 shows a summary of source localization methods in near-field concerning the decorrelation ability, method computation.

Table 2.3 – Summary of source localization methods in near-field.

Method	Coherent signals	Computation	Remark
Maximum likelihood	Yes	$(2K)$D search	
2D MUSIC	No	EVD, 2D search	
Symmetric method	No	EVD, $K+1$ 1D search	M odd number, $K \leq N$
Anti-diagonal method	No	EVD, $K+1$ 1D search	M odd number, $K \leq N$
Focusing Method	No	EVD, K 1D search, 2D search	Pre-estimation

2.4 Conclusion

In this chapter, the signal models for far-field and near-field source localization are presented along with several signal processing methods. The signal model for TDE is presented as well. Furthermore, the training and learning process of SVR is introduced in the estimation of DOA. However, most of the summarized signal processing methods depend on the covariance matrix of received signals, which might have unstable results with limited numbers of snapshots. Besides, the coherency between signals introduces additional problems to EVD based methods, not only in far-field but also in near-field. In the following chapters, new signal processing methods will be proposed to deal with coherent signals and low number of snapshots.

3

Proposed DOA estimation method in far-field

3.1 Introduction

In this chapter, we focus on the source localization problem in far-field, especially with coherent signals and limited numbers of snapshots. DOA is an important parameter in identifying the sources in far-field [3, 15]. Subspace methods, like MUSIC, ESPRIT, achieve asymptotically infinite resolution but they cannot be applied directly in coherent scenarios [67]. Additional decorrelation techniques (e.g., SSP) are usually necessary. The family of LP methods performs SSP implicitly and can deal with coherent signals [13, 27]. Besides, they have higher resolution than the conventional Fourier-based approaches and don't require EVD of the covariance matrix of observation. However, LP methods fail to work when the number of snapshots is small [27, 68].

The principle of LP is to find the weight coefficients which minimize the prediction error. SVR is a good sparse machine learning method capable of dealing with small samples [50]. In signal processing, SVR has been used to estimate the coefficients of several linear models, such as AR and ARMA for frequency estimation and system identification problems [58, 65]. In theory, AR is closely related to FLP [21]. FBLP offers better performance

than the one-directional prediction methods (FLP and BLP) [69]. Moreover, there is no explicit work about SVR-based LP models with coherent signals. Therefore, we propose to combine SVR with FBLP in DOA estimation of coherent incoming signals with a small number of snapshots.

The signal model used in this chapter is the signal model presented in Section 2.2.1. The derivations and associated notations of LP in Section 2.2.3 are also adopted.

3.2 Proposed method

As formulated in (2.10)-(2.13), the key issue in LP methods is the estimation of weight vector $\boldsymbol{\omega}_{FBLP}$. However, the classical least-squares solution imposes a constraint on the number of snapshots: $L \geq P/[2(M-P)]$, with L the number of snapshots, M the number of sensors, and P the order of the prediction filter. As a result, in scenarios where the observation is insufficient (i.e., the number of snapshots is too small), LP methods might be unstable (even unsuccessful). Therefore, we propose to use the principle of SVR to deal with limited samples. In [55], the classical beamforming function is modified as a SVR problem to control the sidelobe and to increase the robustness. The optimization problem are rewritten in terms of real variables in order to apply SVR. Likewise, (2.11) can be expressed in terms of real and imaginary parts as follows:

$$\widetilde{\mathbf{y}} = \overline{\mathbf{Z}}\widetilde{\boldsymbol{\omega}} \tag{3.1}$$

where

$$\widetilde{\boldsymbol{\omega}}^T = \begin{bmatrix} \Re(\boldsymbol{\omega}_{FBLP}^T) & \Im(\boldsymbol{\omega}_{FBLP}^T) \end{bmatrix};$$

$$\overline{\mathbf{Z}} = \begin{bmatrix} \Re(\mathbf{Z}) & -\Im(\mathbf{Z}) \\ \Im(\mathbf{Z}) & \Re(\mathbf{Z}) \end{bmatrix};$$

$$\widetilde{\mathbf{y}}^T = \begin{bmatrix} \Re(\mathbf{y}^T) & \Im(\mathbf{y}^T) \end{bmatrix}.$$

The transformed vector $\widetilde{\boldsymbol{\omega}}$ belongs to $\mathbb{R}^{2P\times 1}$, $\widetilde{\mathbf{y}} \in \mathbb{R}^{2N_T\times 1}$, and $\overline{\mathbf{Z}} \in \mathbb{R}^{2N_T\times 2P}$, $N_T = 2(M-P)L$.

It is worth noting that (3.1) can be viewed as a typical form of SVR in the real domain. We can calculate $\boldsymbol{\omega}_{FBLP}$ according to the derivations in Section 2.2.5.

Unlike the training and testing process in Section 2.2.5, SVR is combined with the FBLP method in this chapter.

In the optimization problem, the empirical error is calculated according to the ϵ-intensive loss function. The regularization term concerning $\widetilde{\boldsymbol{\omega}}$ denotes the model complexity. Therefore, the primal optimization problem is given by:

$$\min_{\widetilde{\boldsymbol{\omega}},\boldsymbol{\xi},\widetilde{\boldsymbol{\xi}}} L_p(\widetilde{\boldsymbol{\omega}},\boldsymbol{\xi},\widetilde{\boldsymbol{\xi}}) = \min_{\widetilde{\boldsymbol{\omega}},\boldsymbol{\xi},\widetilde{\boldsymbol{\xi}}} (\frac{1}{2}\|\widetilde{\boldsymbol{\omega}}\|^2 + C\sum_{i=1}^{2N_T}(\xi_i + \widetilde{\xi}_i)) \tag{3.2}$$

$$\text{s.t.} \begin{cases} \widetilde{y}_i - \overline{\mathbf{z}}_i^T\widetilde{\boldsymbol{\omega}} \leqslant \epsilon + \xi_i, i = 1,\ldots,2N_T \\ -\widetilde{y}_i + \overline{\mathbf{z}}_i^T\widetilde{\boldsymbol{\omega}} \leqslant \epsilon + \widetilde{\xi}_i, i = 1,\ldots,2N_T \\ \xi_i, \widetilde{\xi}_i \geqslant 0, i = 1,\ldots,2N_T \end{cases}$$

where $\overline{\mathbf{z}}_i$ and $\widetilde{y}_i$ are the ith column of $\overline{\mathbf{Z}}^T$ and $\widetilde{\mathbf{y}}^T$, respectively; ξ_i and $\widetilde{\xi}_i$ are the corresponding slack variables to compensate to empirical errors; C is the balance between the regularization and empirical error.

The method of Lagrange multipliers is applied to find the minima of (3.2). Therefore, we deduce the following primal-dual objective function:

$$\begin{aligned} L_{pd} = &\frac{1}{2}\|\widetilde{\boldsymbol{\omega}}\|^2 + C\sum_{i=1}^{2N_T}(\xi_i + \widetilde{\xi}_i) - \sum_{i=1}^{2N_T}(\lambda_i\xi_i + \widetilde{\lambda}_i\widetilde{\xi}_i) \\ &+ \sum_{i=1}^{2N_T}\alpha_i(\widetilde{y}_i - \overline{\mathbf{z}}_i^T\widetilde{\boldsymbol{\omega}} - \epsilon - \xi_i) \\ &+ \sum_{i=1}^{2N_T}\widetilde{\alpha}_i(-\widetilde{y}_i + \overline{\mathbf{z}}_i^T\widetilde{\boldsymbol{\omega}} - \epsilon - \widetilde{\xi}_i) \end{aligned} \tag{3.3}$$

where α_i, $\widetilde{\alpha}_i$, λ_i, and $\widetilde{\lambda}_i$ are Lagrange multipliers.

The partial derivatives of L_{pd} with respect to the primal variables ($\widetilde{\boldsymbol{\omega}}$, ξ_i, and $\widetilde{\xi}_i$) should equal to zero at the saddle point:

$$\begin{cases} \frac{\partial L_{pd}}{\partial \widetilde{\boldsymbol{\omega}}} = \widetilde{\boldsymbol{\omega}} - \sum_{i=1}^{2N_T}(\alpha_i - \widetilde{\alpha}_i)\overline{\mathbf{z}}_i = 0 \\ \frac{\partial L_{pd}}{\partial \xi_i} = C - \alpha_i - \lambda_i = 0,\ i = 1,\ldots,2N_T \\ \frac{\partial L_{pd}}{\partial \widetilde{\xi}_i} = C - \widetilde{\alpha}_i - \widetilde{\lambda}_i = 0,\ i = 1,\ldots,2N_T \end{cases} \tag{3.4}$$

The weight vector $\widetilde{\boldsymbol{\omega}}$ is reformulated by means of Lagrange multipliers: $\widetilde{\boldsymbol{\omega}} = \sum_{i=1}^{2N_T}(\alpha_i - \widetilde{\alpha}_i)\overline{\mathbf{z}}_i$.

Substituting (3.4) into (3.3) yields the dual optimization problem:

$$L_d = \max_{\boldsymbol{\alpha},\widetilde{\boldsymbol{\alpha}}} [-\frac{1}{2}(\boldsymbol{\alpha}-\widetilde{\boldsymbol{\alpha}})^T(\overline{\mathbf{Z}}\,\overline{\mathbf{Z}}^T+\gamma\mathbf{I})(\boldsymbol{\alpha}-\widetilde{\boldsymbol{\alpha}})-\epsilon\mathbf{1}_{2N_T\times 1}^T(\boldsymbol{\alpha}+\widetilde{\boldsymbol{\alpha}})+\widetilde{\mathbf{y}}^T(\boldsymbol{\alpha}-\widetilde{\boldsymbol{\alpha}})] \quad (3.5)$$

$$\text{s.t. } 0 \leqslant \alpha_i, \widetilde{\alpha}_i \leqslant C, \;\; i = 1, \ldots, 2N_T$$

where $\boldsymbol{\alpha} = [\alpha_1, \alpha_2, \ldots, \alpha_{2N_T}]^T$ and $\widetilde{\boldsymbol{\alpha}} = [\widetilde{\alpha}_1, \widetilde{\alpha}_2, \ldots, \widetilde{\alpha}_{2N_T}]^T$; $\mathbf{1}_{2N_T\times 1}$ is an all-one column vector with $2N_T$ elements.

The coefficients vectors $\boldsymbol{\alpha}$ and $\widetilde{\boldsymbol{\alpha}}$ in (3.5) can be calculated using QP solvers. The QP techniques are computationally demanding. Nevertheless, the number of samples in the considered situations being small, the increase of the computational burden is not significant, which will be shown qualitatively in the simulation part.

Finally, the weight vector $\widetilde{\boldsymbol{\omega}}$ is obtained. We can rewrite it back into the complex domain as $\boldsymbol{\omega}(i) = \widetilde{\boldsymbol{\omega}}(i) + j\widetilde{\boldsymbol{\omega}}(i+P)$ for $i = 1, \ldots, P$ and then find the DOAs by searching the peak positions of the PSD spectrum defined in (2.13).

3.3 Simulation

In this section, the performance of the proposed method is evaluated with five simulations. We assume a ULA with 10 isotropic sensors (i.e., $M = 10$). The distance between two adjacent sensors is half the wavelength of incoming signals, $d = \lambda/2$.

The research results in [27] show that the decorrelation ability of LP methods is at the expense of the real effective array aperture. In order to maintain an effective array aperture, we chose P = 9. Therefore, the number of snapshots L in the standard FBLP should be greater than 5 in order to make the covariance matrix invertible.

The SVR parameters used in all the simulations are $\epsilon = 0.1$, $C = 0.1$, and $\gamma = 10^{-6}$, as in [28]. In our extensive simulation experiences, C and γ are insensitive parameters while ϵ should be small values. There may be other analytic parameter selection methods or other pairs of parameter settings, but the proposed FBLP-SVR shows its robustness with these parameters at different scenarios. The sensitivity analysis of parameter settings in FBLP-SVR and the corresponding change in the performance are shown in Appendix B. Even if FBLP-SVR in Appendix B is applied in TDE, its performance in the estimation of DOA shows similar tendency.

3.3.1 Performance with PSD

In the first simulation, we examine the PSD of the standard FBLP and the proposed FBLP-SVR not only with two sources, but also with three sources, in coherent scenarios. In the two-source case, the signals come from $\theta_1 = 10°$, $\theta_2 = 20°$. When there are three sources, the signals come from $\theta_1 = -20°$, $\theta_2 = 0°$, $\theta_3 = 8°$. The signal to noise ratio (SNR) is fixed at 10 dB. In both cases, two different numbers of snapshots are considered: L = 100 and L = 5. The spatial spectrum search is performed over $[-90°, 90°]$ with step size $0.01°$. The angles corresponding to the two highest peak positions in the spectrum allow the estimation of the DOAs of incoming signals. Figures 3.1 and 3.2 show the PSD of the methods with two and three coherent sources, respectively. The vertical dashed lines indicate the true values of DOAs.

As shown in the two-source case in Figure 3.1, FBLP-SVR and FBLP perform better with 100 snapshots than with 5 snapshots in terms of the positions of the peaks and stability of curves across the spectrum. When there are 100 snapshots, these two methods are able to detect the true DOAs. The PSD curves of FBLP and FBLP-SVR are similar to each other. However, in the scenario where there are only five snapshots, the FBLP-SVR method can accurately detect the signals while the standard FBLP fails. Similar results can be observed in a three-source case in Figure 3.2. The curves of FBLP-SVR have no false peaks, even when the number of snapshots is small.

3.3.2 Performance versus angle separation

In order to know the resolution performance of the proposed FBLP-SVR, we carry out several statistical analyses with different angle separations of incoming signals. The results of standard FBLP, FLP, SVR-based FLP method (FLP-SVR) are collected for comparison. Two coherent signals are used in this simulation: one is fixed at direction $\theta_1 = 0°$; the other comes from $\theta_2 = \theta_1 + \Delta\theta$ with the same power, $\Delta\theta \in [1°, 10°]$. SNR is set as 15 dB.

The probability of success estimation (PSE) is used to carry out the first statistical analysis, which is defined as the ratio between the number of successful estimations and the total number of estimations. An estimation is considered as successful if the estimation of all K sources satisfies $|\hat{\theta}_k - \theta_k| \leq \Delta\theta/2,\ k = 1, 2$.

Four methods, FBLP-SVR, FLP-SVR, the standard FBLP and FLP, are tested with 5 and 100 snapshots over 500 independent trials. Figure 3.3 depicts the PSE of DOA estimation versus angle separation for 5 and 100 snapshots. It is obvious that these methods can

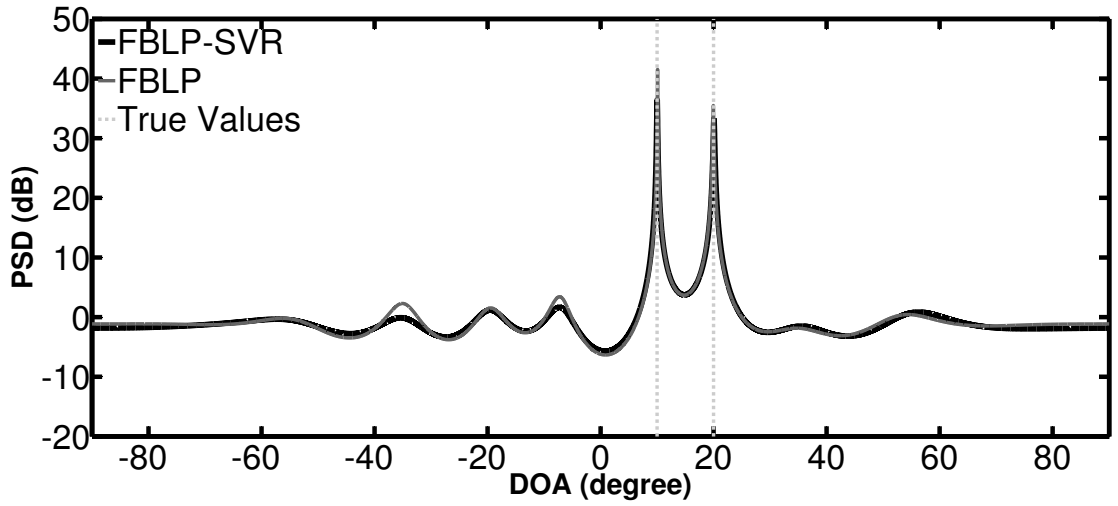

(a)

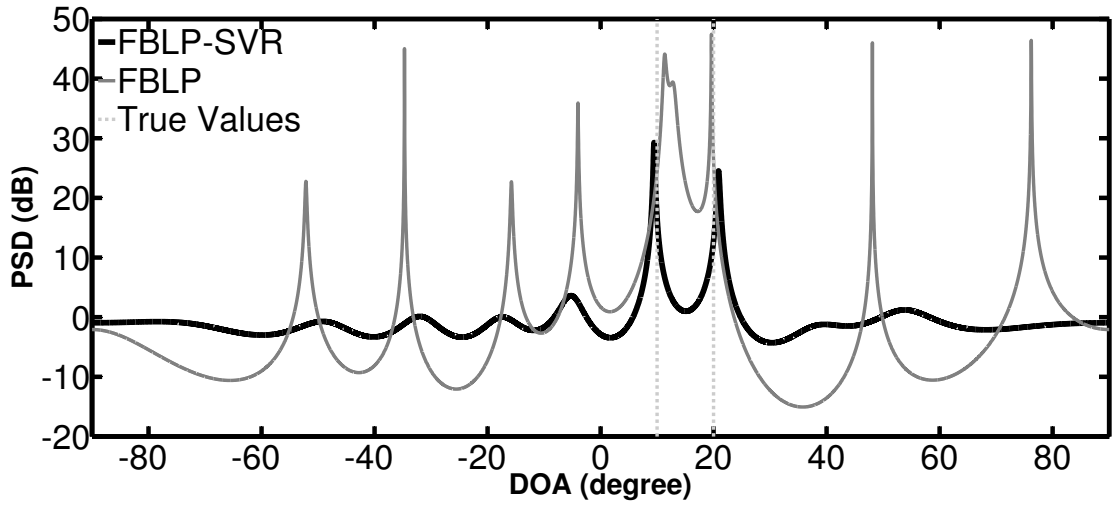

(b)

Figure 3.1 – PSD of FBLP-SVR and FBLP with 10 antennas and 2 coherent signals coming from $\theta_1 = 10°$, $\theta_2 = 20°$. (a) Number of snapshots = 100; (b) Number of snapshots = 5.

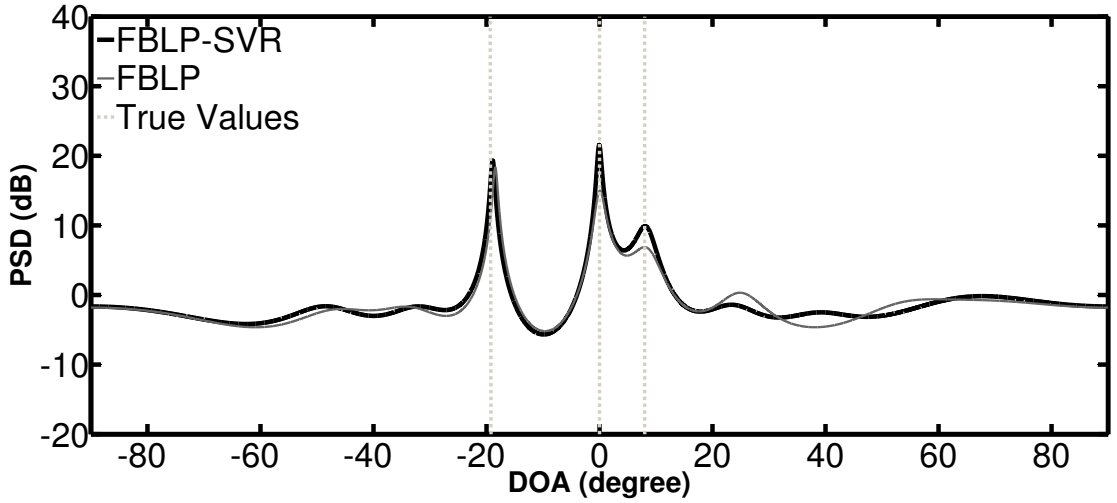

(a)

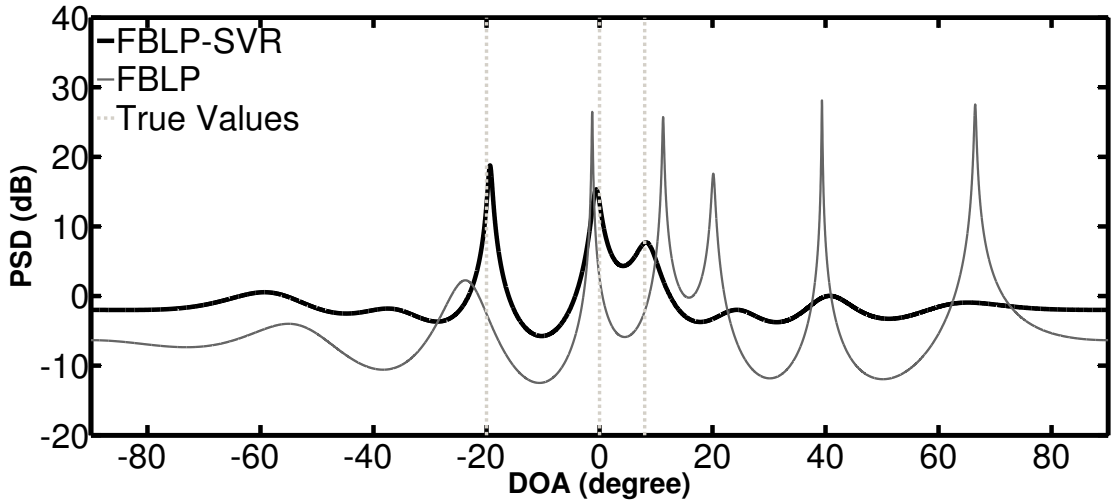

(b)

Figure 3.2 – PSD of FBLP-SVR and FBLP with 10 antennas and 3 coherent signals coming from $\theta_1 = -20°$, $\theta_2 = 0°$, $\theta_3 = 8°$. (a) Number of snapshots = 100; (b) Number of snapshots = 5.

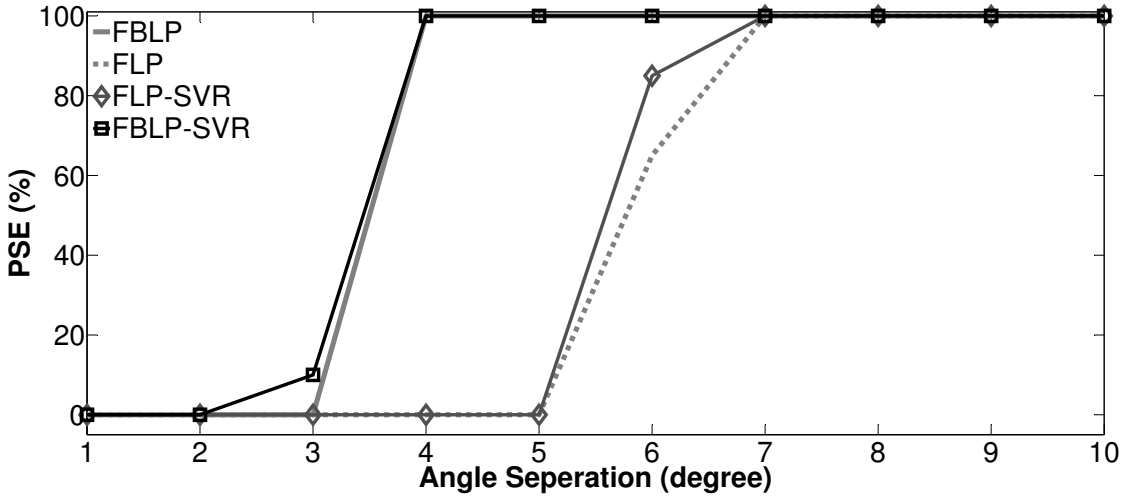

(a)

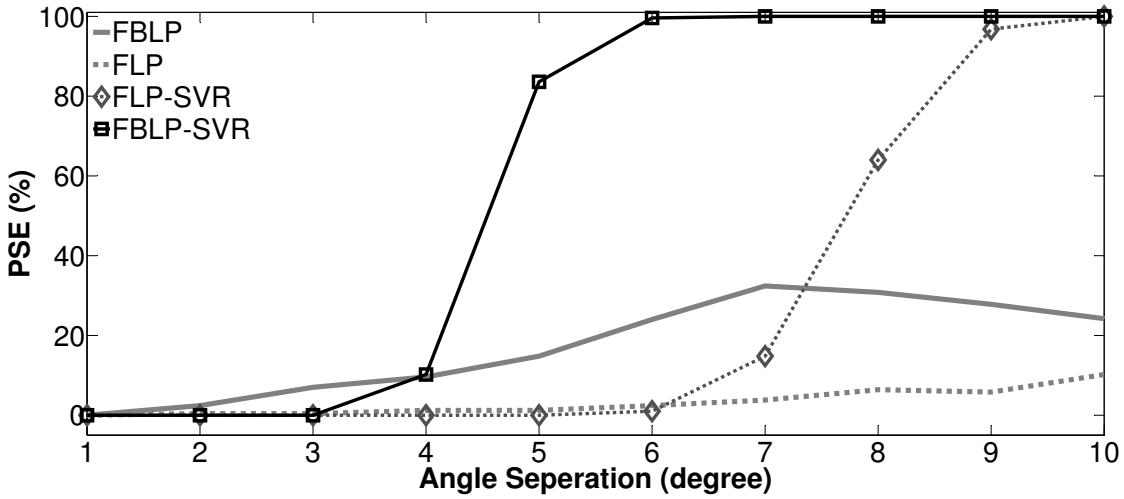

(b)

Figure 3.3 – PSE of FBLP, FLP, FLP-SVR, and FBLP-SVR as a function of angle separation. (a) Number of snapshots = 100; (b) Number of snapshots = 5.

not detect the signals with small angle separations. As the angle separation between two signals increases, the PSE of these methods increases to 100%. The difference between Figure 3.3–(a) and (b) shows that the performance with 5 snapshots is inferior to that with 100 snapshots. When there are 100 snapshots, the PSE of FBLP and FBLP-SVR is similar. The same results can be found by using FLP and FLP-SVR. In comparison with FLP-based methods, FBLP based methods reach 100% successful estimation rate at smaller angle separation ($\Delta\theta = 4°$). When there are 5 snapshots, the PSE of standard LP methods (FBLP, FLP) stays at a low rate at different angle separations. SVR improves the accuracy of LP methods, specifically when the number of snapshots is low.

Besides, the root mean square error (RMSE) is also calculated to show the estimation results. The definition of RMSE is given by [67]:

$$RMSE = \sqrt{\frac{1}{KJ}\sum_{j=1}^{J}\sum_{k=1}^{K}(\hat{\theta}_{kj} - \theta_k)^2} \tag{3.6}$$

where $\hat{\theta}_{kj}$ is the estimate of θ_k at the jth independent trial. J is the total number of trials.

Figure 3.4 depicts the RMSE of DOA estimation versus angle separation for the four methods with both 5 and 100 snapshots. The Cramér-Rao Lower Bound (CRLB, refer to [70], the formulations of CRLB can be found in Appendix A) is also added. The statistic results in Figure 3.4 are consistent with the PSEs in Figure 3.3. When there are 100 snapshots, FBLP and FBLP-SVR work better than single direction FLP and FLP-SVR. When there are 5 snapshots, SVR based LP methods have lower RMSEs than standard LP methods. FBLP-SVR has the best accuracy and outperforms FBLP, FLP, and FLP-SVR.

3.3.3 Performance versus number of snapshots

In the third simulation, we test the performance of the proposed method as a function of the number of snapshots. The simulation conditions are similar to the second simulation, except that two coherent sources are from $\theta_1 = 0°$ and $\theta_2 = 6°$. The comparison is conducted between the standard FBLP and the proposed FBLP-SVR. The number of snapshots L varies from $[5, 10, 15, 20, \ldots, 50]$. Figure 3.5 shows the RMSE of DOA estimation versus the number of snapshots via 500 independent trials. The RMSE of FBLP-SVR and FBLP decreases with the increase of the number of snapshots. When the number of snapshots is low, the proposed FBLP-SVR gives much better estimation results than the standard FBLP. As L gets larger, FBLP and FBLP-SVR achieve similar results.

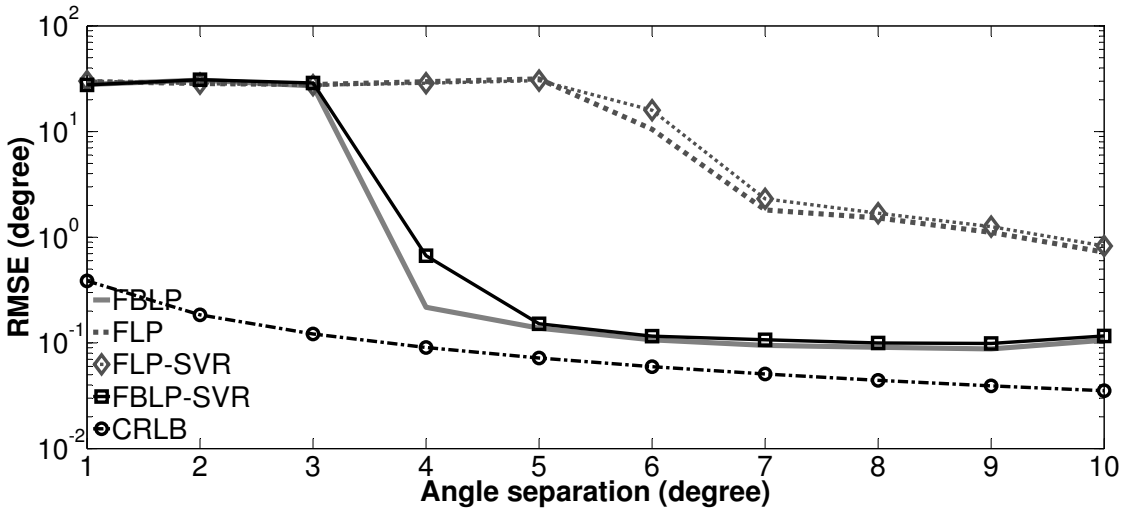

(a)

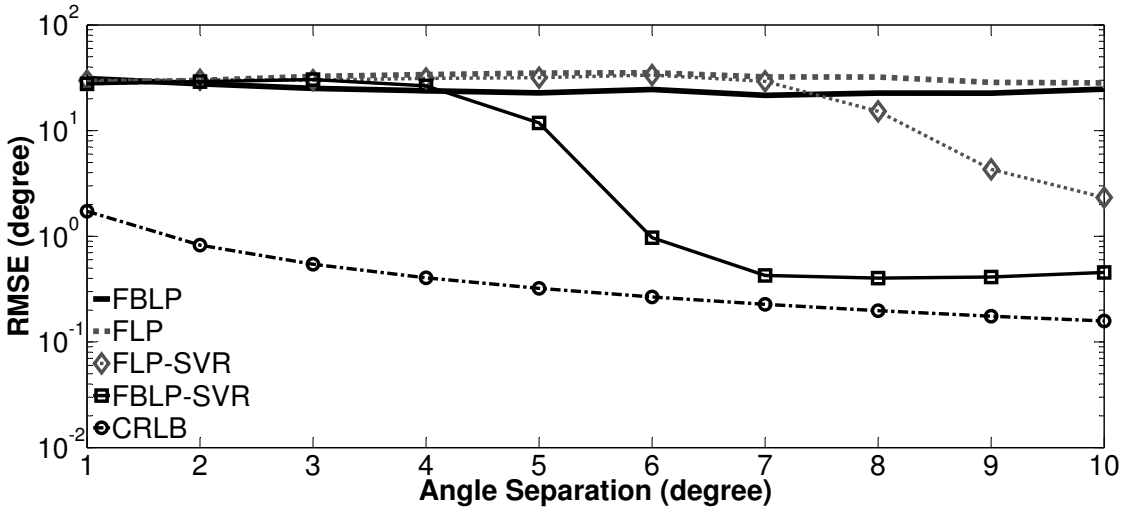

(b)

Figure 3.4 – RMSE of FBLP, FLP, FLP-SVR, and FBLP-SVR as a function of angle separation. (a) Number of snapshots = 100; (b) Number of snapshots = 5.

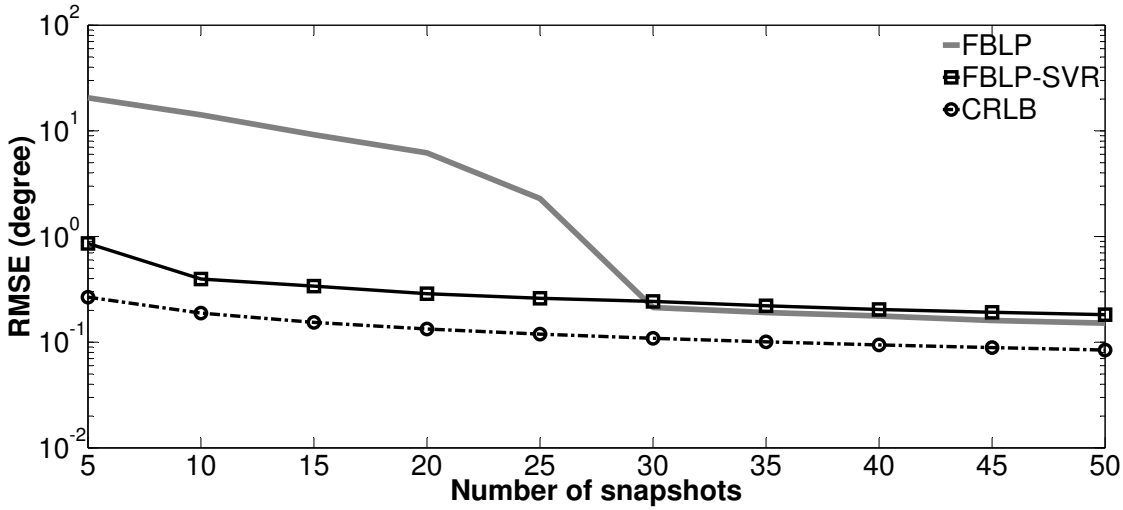

Figure 3.5 – RMSE of DOA estimation versus number of snapshots.

In order to get an idea about the computational burden, the execution time is evaluated with $L = 5$ during 500 simulations. The average time for a single simulation using the proposed FBLP-SVR is 0.2728 s, while the corresponding time for the standard FBLP is 0.2595 s with a computer equipped with a processor unit (CPU) of 2.7 GHz and 16 GB of RAM. Therefore, the combination of SVR with FBLP can greatly improve the estimation performance with only a small increment of operation time, especially when the number of snapshots is limited.

3.3.4 Performance versus SNR

In the fourth simulation, we evaluate the performance of the proposed FBLP-SVR with respect to SNR in coherent scenarios. Two signals come from $\theta_1 = 0°$ and $\theta_2 = 6°$, respectively. Only 5 snapshots are used in this simulation. SNR varies from 0 dB to 30 dB. The RMSE is calculated with 500 independent trials for each SNR. The RMSE against SNR with 5 snapshots is plotted in Figure 3.6. It is obvious that FBLP-SVR has a more significant decrease of RMSE when SNR increases, compared with the standard FBLP. Furthermore, FBLP-SVR is closer to the CRLB than FBLP.

3.3.5 Performance versus steering vector uncertainty

In this section, we analyze the influence of steering vector uncertainty on the performance of the proposed FBLP-SVR method. The simulation settings are the same with Sec-

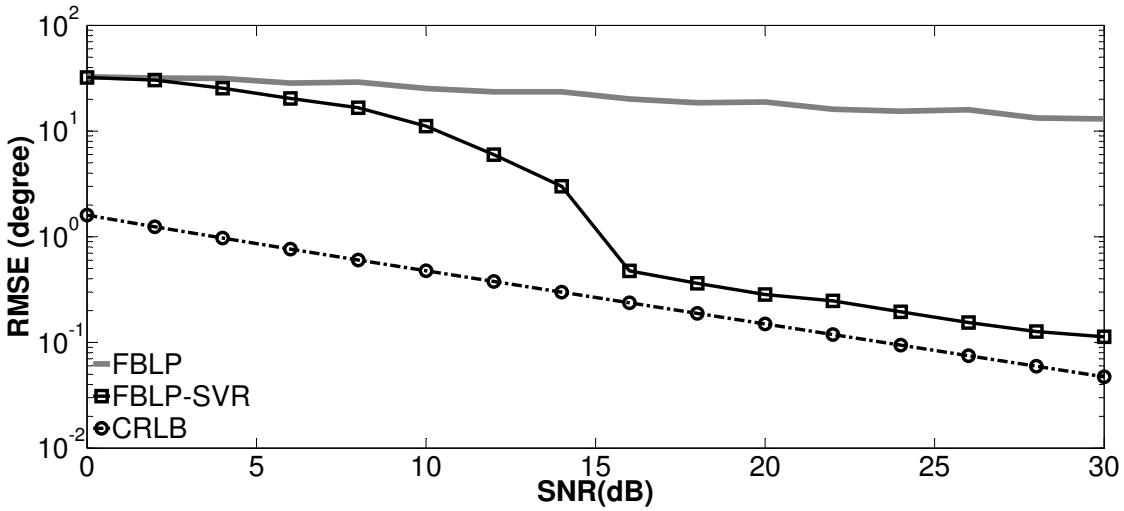

Figure 3.6 – RMSE of DOA estimation versus SNR via 5 snapshots.

tion 3.3.4 except SNR = 20 dB. The steering vector uncertainty is represented by $\hat{\mathbf{a}} = \mathbf{a} + \Delta$, where $\mathbf{a}$ is the steering vector of the incoming signal and Δ is the steering vector uncertainty characterized as an AGWN noise vector with zero mean and covariance matrix $\sigma_1^2\mathbf{I}$. The performance of FBLP-SVR and FBLP versus $-20log_{10}(\sigma_1)$ is shown in Figure 3.7 over 500 independent trials.

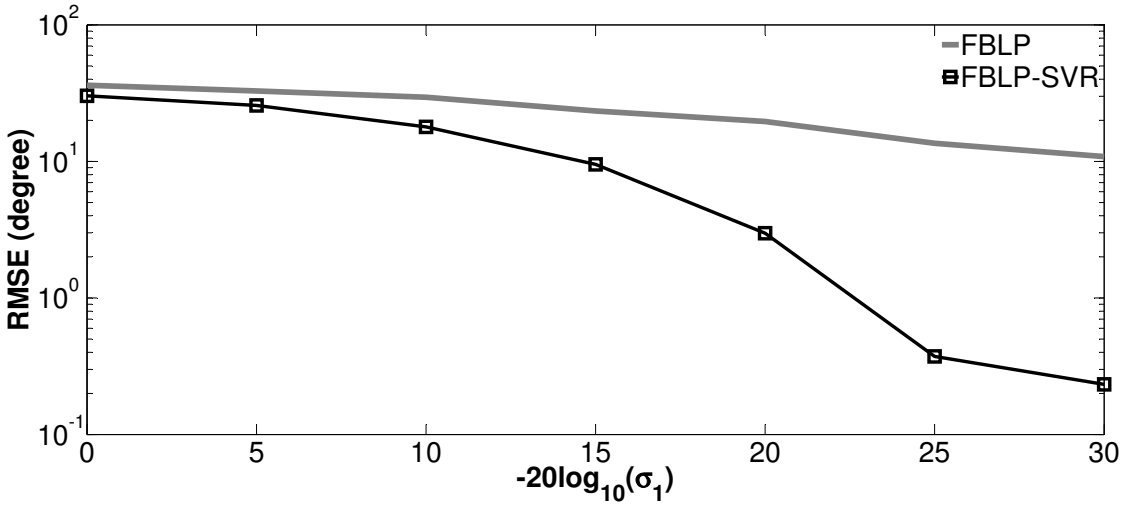

Figure 3.7 – RMSE of FBLP-SVR and FBLP versus $-20log_{10}(\sigma_1)$.

In Figure 3.7, the RMSE of FBLP-SVR decreases much faster than that of the standard FBLP. Therefore, in this case, FBLP-SVR is more robust than the standard FBLP in terms of the steering vector uncertainty.

3.4 Conclusion

This chapter proposes the combination of the advantages of FBLP and SVR in the estimation of DOAs of coherent incoming signals with limited snapshots. The proposed FBLP-SVR allows to directly deal with coherent signals, and remains applicable with a limited number of snapshots. The performance of the proposed method is validated with numerical simulations in coherent scenarios, in terms of different angle separations, numbers of snapshots, SNRs, and different levels of steering vector uncertainty. Simulation results prove the stability and robustness of FBLP-SVR with coherent signals and low numbers of snapshots, in comparison with FLP, FLP-SVR, and FBLP. In the next chapter, we will present an extension of FBLP-SVR in TDE.

4

Proposed time-delay estimation method using GPR

4.1 Introduction

GPR is a common tool for subsurface sensing in the field of civil engineering, defense, agriculture and environment [7, 8, 9]. It allows nondestructive probing and therefore gains much interest both in media parameters estimation and in buried targets localization [71, 72, 73]. In civil engineering, GPR is used to survey horizontally stratified media, for example, roadways. The information of the vertical structure of the stratified media can be extracted from radar profiles by means of echo detection and amplitude estimation. Echo detection provides the time-delay associated with each interface, whereas amplitude estimation is used to retrieve the wave speed within each layer.

In Chapter 3, LP methods have shown its high resolution and the ability to deal with coherent signals in far-field source localization problems. In GPR applications, there are researches making use of LP to detect buried objects [74, 75, 76, 77]. LP is used to predict the next GPR signal from the previous observations. An object appears when the measured signal is different from the prediction. Besides, there are GPR applications by using AR model in the estimation of parameters of subsurface materials, for example, the estimation

of time-delay [9] and soil permittivity [78]. Nevertheless, the performance of LP is limited when the observation records are short [74].

Likewise, the sparse SVR can be applied with LP to deal with short observation records. In the literature, SVR has been embeded with several linear signal processing algorithms, for example, the AR-SVR [56, 57] and ARMA-SVR [58] for frequency estimation and system identification applications. Nevertheless, FBLP performs better than the one-side FLP and BLP. Moreover, FBLP-SVR provides satisfactory performance in the estimation of DOA in Chapter 3. Therefore, we would like to analyze the performance of FBLP-SVR in TDE. Contrary to Chapter 3, the complex variables here are directly formulated in the complex domain with Wirtinger's calculus [59, 79].

4.2 Signal Model

The TDE signal model presented in Section 2.2 is adopted here. In order to use LP methods, the received GPR signals are whitened by the radar pulse. Therefore, (2.4) becomes:

$$r_m = \frac{g_m}{e_m} = \sum_{k=1}^{K} s_k e^{-j2\pi f_m \tau_k} + \frac{n_m}{e_m}. \tag{4.1}$$

With L independent snapshots, the data sample at frequency f_m can be written as

$$\mathbf{r}_m = [r_m(1), r_m(2), \ldots, r_m(L)]^T. \tag{4.2}$$

4.3 Proposed method

Similarly, we can write the FBLP equation with the whitened GPR signals as follows:

$$\begin{bmatrix} \mathbf{r}_P & \mathbf{r}_{P-1} & \cdots & \mathbf{r}_1 \\ \vdots & \vdots & & \vdots \\ \mathbf{r}_{M-1} & \mathbf{r}_{M-2} & \cdots & \mathbf{r}_{M-P} \\ & \cdots\cdots\cdots\cdots & & \\ \mathbf{r}_2^* & \mathbf{r}_3^* & \cdots & \mathbf{r}_{P+1}^* \\ \vdots & \vdots & \vdots & \\ \mathbf{r}_{M-P+1}^* & \mathbf{r}_{M-P+2}^* & \cdots & \mathbf{r}_M^* \end{bmatrix} \begin{bmatrix} \omega_1 \\ \vdots \\ \omega_P \end{bmatrix} = \begin{bmatrix} \mathbf{r}_{P+1} \\ \vdots \\ \mathbf{r}_M \\ \cdots \\ \mathbf{r}_1^* \\ \vdots \\ \mathbf{r}_{M-P}^* \end{bmatrix}. \tag{4.3}$$

where P is the order of the prediction filter.

Rewrite (4.3) in the same compact form as in (2.11):

$$\mathbf{Z}\boldsymbol{\omega}_{FBLP} = \mathbf{y}$$

where $\mathbf{y} \in \mathbb{C}^{N_T \times 1}$, $\mathbf{Z} \in \mathbb{C}^{N_T \times P}$, and $\boldsymbol{\omega}_{FBLP} \in \mathbb{C}^{P \times 1}$, $N_T = 2(M-P)L$.

The weight vector $\boldsymbol{\omega}_{FBLP}$ can be calculated by SVR. In contrast to Chapter 3, the SVR model in this chapter is formulated directly in the complex domain to deal with complex data in a more natural way [28, 59]. The research in [59] deals with complex-valued nonlinear regression problems by exploiting Wirtinger's calculus, which is very inspiring in finding the solution of FBLP in this chapter.

The ϵ-intensive loss function is used here. Since the empirical errors are complex-valued, the residuals in SVR should be minimized both in their real and imaginary parts. Therefore, the primal optimization task can be expressed as [28, 59, 65]:

$$\min_{\boldsymbol{\omega}_{FBLP},\boldsymbol{\xi}^r,\hat{\boldsymbol{\xi}}^r,\boldsymbol{\xi}^i,\hat{\boldsymbol{\xi}}^i} (\frac{1}{2}\|\boldsymbol{\omega}_{FBLP}\|^2 + C\sum_{n=1}^{N_T}(\xi_n^r + \hat{\xi}_n^r + \xi_n^i + \hat{\xi}_n^i)) \tag{4.4}$$

$$\text{s. t.} \begin{cases} \Re(y_n - \mathbf{z}_n^H\boldsymbol{\omega}_{FBLP}) \leqslant \epsilon + \xi_n^r, n = 1,\ldots,N_T \\ \Re(-y_n + \mathbf{z}_n^H\boldsymbol{\omega}_{FBLP}) \leqslant \epsilon + \hat{\xi}_n^r, n = 1,\ldots,N_T \\ \Im(y_n - \mathbf{z}_n^H\boldsymbol{\omega}_{FBLP}) \leqslant \epsilon + \xi_n^i, n = 1,\ldots,N_T \\ \Im(-y_n + \mathbf{z}_n^H\boldsymbol{\omega}_{FBLP}) \leqslant \epsilon + \hat{\xi}_n^i, n = 1,\ldots,N_T \\ \xi_n^r, \hat{\xi}_n^r, \xi_n^i, \hat{\xi}_n^i \geqslant 0, n = 1,\ldots,N_T \end{cases}$$

where $\mathbf{z}_n$ is the nth column of $\mathbf{Z}^H$ and $y_n = \mathbf{y}(n)$, $n = 1,\ldots,N_T$. ξ_n^r and $\hat{\xi}_n^r$ stand for the positive and negative errors in the real part of y_n while ξ_n^i and $\hat{\xi}_n^i$ are for the corresponding imaginary part, respectively. The value C controls the trade-off between the structural and empirical errors.

The method of Lagrangian multipliers is employed to find the solutions of (4.4) by introducing a dual set variables. Therefore, we have the primal-dual objective function:

$$
\begin{aligned}
L_{pd}(\boldsymbol{\omega}_{FBLP}) = \tfrac{1}{2}\|\boldsymbol{\omega}_{FBLP}\|^2 + C\sum_{n=1}^{N_T}(\xi_n^r + \hat{\xi}_n^r + \xi_n^i + \hat{\xi}_n^i) \\
+ \sum_{n=1}^{N_T} a_n(\Re(y_n - \mathbf{z}_n^H\boldsymbol{\omega}_{FBLP}) - \epsilon - \xi_n^r) \\
+ \sum_{n=1}^{N_T} \hat{a}_n(\Re(-y_n + \mathbf{z}_n^H\boldsymbol{\omega}_{FBLP}) - \epsilon - \hat{\xi}_n^r) \\
+ \sum_{n=1}^{N_T} b_n(\Im(y_n - \mathbf{z}_n^H\boldsymbol{\omega}_{FBLP}) - \epsilon - \xi_n^i) \\
+ \sum_{n=1}^{N_T} \hat{b}_n(\Im(-y_n + \mathbf{z}_n^H\boldsymbol{\omega}_{FBLP}) - \epsilon - \hat{\xi}_n^i) \\
- \sum_{n=1}^{N_T} \eta_n\xi_n^r - \sum_{n=1}^{N_T} \hat{\eta}_n\hat{\xi}_n^r - \sum_{n=1}^{N_T} \lambda_n\xi_n^i - \sum_{n=1}^{N_T} \hat{\lambda}_n\hat{\xi}_n^i
\end{aligned}
\tag{4.5}
$$

where a_n, $\hat{a}_n$, b_n, $\hat{b}_n$, η_n, $\hat{\eta}_n$, λ_n, and $\hat{\lambda}_n$ are Lagrangian multipliers.

(4.4) and (4.5) are real-valued functions defined on complex variables. In order to apply KKT theorem, Wirtinger's calculus [79, 59] is carried out for the complex variable $\boldsymbol{\omega}_{FBLP}$. The theory of Wirtinger's calculus and the derivation of L_{pd} with respect to $\boldsymbol{\omega}_{FBLP}$ are presented in Appendix C. Besides, the gradients of real variables are computed in the traditional way. Then, we deduce:

$$
\begin{cases}
\frac{\partial L_{pd}}{\partial \boldsymbol{\omega}_{FBLP}^*} = \frac{1}{2}\boldsymbol{\omega}_{FBLP} - \frac{1}{2}\sum_{n=1}^{N_T}((a_n - \hat{a}_n) + j(b_n - \hat{b}_n))\mathbf{z}_n = 0 \\
\frac{\partial L_{pd}}{\partial \xi_n^r} = C - a_n - \eta_n = 0, n = 1, \ldots, N_T \\
\frac{\partial L_{pd}}{\partial \hat{\xi}_n^r} = C - \hat{a}_n - \hat{\eta}_n = 0, n = 1, \ldots, N_T \\
\frac{\partial L_{pd}}{\partial \xi_n^i} = C - b_n - \lambda_n = 0, n = 1, \ldots, N_T \\
\frac{\partial L_{pd}}{\partial \hat{\xi}_n^i} = C - \hat{b}_n - \hat{\lambda}_n = 0, n = 1, \ldots, N_T.
\end{cases}
\tag{4.6}
$$

Substituting (4.6) into (4.5), we have the following maximization task:

$$
\begin{aligned}
\max_{\boldsymbol{a},\hat{\boldsymbol{a}},\boldsymbol{b},\hat{\boldsymbol{b}}} \; & -\frac{1}{2}\begin{bmatrix}\boldsymbol{a}-\hat{\boldsymbol{a}} \\ \boldsymbol{b}-\hat{\boldsymbol{b}}\end{bmatrix}^T \begin{bmatrix}\Re(\mathbf{Z}\mathbf{Z}^H) & -\Im(\mathbf{Z}\mathbf{Z}^H) \\ \Im(\mathbf{Z}\mathbf{Z}^H) & \Re(\mathbf{Z}\mathbf{Z}^H)\end{bmatrix}\begin{bmatrix}\boldsymbol{a}-\hat{\boldsymbol{a}} \\ \boldsymbol{b}-\hat{\boldsymbol{b}}\end{bmatrix} \\
& - \epsilon\mathbf{1}_{N_T\times 1}^T(\boldsymbol{a}+\hat{\boldsymbol{a}}+\boldsymbol{b}+\hat{\boldsymbol{b}}) + \Re(\mathbf{y}^T)(\boldsymbol{a}-\hat{\boldsymbol{a}}) + \Im(\mathbf{y}^T)(\boldsymbol{b}-\hat{\boldsymbol{b}}) \\
\text{s. t. } & 0 \leqslant a_n, \hat{\alpha}_n, b_n, \hat{b}_n \leqslant C, \quad n = 1, \ldots, N_T
\end{aligned}
\tag{4.7}
$$

where $\mathbf{1}_{N_T\times 1}$ is a all-one column vector with N_T elements, $\boldsymbol{a} = [a_1, \ldots, a_{N_T}]^T$, $\hat{\boldsymbol{a}} = [\hat{a}_1, \ldots, \hat{a}_{N_T}]^T$, $\boldsymbol{b} = [b_1, \ldots, b_{N_T}]^T$, and $\hat{\boldsymbol{b}} = [\hat{b}_1, \ldots, \hat{b}_{N_T}]^T$.

The Lagrange coefficient vectors $\boldsymbol{a}, \hat{\boldsymbol{a}}, \boldsymbol{b}, \hat{\boldsymbol{b}}$ can be computed using QP solvers. Then, the weight $\boldsymbol{\omega}_{FBLP}$ can be obtained according to (4.6), $\boldsymbol{\omega}_{FBLP} = \sum_{n=1}^{N_T}((a_n - \hat{a}_n) + j(b_n - \hat{b}_n))\mathbf{z}_n$.

4.4 Simulation results

4.4.1 Simulation Settings

Three simulations are carried out to evaluate the performance of the proposed FBLP-SVR method in TDE. The frequency range of the step frequency radar is $[1.0, 4.0]$ GHz, with $M = 21$ frequency samples. The underground structure is assumed to have three layers, Layer 1, Layer 2, and Layer 3, as shown in Figure 4.1. The relative permittivities and thicknesses of the layers are listed in Table 4.1. In the simulation, four echoes (S_0, S_1, S_{M1}, and S_2) are considered. S_0, S_1, and S_2 are the primary echoes, with the corresponding time-delays [τ_0, τ_1, τ_2] = [6.67, 6.95, 7.89] ns. S_{M1} is the multiple echo within the first layer with time-delay $\tau_{M1} = 7.24$ ns. The time resolution is determined by $B\Delta\tau$, where B is the GPR frequency bandwidth and $\Delta\tau$ the time shift between two echoes [9]. If the product $B\Delta\tau$ is greater than 1, the echoes are distinguishable by the conventional FFT based methods. In this simulation, the first three echoes (the first, second primary echo and the multiple echo) are overlapped. The third primary echo is not overlapped with the others. These four echoes are coherent. SNR is defined as the ratio between the power of the last primary echo and the noise variance.

Table 4.1 – Values of relative permittivity and thickness in the horizontal stratified medium.

$\{\epsilon_{r0}, \epsilon_{r1}, \epsilon_{r2}, \epsilon_{r3}\}$	{1, 3, 8, 9}
$\{H_1, H_2\}$ mm	{25, 50}

The work in [27] implies that the smaller the order of the prediction filter P is, the worse the estimation performance of LP will be. Therefore, the order P in this section is set to 19. In this situation, there should be at least 5 snapshots when using the standard FBLP, in order to keep the covariance matrix reversible. In contrast, SVR based method does not require such constraint.

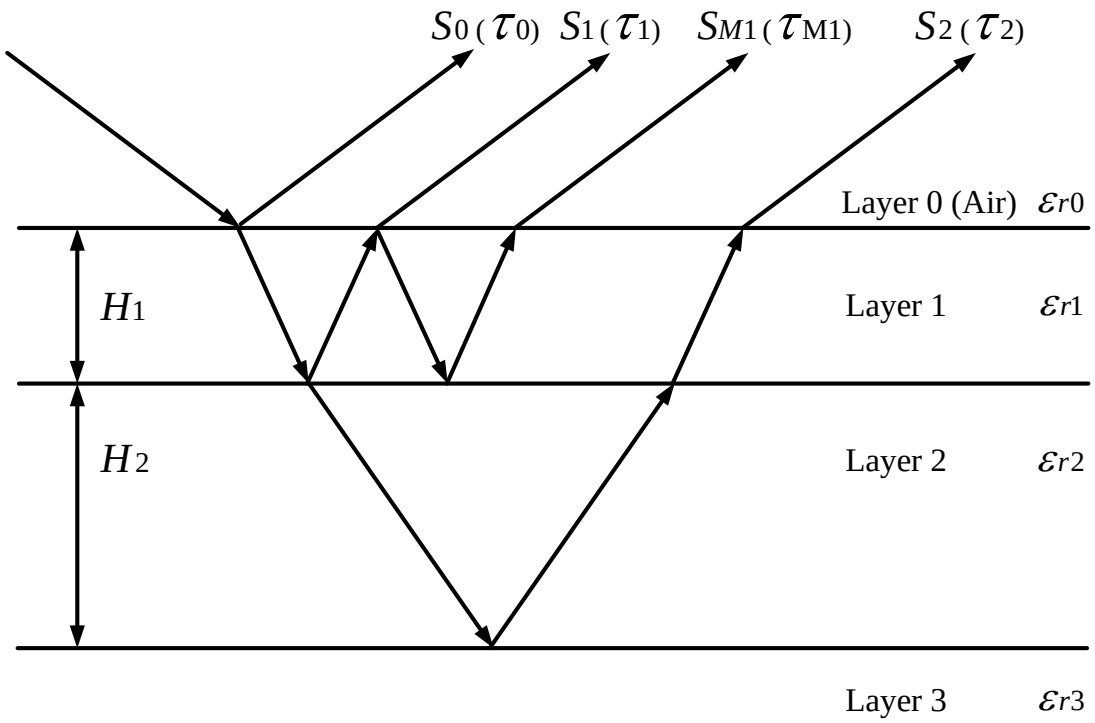

Figure 4.1 – Stratified layers from a simulated setup. H_i and ϵ_{ri} are the thickness and relative permittivity of Layer i ($i \in [0, 1, 2, 3]$), respectively. S_i and τ_i are the reflected echo and time-delay for interface i, respectively. S_{M1} and τ_{M1} are for the multiple echo within the first layer.

In all simulations, the SVR-related parameters are set as $\epsilon = 0$, $C = 1$, and $\gamma = 10^{-6}$. The sensitivity analysis of SVR parameters in TDE is shown in Appendix B.

4.4.2 Performance with PSD

In the first simulation, the normalized PSD of the proposed FBLP-SVR is compared with the standard FBLP and MUSIC. The four highest peak locations in the spectrum allow estimating the four time-delays. The simulation is conducted with 5 and 100 snapshots to show the influence of the number of snapshots on the estimation performance. SNR = 20 dB. The results are depicted in Figure 4.2. The vertical dashed lines are located at the true values of time-delays.

In the scenario with 5 snapshots, the proposed FBLP-SVR can detect the three primary echoes, but the amplitude of PSD of the multiple echo is very weak. The PSD of the standard FBLP has false peaks and it can not correctly detect the multiple echo. When there are 100 snapshots, FBLP and FBLP-SVR perform similarly. Both of them are capable of detecting the three primary echoes and the multiple echo. The performance of FBLP and FBLP-SVR is enhanced with more snapshots. Unfortunately, MUSIC fails to detect the echoes not only with 5 snapshots but also with 100 snapshots, due to the fact that the echoes are totally correlated.

In Figure 4.2, the multiple echo has little impact on the three primary echoes, even when the first two primary echoes are overlapped with the multiple echo. Therefore, the estimation of the multiple echo is excluded in the following.

4.4.3 Performance versus the number of snapshots

In the second simulation, we evaluate the accuracy of the proposed FBLP-SVR as a function of the number of snapshots L, $L \in [1,\ldots,50]$. Since the standard FBLP requires $L \geqslant 5$, its results are shown only from 5 snapshots. FLP-SVR is also considered in this simulation to compare with FBLP-SVR. Other settings are the same as the first simulation. For each number of snapshots, the methods are evaluated with 500 Monte Carlo trials. The performance is assessed with the relative root mean square error (RRMSE), which is defined as [72]

$$RRMSE = \frac{\sqrt{\frac{1}{J}\sum_{j=1}^{J}(\hat{z}_j - z)^2}}{z} \tag{4.8}$$

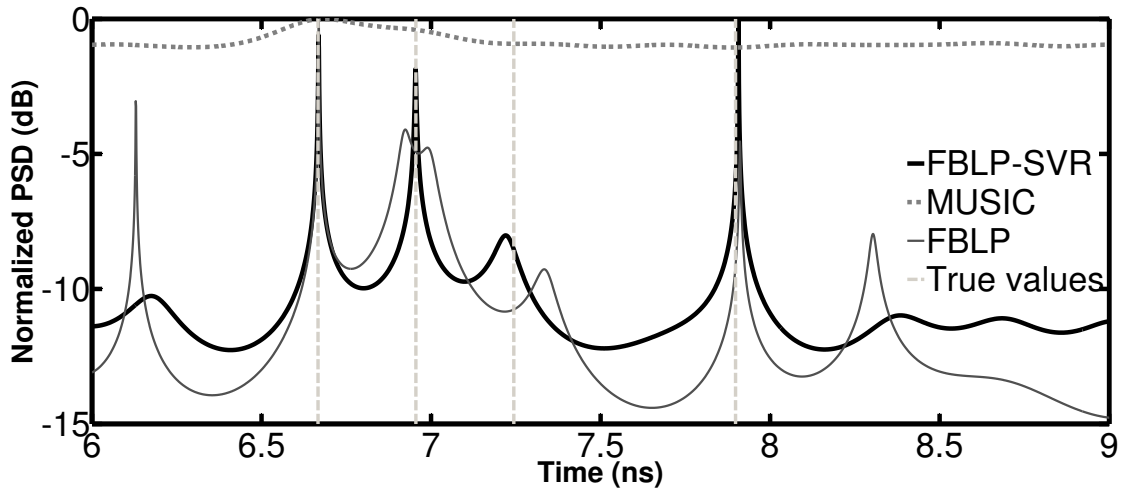

(a)

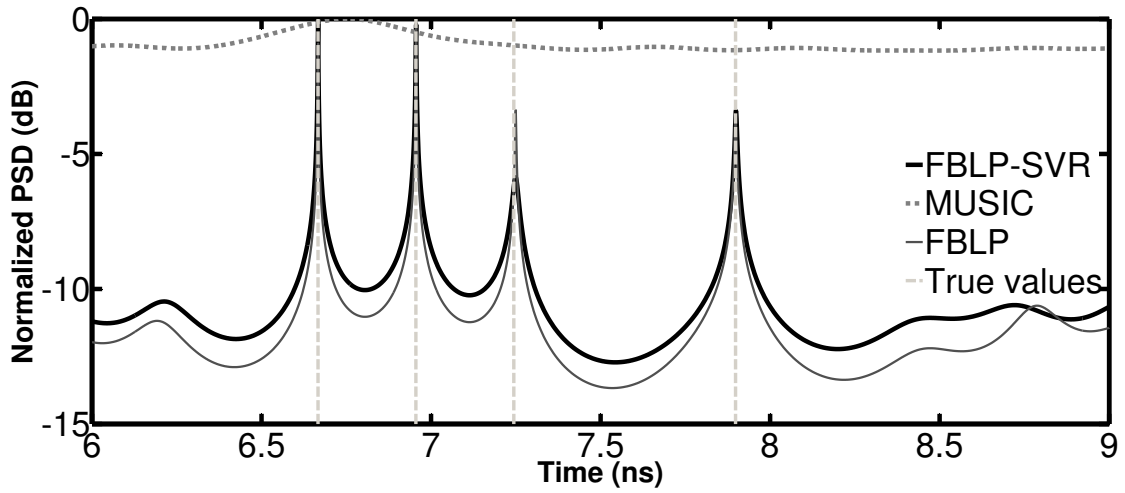

(b)

Figure 4.2 – PSD of FBLP-SVR, FBLP, and MUSIC in the estimation of time-delays. (a) Number of snapshots = 5; (b) Number of snapshots = 100.

where $\hat{z}_j$ denotes the estimated time-delay for the jth run; z is the true value of the time-delay.

The RRMSEs of the three methods versus the number of snapshots are illustrated in Figures 4.3-4.5. With the increasing of the number of snapshots, the RRMSEs of FBLP, FBLP-SVR and FLP-SVR decrease. FBLP-SVR has lower RRMSEs than FLP-SVR at different numbers of snapshots. When the number of snapshots is large (more than 15 in this case), FBLP and FBLP-SVR achieve similar results. But when the number of snapshots is limited, the proposed FBLP-SVR has the best accuracy and outperforms the one-directional FLP-SVR and the traditional FBLP.

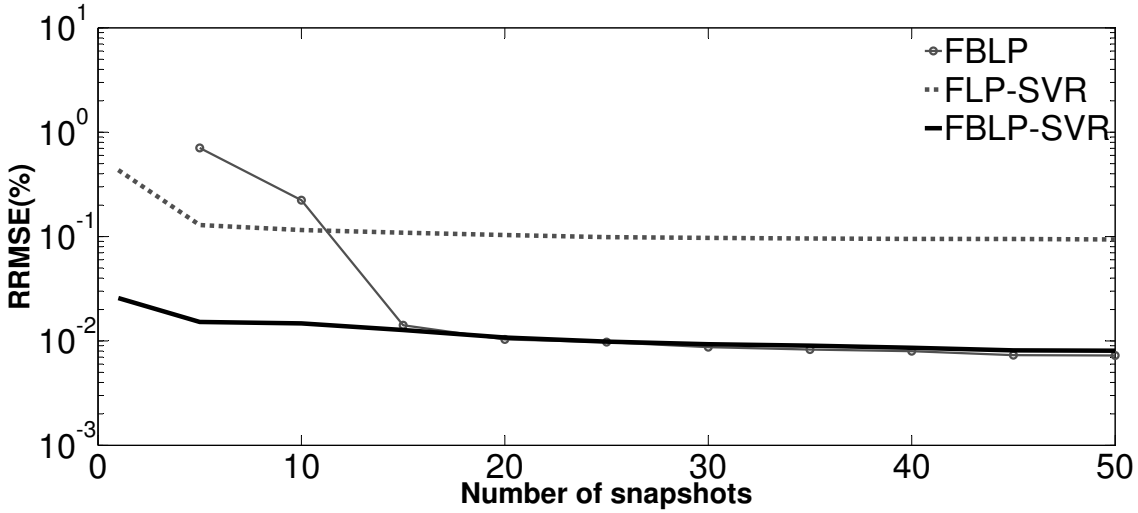

Figure 4.3 – RRMSEs of TDE versus number of snapshots, first primary echo.

The execution time, by a computer equipped with a processor unit (CPU) of 2.7 GHz and 16 GB of RAM, is used to get a rough idea about the computational burden of the proposed method. In the comparison, three methods (the traditional FBLP, FLP-SVR, and FBLP-SVR) are evaluated with $L = 5$ during 500 Monte Carlo trials. The average execution time of one trial using the traditional FBLP, FLP-SVR, and FBLP-SVR are 0.0674 s, 0.0816 s, and 0.0899 s, respectively. In view of the average execution time, these three methods are not time consuming. The combination of FBLP (or FLP) with SVR slightly increases the computational complexity. However, the proposed FBLP-SVR greatly improves the estimation performance.

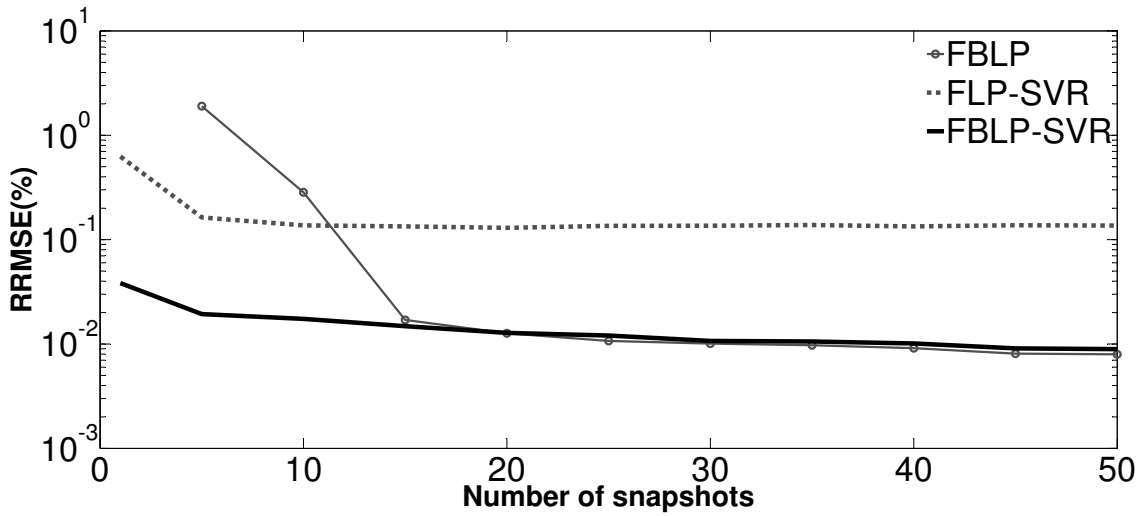

Figure 4.4 – RRMSEs of TDE versus number of snapshots, second primary echo.

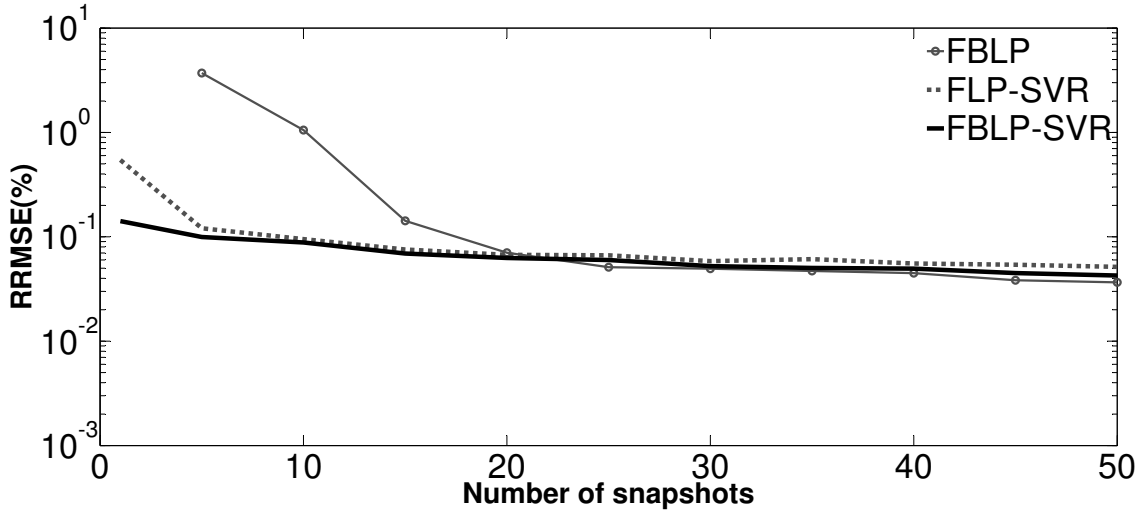

Figure 4.5 – RRMSEs of TDE versus number of snapshots, third primary echo.

4.4.4 Performance versus SNR

In the third simulation, the methods are applied to GPR data with different SNRs ranging from 0 dB to 30 dB. Only one snapshot is considered in this simulation. The standard FBLP can not work with a single snapshot. Thus, it is not presented in the comparison. The performance of FBLP-SVR and FLP-SVR is tested with a Monte Carlo process, which consists of 500 independent runs of the methods. Figures 4.6-4.8 show the RRMSEs of the three primary echoes using FBLP-SVR and FLP-SVR as a function of SNR. It can be seen that the RRMSEs of the three primary echoes continuously decrease as SNR increases. The estimation results of FBLP-SVR have lower RRMSEs than those of FLP-SVR. The RRMSE of the methods depends on the echo amplitude, that is, the larger the echo amplitude is, the smaller the RRMSE will be. The RRMSE difference between FBLP-SVR and FLP-SVR is the smallest for the third primary echo (in Figures 4.5 and 4.8), which might lie in the fact that the third echo is not overlapped with the other echoes.

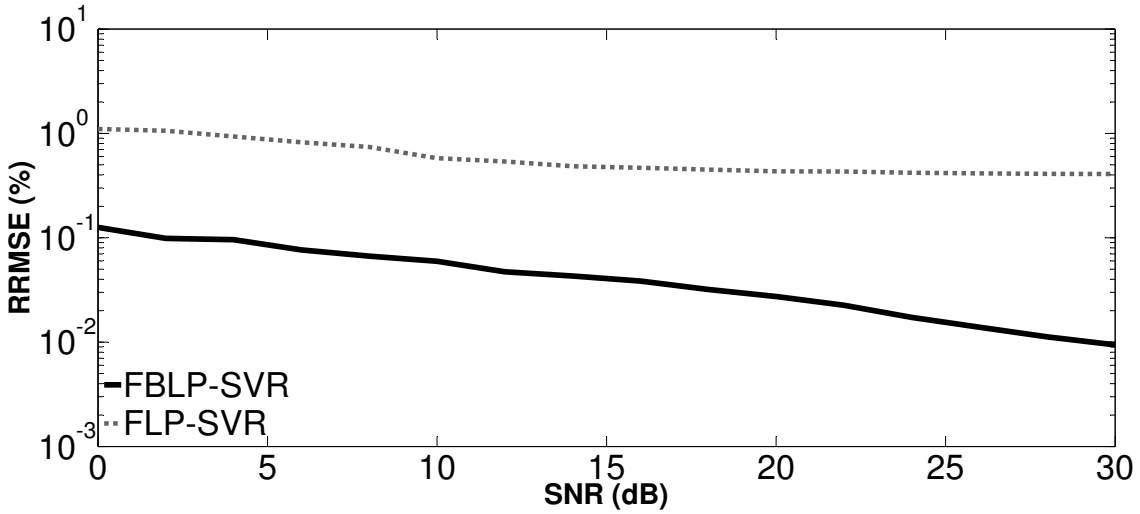

Figure 4.6 – RRMSEs of TDE versus SNR, first primary echo.

4.5 Experimental results

The proposed method is also tested with two experimental databases. The first experiment is conducted with a model medium. The second one is conducted with a pavement.

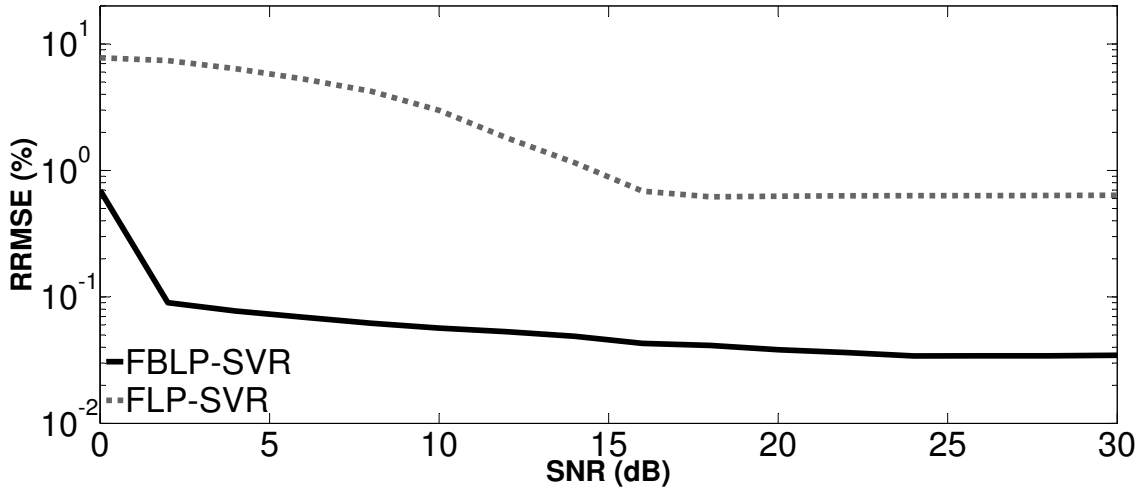

Figure 4.7 – RRMSEs of TDE versus SNR, second primary echo.

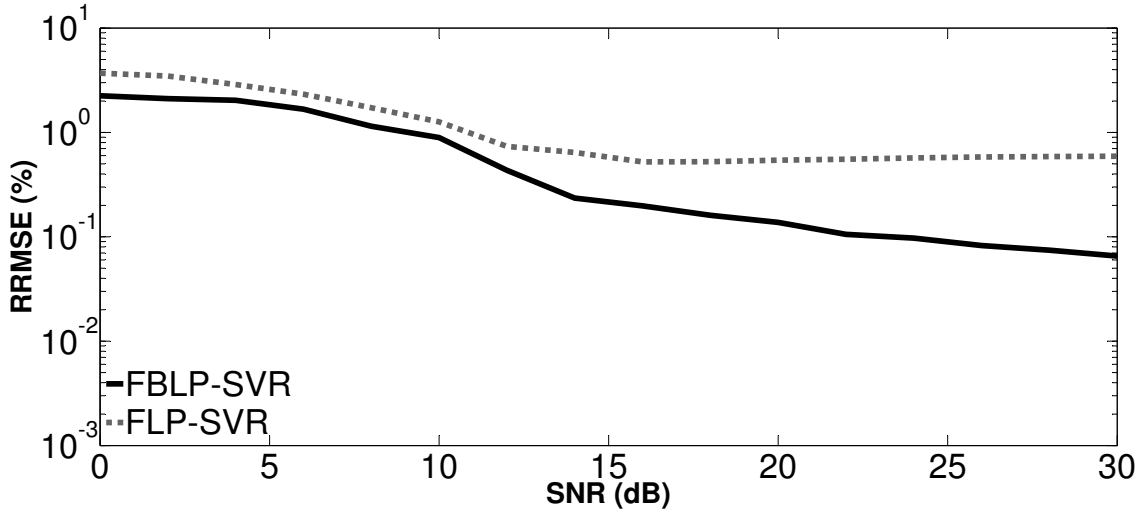

Figure 4.8 – RRMSEs of TDE versus SNR, third primary echo.

4.5.1 Laboratory experiment

In the first experiment, a polyvinyl chloride (PVC) slab is probed in laboratory by a monostatic step frequency radar in far-field, as shown in Figure 4.9. The radar is composed of a vector network analyzer (VNA) and an antenna which is the Transmitter (Tx) and Receiver (Rx). The frequency bandwidth is $f \in [1.6, 3]$ GHz, with $M = 71$ frequency samples. The height of the antenna is 70 cm. The PVC slab has a thickness of 4 cm and relative permittivity $\epsilon_r = 2.97 + 0.015j$. In this case, the product $B\Delta\tau$ is about 0.64 and the two backscattered echoes overlap with each other. The radar pulse is measured with a metal plane [9]. The data are acquired with a single snapshot.

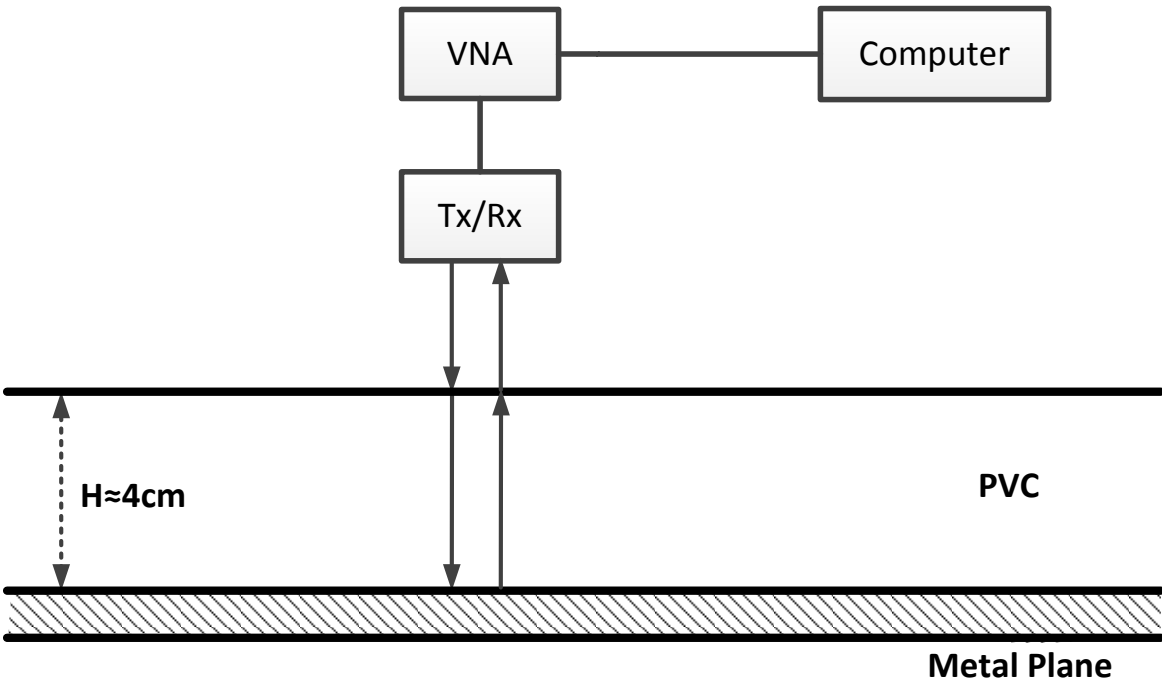

Figure 4.9 – Observation framework of GPR.

The measured GPR data are preprocessed with temporal filtering and data whitening, like in [9, 72]. After preprocessing, the proposed FBLP-SVR and FBLP are applied to TDE. The order of the prediction filter P is set to 70. Figure 4.10 illustrates the obtained results. The backscattered echoes are overlapped and correlated with each other and there is only one snapshot. The proposed FBLP-SVR can accurately detect the two echoes while FBLP fails because of the limitation on the number of snapshots ($L \geqslant P/[2(M-P)] = 35$). The relative error of FBLP-SVR in Figure 4.10–(c) is about 2.7%.

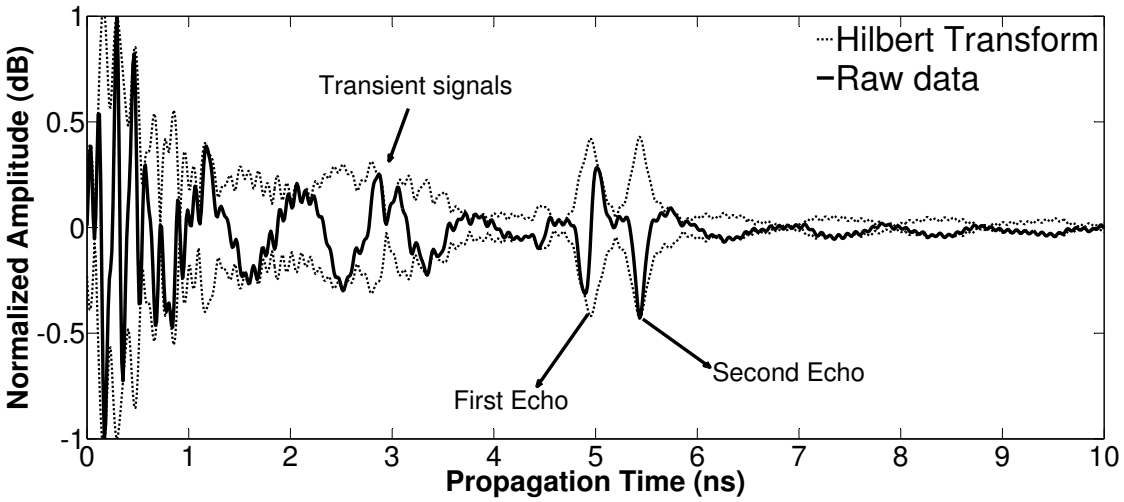

(a)

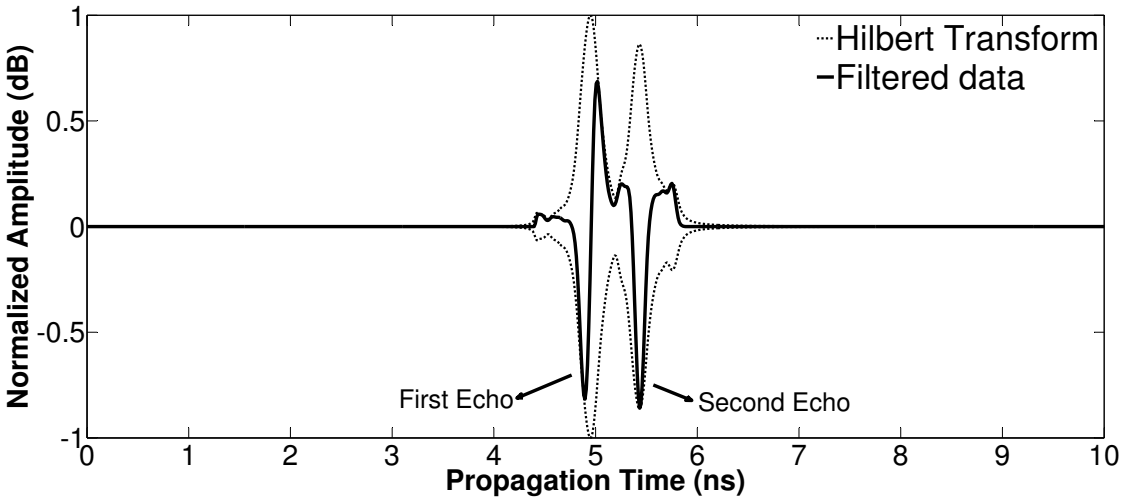

(b)

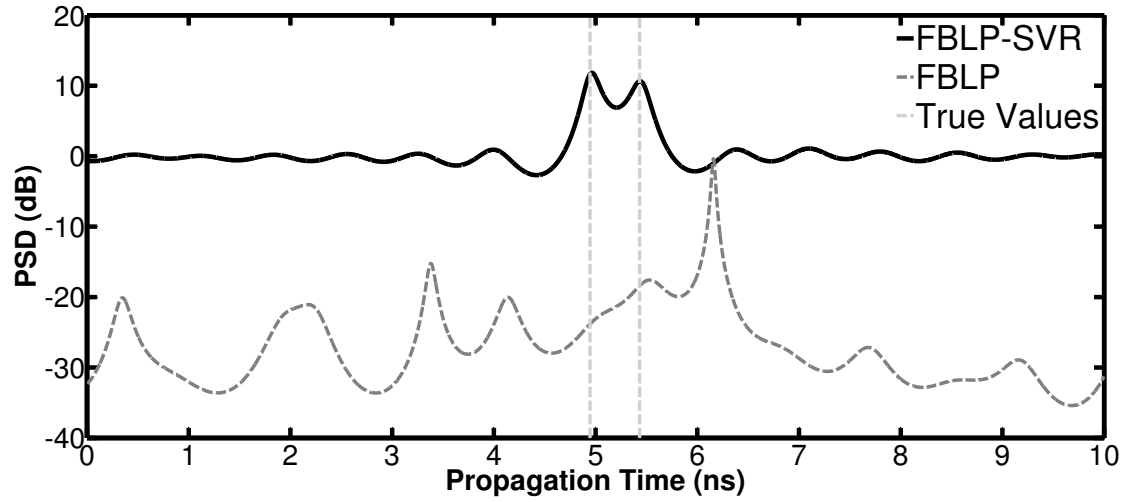

(c)

Figure 4.10 – Processing of GPR measurements. (a) Raw data. (b) Time-filtered data. (c) PSD of FBLP-SVR and FBLP ($B\Delta\tau \approx 0.64$).

4.5.2 Field experiment

An experiment is conducted to probe a pavement of IFSTTAR fatigue carousel [80]. The pavement consists of two layers of asphalt. The relative permittivities of the two layers are very close. The thickness of the first layer is about 5 cm. The measurement is carried out by a quasi-monostatic step frequency radar with closely located Tx and Rx antennas. The distance between Tx and Rx antennas is constant during the B-scan. The B-scan is composed of 21 traces (A-scans). During the measurement, the far-field condition is verified. Preprocessing techniques (filtering the air wave, data whitening) are performed before applying the proposed algorithm [9, 72]. By the inverse Fourier transform, we have the B-scan obtained from the experimental data without air wave with a large frequency band ($f \in [0.8, 10.8]$ GHz), as shown in Figure 4.11. There are two echoes and the time shift $\Delta\tau$ between them is about 1.07 ns.

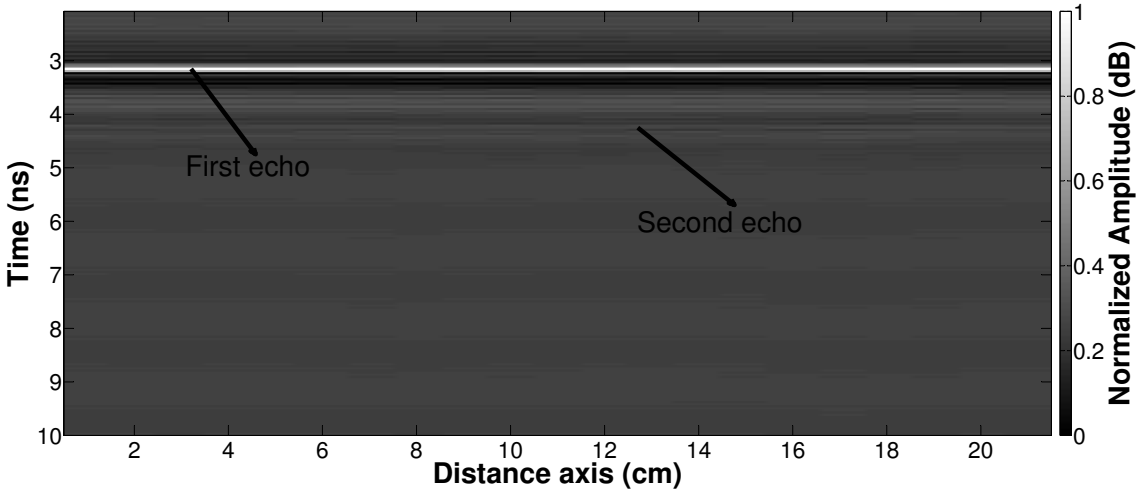

Figure 4.11 – Raw GPR data, B-scan with a large frequency band ($f \in [0.8, 10.8]$ GHz).

Figure 4.12 shows the B-scan obtained by the proposed FBLP-SVR using only one snapshot. The frequency band used in the estimation is $f \in [3.77, 4.42]$ GHz with 27 frequency elements. Thus, the product $B\Delta\tau$ is about 0.7, which means that the two echoes are overlapped. As expected, the two echoes are well resolved by FBLP-SVR over 21 A-scans. The prediction order P is set to 25. The standard FBLP can not work since the limitation on the number of snapshots is $L \geqslant 7$ and there is only one snapshot in the experiment. Figure 4.13 illustrates the results obtained by the proposed method and FBLP at the 5th trace of the B-scan (5th A-scan of Figure 4.11). The proposed method is able

to detect the two echoes, as shown in Figures 4.12 and 4.13. FBLP shows no peak at the position of true values.

In addition, the time-delays between the two echoes for the 21 A-scans are calculated. The mean and median of the estimated time shifts are 1.058 ns and 1.110 ns, respectively. The estimated time-delays are close to the real values.

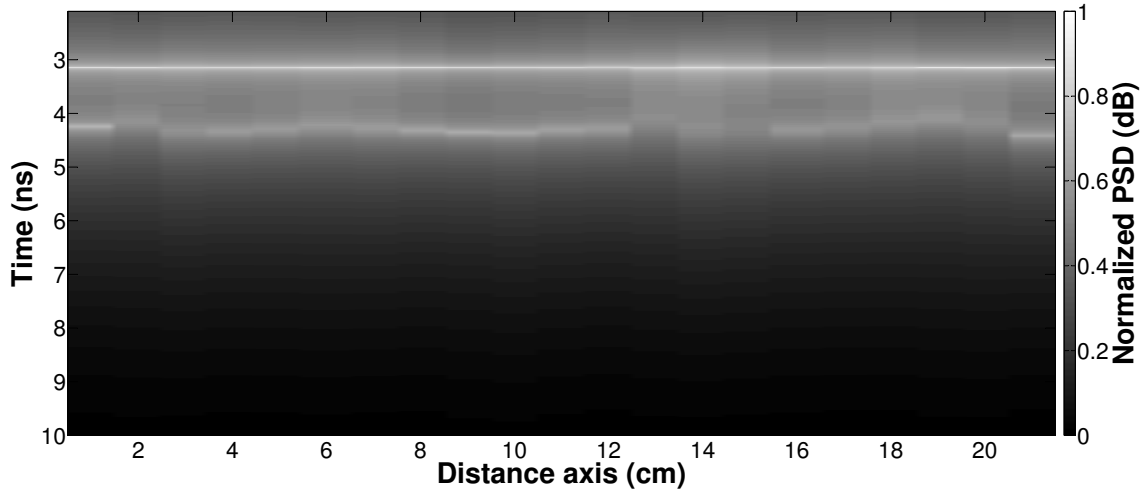

Figure 4.12 – Estimations using FBLP-SVR, B-scan, $f \in [3.77, 4.42]$ GHz.

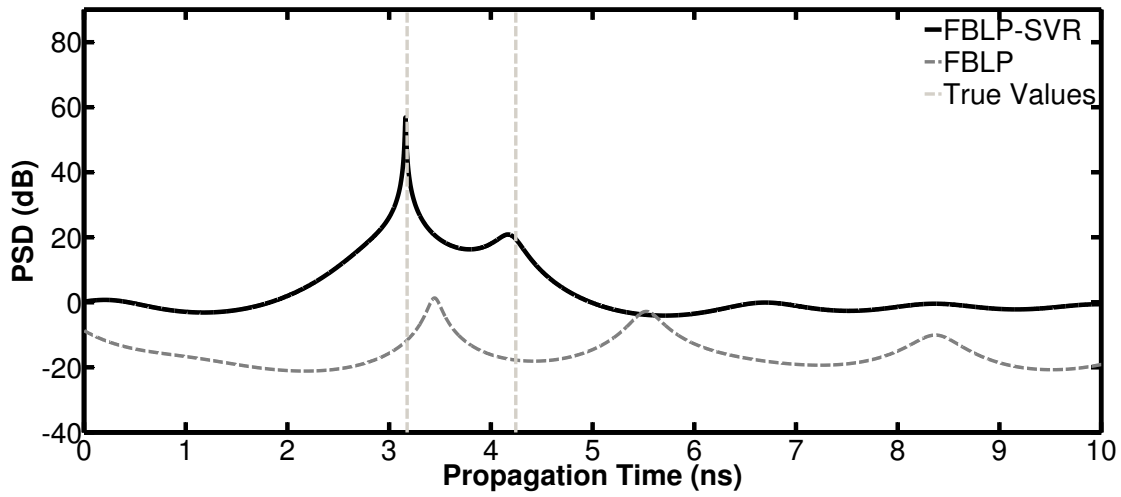

Figure 4.13 – PSD of FBLP and FBLP-SVR at the 5th A-scan.

4.6 Conclusion

In this chapter, the proposed FBLP-SVR is extended to estimate the time-delays of the backscattered echoes within stratified medium by using GPR. Wirtinger's calculus is used to directly deal with complex-valued signals. The performance of FBLP-SVR is validated with numerical and experimental data, in coherent scenarios with both overlapping and non-overlapping signals and limited snapshots. The proposed FBLP-SVR outperforms the traditional FBLP and FLP-SVR methods, especially when the number of snapshots is low. Furthermore, FBLP-SVR is applicable with only one snapshot.

5

Proposed source localization method in near-field

5.1 Introduction

In Chapter 3, we propose a source localization method in far-field in coherent scenarios. In far-field, the wavefronts of signals are planar and there is only one parameter (DOA) in the estimation. However, when the sources are in near-field, the wavefronts of signals become spherical and both the range and DOA are necessary in source localization. Several methods have been proposed in near-field source localization, for example, 2D MUSIC, ML [38], the weighted linear prediction method [39], the symmetric method [40], the anti-diagonal method [42], the focusing method [43], and the sub-array processing (SAP) method [44, 45]. Most of the methods (except ML) require EVD, as summarized in Table 2.3. However, EVD-based methods can not work in coherent scenarios. Besides, the SSP procedures in [13, 30] can not be directly applied to decorrelate signals, since the phase shifts are nonlinear in near-field. The SAP technique can work with coherent signals. But it requires a large number of sensors and a large angle separation between sources, which is not efficient with closely located sources. The principle of ML doesn't depend on signal or noise subspaces and it can deal with coherent signals. However, it needs multidimensional

searching, which is computational demanding.

In this chapter, we focus on the localization of two closely located sources in near-field and in coherent scenarios. The focusing technique in [43] is able to transform the near-field signal model into a far-field-like one. Then, we can apply SSP to decorrelate the coherent signals. The DOA of each source can then be estimated by using far-filed source localization methods. The range can be estimated by using ML with the estimated DOAs and pre-estimate of ranges. In this case, the searching complexity of ML is greatly reduced.

5.2 Signal model

The near-field signal model used in this chapter is presented in Section 2.3. We assume a ULA with $M = 2N + 1$ elements and K narrow band sources locating within $\mathbf{r}_F = [0.62(D^3/\lambda)^{1/2},\ 2D^2/\lambda]$, as shown in Figure 5.1. Contrary to Section 2.3, the sources are considered as coherent in this chapter.

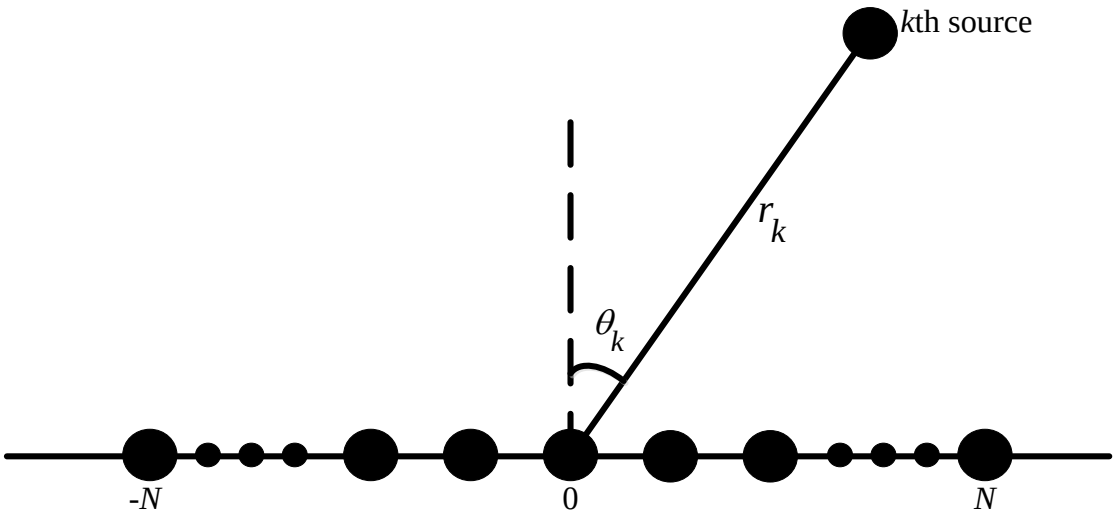

Figure 5.1 – Uniform linear array configuration in near-field source localization.

According to (2.43), the output of sensors in vector form can be formulated as

$$\mathbf{x}(t) = \mathbf{A}\mathbf{s}(t) + \mathbf{n}(t) \tag{5.1}$$

where $\mathbf{s}(t) = [s_1(t), \ldots, s_K(t)]^T$ is the signal vector; $\mathbf{n}(t) = [n_{-N}(t), \ldots, n_N(t)]^T$ is the noise vector; $\mathbf{A}$ is the mode matrix given by $\mathbf{A} = [\mathbf{a}(r_1, \theta_1), \ldots, \mathbf{a}(r_K, \theta_K)]$, with steering

vector $\mathbf{a}(r_k, \theta_k)$:

$$\mathbf{a}(r_k, \theta_k) = \begin{bmatrix} e^{j(2\pi \frac{d}{\lambda} \sin\theta_k)N + j(\frac{\pi d^2}{\lambda r_k} \cos^2\theta_k)N^2} \\ \vdots \\ e^{j(2\pi \frac{d}{\lambda} \sin\theta_k)(-N) + j(\frac{\pi d^2}{\lambda r_k} \cos^2\theta_k)N^2} \end{bmatrix}. \tag{5.2}$$

The covariance matrix of the received signals is $\mathbf{R} = E[\mathbf{x}(t)\mathbf{x}^H(t)] = \mathbf{A}\mathbf{R}_s\mathbf{A}^H + \sigma^2\mathbf{I}$.

5.3 Proposed method

The flowchart of the proposed method is shown in Figure 5.2. Before applying the focusing technique, a pre-estimation of the parameters (DOA and range) is carried out by using beamforming. Then, we form a focusing matrix to transform the near-field signal model into a far-field-like one. After the focusing process, the DOAs can be estimated using SSP and a subspace method (MUSIC or ESPRIT). Finally, the range can be estimated by using ML and the previously estimated parameters.

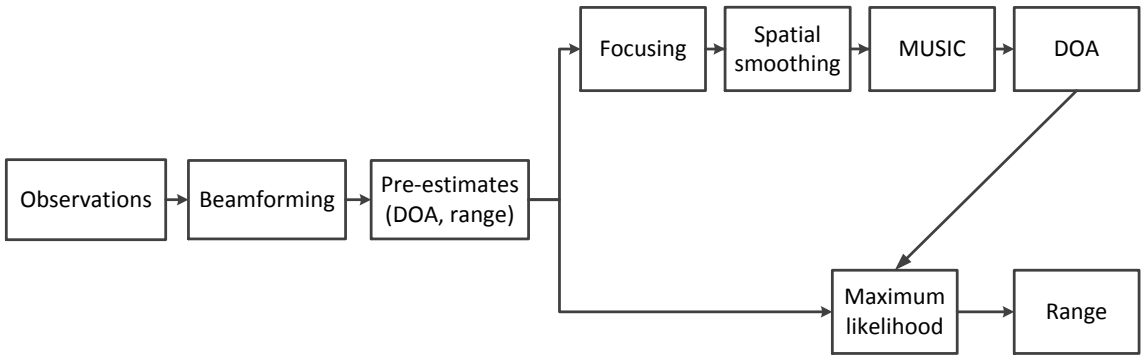

Figure 5.2 – Flowchart of the proposed method.

5.3.1 Pre-estimation: beamforming

The beamforming method is necessary to roughly estimate the positions of the sources before the focusing technique. The positions of sources can be estimated by searching the spectrum of the output power as follows:

$$P(r, \theta) = \mathbf{a}(r, \theta)^H \mathbf{R}\mathbf{a}(r, \theta) \tag{5.3}$$

where $r \in \mathbf{r}_F$ and $\theta \in [-\pi/2, \pi/2]$.

The resolution of the classical beamforming method is limited to the Rayleigh resolution [15]. Thus, the closely located sources are mixed up in the power spectrum.

5.3.2 Focusing technique-particular case

We assume that the sources are closely located. Thus, there will be only one peak in beamforming. Let r_e and θ_e be the corresponding estimates. The diagonal focusing matrix $\mathbf{C}$ can be expressed as:

$$\mathbf{C} = diag[e^{-j(\frac{\pi d^2}{\lambda r_e}\cos^2\theta_e)(-N)^2}, \ldots, e^{-j(\frac{\pi d^2}{\lambda r_e}\cos^2\theta_e)(N)^2}]. \tag{5.4}$$

Then, we can build the focused covariance matrix $\mathbf{R}'$ as follows:

$$\begin{aligned} \mathbf{R}' &= \mathbf{C}\mathbf{R}\mathbf{C}^H \\ &= (\mathbf{C}\mathbf{A})\mathbf{R}_s(\mathbf{C}\mathbf{A})^H + \sigma^2\mathbf{I}. \end{aligned} \tag{5.5}$$

The matrix $(\mathbf{CA})$ has the same structure as the mode matrix in far-field. Since the signals are coherent and the focused signal model is linear, SSP techniques in Section 2.2.4 can be used to decorrelate signals. Then, we can estimate the DOA by using subspace methods, for example, MUSIC. Let $\hat{\theta}_k$ be the estimate of θ_k, $k = 1, 2$.

5.3.3 ML

As introduced in Section 2.3.2, the range and DOA of each source are estimated by ML with the following expression:

$$\max_{\mathbf{A}} \; tr(\mathbf{\Pi}_\mathbf{A}\mathbf{R}) \tag{5.6}$$

where $\mathbf{\Pi}_\mathbf{A} = \mathbf{A}(\mathbf{A}^H\mathbf{A})^{-1}\mathbf{A}^H$.

The matrix $\mathbf{A} = [\mathbf{a}(r_1, \theta_1), \ldots, \mathbf{a}(r_K, \theta_K)]$ is composed of $2K$ unknown variables and $r_k \in \mathbf{r}_F$, $\theta_k \in [-\pi/2, \pi/2]$, $k = 1, \ldots, K$.

With the estimated DOA $\hat{\theta}_k$ and the pre-estimate of range r_e, the range of each source can be estimated by using ML.

5.4 Simulation

Consider a ULA with 11 isotropic sensors (i.e., $N = 5$). The distance between two adjacent sensors is $d = \text{l}/5\lambda$ to avoid phase ambiguity. The Fresnel region of this array is $\mathbf{r}_F = [1.75\lambda, 8\lambda]$. Two coherent sources locate at $(4.0\lambda, 0°)$ and $(3.8\lambda, 10°)$, respectively.

5.4.1 DOA and range estimation

Beamforming method is firstly used to obtain the pre-estimates of DOA and range by searching the peak of the PSD, as shown in Figure 5.3. 1000 snapshots are used and SNR = 20 dB.

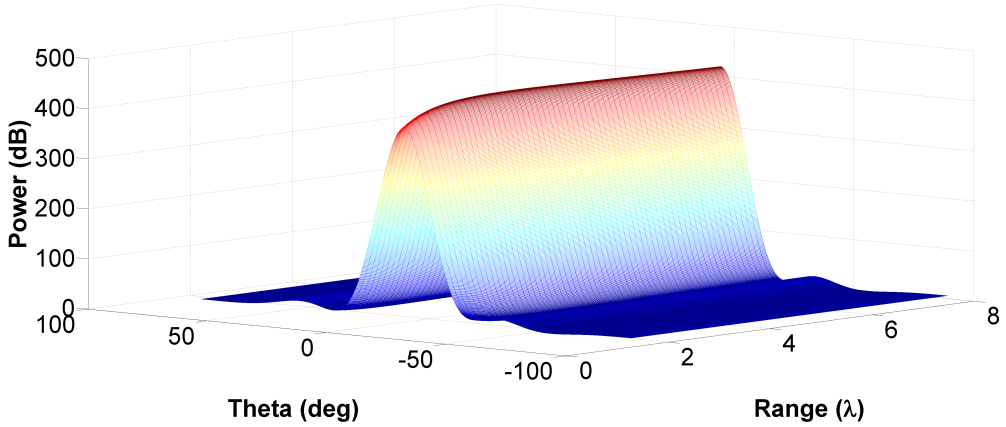

Figure 5.3 – Beamforming spectrum. Two sources locate at $(4.0\lambda, 0°)$ and $(3.8\lambda, 10°)$. The number of snapshots = 1000. SNR = 20 dB.

Then, the focusing technique, SSP, and MUSIC are applied. We can estimate the DOA and range of each source. Figure 5.4 shows the pseudo spectrum of MUSIC for the estimation of DOA. We can see that the estimated DOAs are close to the true values. Figure 5.5 shows the result from ML in the estimation of range. Since there are two sources in the simulation, the range estimation by using ML requires a 2D search. The maximum of the 2D spectrum indicates the estimates of range.

5.4.2 Performance versus SNR

The RMSE defined in (3.6) is used to analyze the behavior of the proposed method at different values of SNRs. Furthermore, the CRLB for near-field source localization (see in Appendix A) is added for comparison. The estimation results are collected over 200 Monte

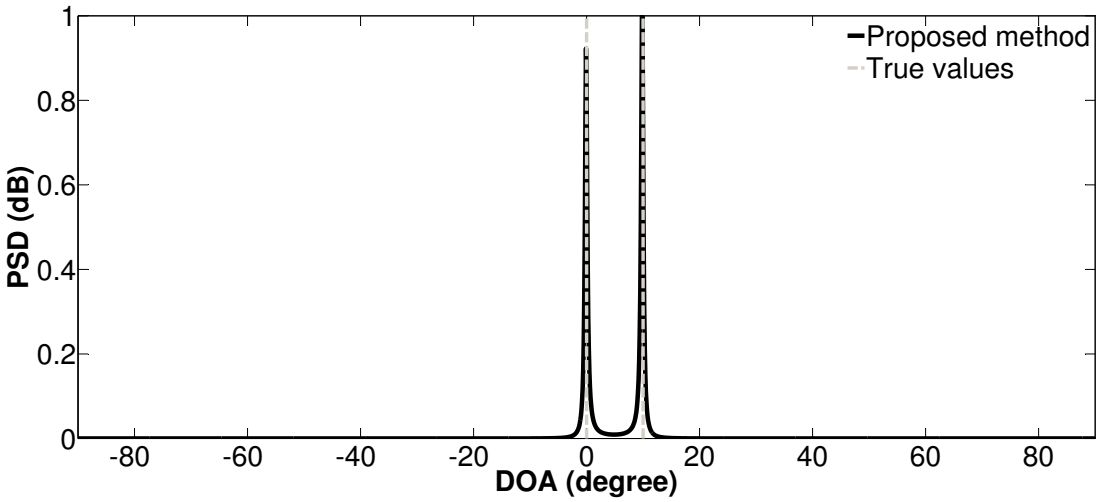

Figure 5.4 – Spectrum of DOA estimation by using focusing technique, SSP, and MUSIC.

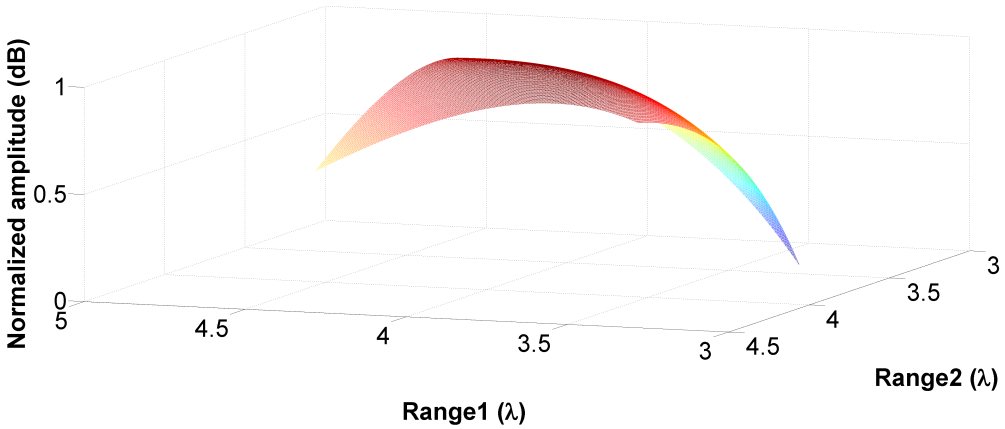

Figure 5.5 – Spectrum of range estimation by using ML.

Carlo trials. The number of snapshots is set to 1000. Figures 5.6 and 5.7 illustrate the RMSE of the estimated DOA and range, respectively.

In Figures 5.6 and 5.7, the RMSE of both sources decreases as SNR increases, , not only in the estimation of DOA but also in range.

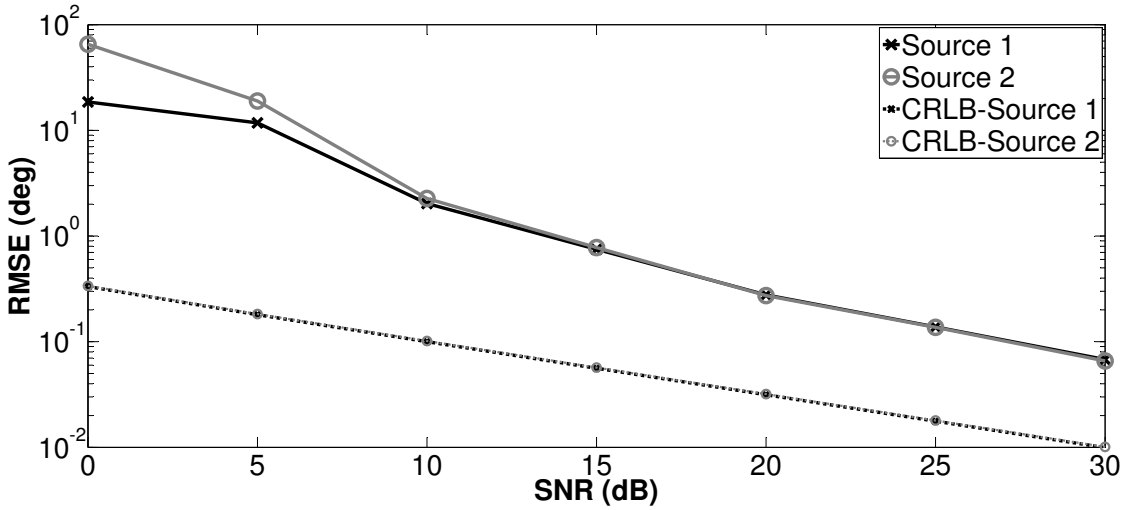

Figure 5.6 – Performance of the proposed method versus SNR, DOA estimation. Two coherent sources locate at $(4.0\lambda, 0°)$ and $(3.8\lambda, 10°)$. The number of snapshots = 1000.

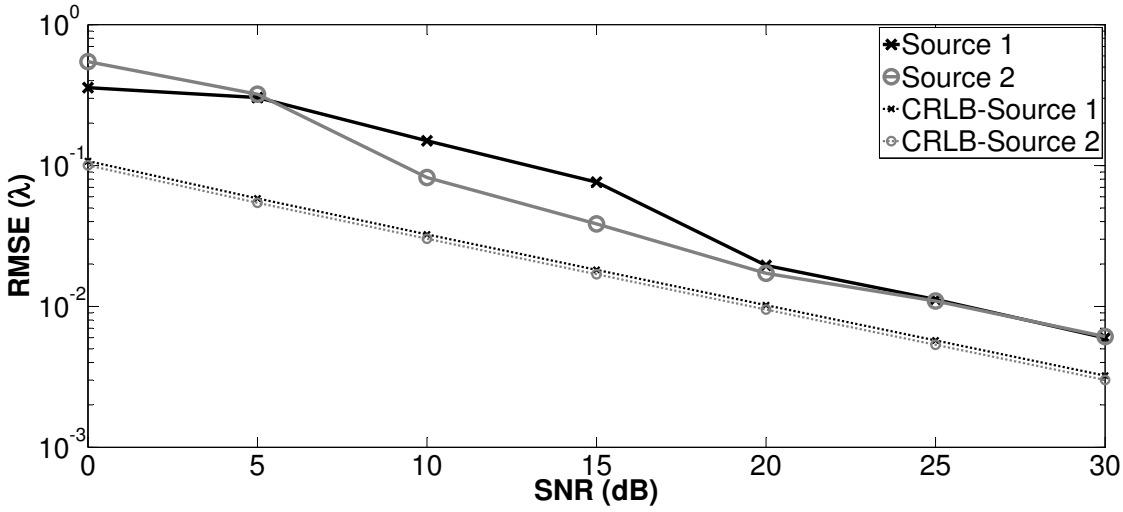

Figure 5.7 – Performance of the proposed method versus SNR, range estimation. Two coherent sources locate at $(4.0\lambda, 0°)$ and $(3.8\lambda, 10°)$. The number of snapshots = 1000.

5.4.3 Performance versus number of snapshots

Then, the performance is evaluated with different numbers of snapshots. The number of Monte Carlo process is also set as 200. SNR is fixed at 15 dB. Figures 5.8 and 5.9 show the estimation results for DOA and range, respectively. When the number of snapshots increases, the RMSE of the estimation of DOA and range decreases.

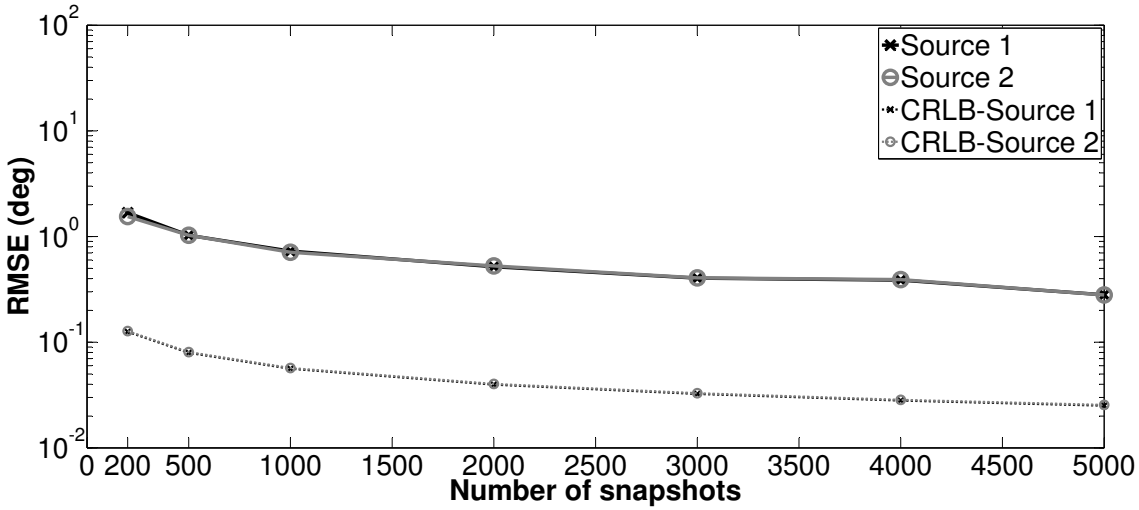

Figure 5.8 – Performance of the proposed method versus number of snapshots, DOA estimation. Two coherent sources locate at $(4.0\lambda, 0°)$ and $(3.8\lambda, 15°)$. SNR = 15 dB.

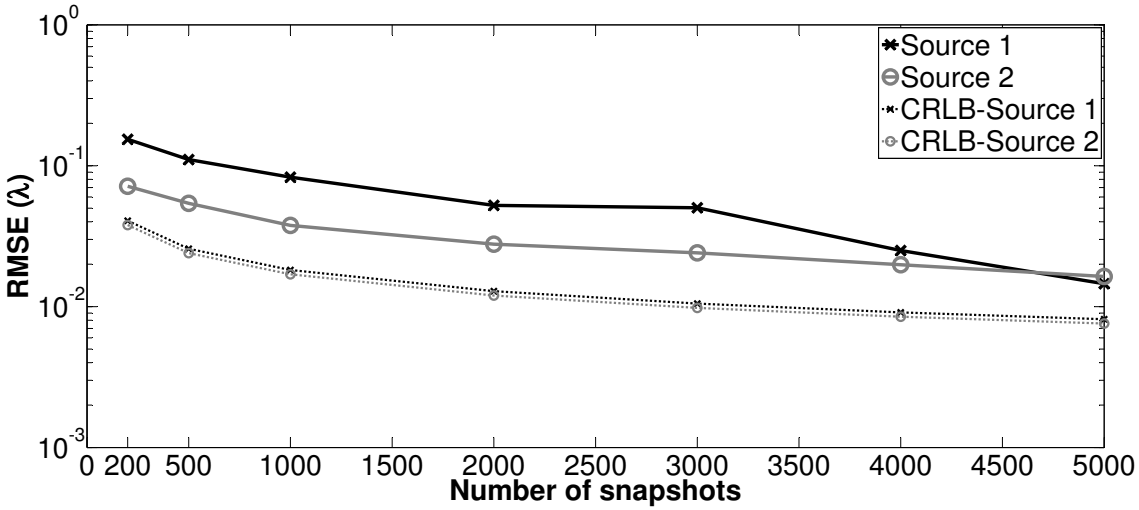

Figure 5.9 – Performance of the proposed method versus number of snapshots, range estimation. Two coherent sources locate at $(4.0\lambda, 0°)$ and $(3.8\lambda, 15°)$. SNR = 15 dB.

5.5 Conclusion

In this chapter, a method is proposed to localize two closely located near-field sources in coherent scenarios. The proposed method firstly makes use of the focusing technique to transform the near-field signal model into a far-field-like one. Then, the SSP decorrelation technique and MUSIC are applied in the estimation of DOA. The ranges are estimated by using ML and the estimated DOAs. Simulation results show the performance of the proposed method.

6

Conclusion and perspectives

6.1 Conclusion

Source localization (in far-field or near-field) and time-delay estimation (TDE) are of great importance in practical engineering applications, for example, radar, communication, civil engineering. In this thesis, we focus on the development of new signal processing methods in source localization (both far-field and near-field) and the estimation of time-delay (civil engineering) in problematic scenarios (coherent signals, limited number of snapshots) and with high resolution.

Chapter 2 firstly presents the signal models for far-field and near-field source localization. Then, several signal processing methods are described in each field. In particular, the signal model for TDE can be viewed as an extension of the signal model in far-field. Therefore, source localization methods in far-field can be applied to TDE. The theory of SVR is introduced to estimate DOAs in far-field, by using the traditional training and testing process.

In Chapter 3, we propose to combine FBLP and SVR in the estimation of DOA in far-field. SVR is a sparse machine learning method. It can work with a limited number of samples. FBLP has high resolution and performs SSP implicitly. To combine both methods, the complex variables in FBLP are converted into the corresponding real and imaginary parts. The behavior of the proposed method is analyzed with respect to SNR, number of

snapshots, and steering vector uncertainty. Numerical simulations show the robustness of the proposed method with a limited number of snapshots and coherent signals.

Chapter 4 extends the proposed FBLP-SVR to estimate the time-delays of backscattered echoes from a stratified medium by using GPR. Since the signal model of source localization methods in far-field is close to that of TDE, the proposed FBLP-SVR works in TDE as well. Contrary to Chapter 3, the complex variables in FBLP-SVR are formulated directly in the complex domain with Wrintinger's calculus. The performance of FBLP-SVR in TDE is validated with numerical and experimental data, in coherent scenarios with both overlapped and non-overlapped echoes, and a limited number of snapshots.

In Chapter 5, we propose a near-field source localization method in coherent scenarios. The proposed method makes use of the focusing technique to transform the near-field signal model into a far-field one. Then, SSP and subspace methods can be applied to estimate the DOAs of coherent incoming signals. The range is estimated by ML with the estimated DOAs. Simulations demonstrate the effectiveness of the proposed method.

6.2 Perspectives

In this thesis, we propose to combine the sparse machine learning method SVR with existing signal processing methods in source localization and the estimation of time-delay. But much work remains to be done.

The SVR adopted in this thesis can only deal with single-output cases. Therefore, an extension of SVR in multi-output cases like in [81] would be interesting, especially in the complex domain. Moreover, the multi-output SVR (M-SVR) can also be used in the training and testing of multiple parameters, for example, DOA and range in near-field source localization, and time-delay, permittivity, thickness, roughness in GPR pavement measurements.

Besides, SVR in this thesis is combined with LP methods. We also would like to combine SVR with other linear signal processing methods in the future, for example, propagator methods.

In source localization problems, we use the simplest observation framework ULA in Chapters 3 and 5. However, other configurations, nested array [82], co-prime array [83], multiple-input multiple-output (MIMO) radar, provide more benefits, for example, improved resolution, higher degrees of freedom. Another future concern is the investigation of these configurations in source localization and parameter estimation with SVR.

Moreover, the proposed near-field source localization method in Chapter 5 works only with two closely located sources in coherent scenarios. The estimation of DOA is based on the focusing technique. More rigorous researches are required to deal with more than two sources and with a lower computational complexity.

In addition, the effectiveness of the proposed methods in source localization (both far-field and near-field) would be more convincing with some experimental data.

A

Cramér-Rao Lower Bound (CRLB)

In estimation theory, CRLB serves as a limit on the variance of an unbiased estimator with which we can compare the performance of the proposed method [84]. The CRLB is derived by the reciprocal of the Fisher information matrix, which contains all the information about the unknown parameters. In source localization problems, the expression of CRLB has been studied not only in far-field [85, 70] but also in near-field [39].

According to [70], the closed-form expression for CRLB in far-field is as follows:

$$\mathbf{CRLB}_f = \frac{\sigma^2}{2L}\{\Re((\mathbf{F}^H\mathbf{\Pi}_{\mathbf{A}}^{\perp}\mathbf{F}) \odot (\mathbf{R}_s\mathbf{A}^H\mathbf{R}^{-1}\mathbf{A}\mathbf{R}_s)^T)\}^{-1} \tag{A.1}$$

where $\odot$ denotes the Hadamard-Schur product; $\mathbf{A} = [\mathbf{a}(\theta_1), \ldots, \mathbf{a}(\theta_K)]$ is the mode matrix in far-field source localization and

$$\mathbf{\Pi}_{\mathbf{A}}^{\perp} = \mathbf{I} - \mathbf{\Pi}_{\mathbf{A}};$$

$$\mathbf{\Pi}_{\mathbf{A}} = \mathbf{A}(\mathbf{A}^H\mathbf{A})^{-1}\mathbf{A}^H;$$

$$\mathbf{F} = \begin{bmatrix} \mathbf{f}(\theta_1) & \ldots & \mathbf{f}(\theta_K) \end{bmatrix};$$

$$\mathbf{f}(\theta_k) = \frac{\partial \mathbf{a}(\theta_k)}{\partial \theta}, \; k = 1, \ldots, K.$$

Similarly, the expression of CRLB for DOA and range in near-field is formulated as

[39]:

$$\mathbf{CRLB}_n = \frac{\sigma^2}{2L}\{\Re((\mathbf{F}^H\mathbf{\Pi}_{\mathbf{A}}^{\perp}\mathbf{F}) \odot (\mathbf{1}_{2\times 2} \otimes (\mathbf{R}_s\mathbf{A}^H\mathbf{R}^{-1}\mathbf{A}\mathbf{R}_s)^T))\}^{-1} \tag{A.2}$$

where $\otimes$ denotes the Kronecker product; $\mathbf{A} = [\mathbf{a}(r_1, \theta_1), \ldots, \mathbf{a}(r_K, \theta_K)]$ is the mode matrix in near-field source localization;

$$\mathbf{1}_{2\times 2} = \begin{bmatrix} 1 & 1 \\ 1 & 1 \end{bmatrix};$$

$$\mathbf{F} = \begin{bmatrix} \mathbf{f}_\theta(r_1, \theta_1) & \ldots & \mathbf{f}_\theta(r_K, \theta_K) & \mathbf{f}_r(r_1, \theta_1) & \ldots & \mathbf{f}_r(r_K, \theta_K) \end{bmatrix};$$

$$\mathbf{f}_\theta(r_k, \theta_k) = \frac{\partial \mathbf{a}(r_k, \theta_k)}{\partial \theta},\ k = 1, \ldots, K;$$

$$\mathbf{f}_r(r_k, \theta_k) = \frac{\partial \mathbf{a}(r_k, \theta_k)}{\partial r},\ k = 1, \ldots, K.$$

B

Parameter sensitivity analysis of FBLP-SVR in TDE

In this appendix, we present a sensitivity analysis of FBLP-SVR. This analysis is carried out for TDE, but similar results can be observed in the estimation of DOA in far-field.

In linear SVR models, three parameters should be analyzed, namely, the regularization parameter C, the epsilon parameter ϵ and the parameter γ. In fact, there are several ways to determine the SVR parameters, for example, the criterion of Cherkassky [86], cross validation [87], particle swarm optimization [88], and gradient descent algorithm [89]. Most of these criteria depend on the prior distribution of the data (a large dataset is required [86, 87]) or an initial start [89]. However, the numbers of snapshots in our simulations are too small to provide sufficient statistical information, $L \in [1, 5, \dots]$. This group of parameters ($\epsilon = 0$, $C = 1$ and $\gamma = 10^{-6}$) has shown its robustness under different conditions in TDE, which will be presented in the following simulations.

B.1 Performance versus C

Firstly, we test the performance of FBLP-SVR at different values of C. The simulation setup is the same as Section 4.4.1. There are 3 layers in the stratified medium associated with 3 primary echoes (the multiple echo is not estimated). Only 5 snapshots are used here.

The range of C is set as [1, 5, 10, 50, 100]. $\epsilon = 0$, $\gamma = 10^{-6}$ and SNR = 15 dB. Figure B.1 shows the PSD of the proposed FBLP-SVR with different values of C.

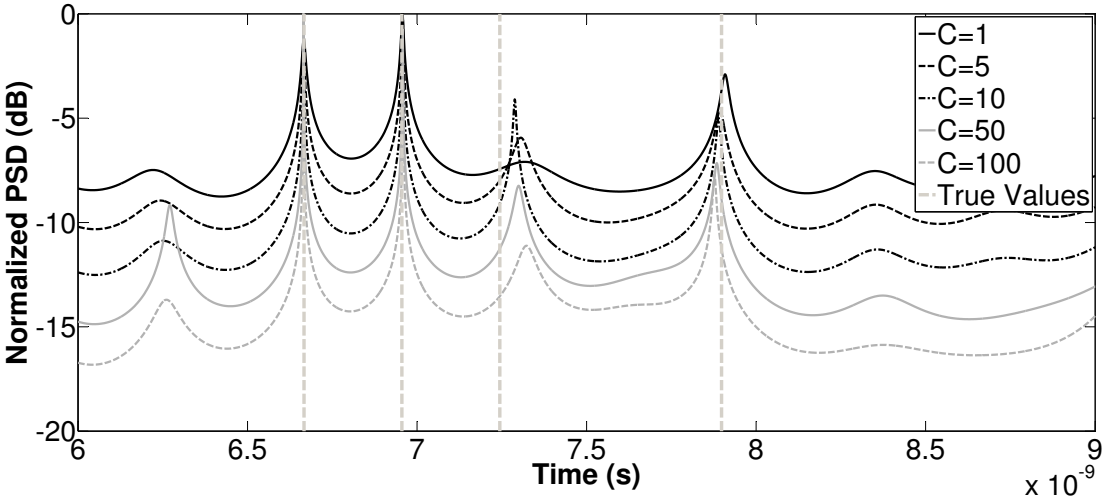

Figure B.1 – PSD of FBLP-SVR for different values of C. $\epsilon = 0$, $\gamma = 10^{-6}$, $L = 5$ and SNR = 15 dB.

From Figure B.1, it is clear that all the values of C can successfully estimate the three primary echoes.

B.2 Performance versus ϵ

Similarly, we test the performance of the proposed method with different values of ϵ. The results are shown in Figure B.2.

In our experience, the value of ϵ should not be too big. When $\epsilon = 0.1$, the third primary echo is undetectable. But the other settings of ϵ can successfully detect the three peaks.

B.3 Performance versus γ

Parameter γ is also set at different values, as shown in Figure B.3.

We can see in Figure B.3 that the performance of the proposed method is similar at different values of γ, even though the value of γ changes greatly (from 10^{-6} to 10^{-2}). All curves have peaks around the true values.

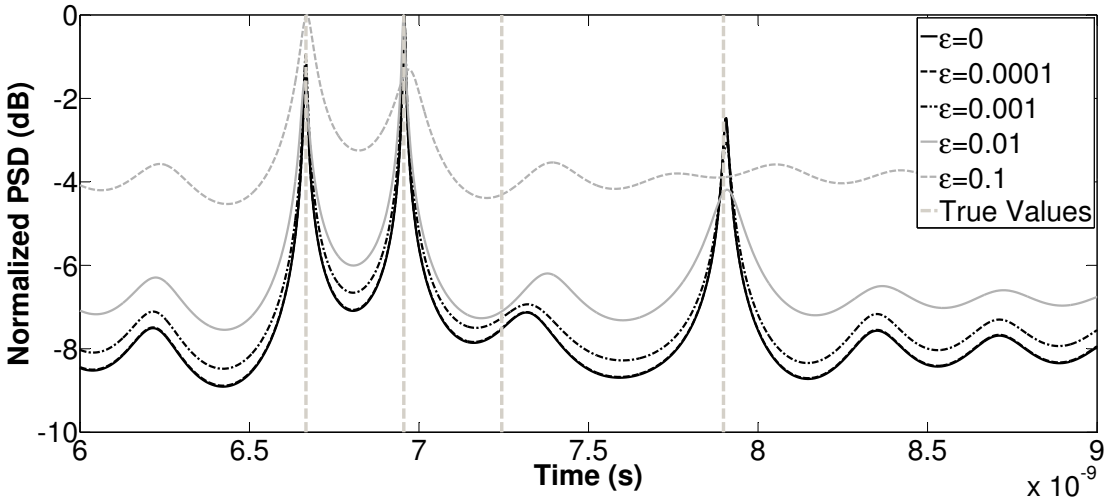

Figure B.2 – PSD of FBLP-SVR for different values of ϵ. $C = 0$, $\gamma = 10^{-6}$, $L = 5$ and SNR = 15 dB.

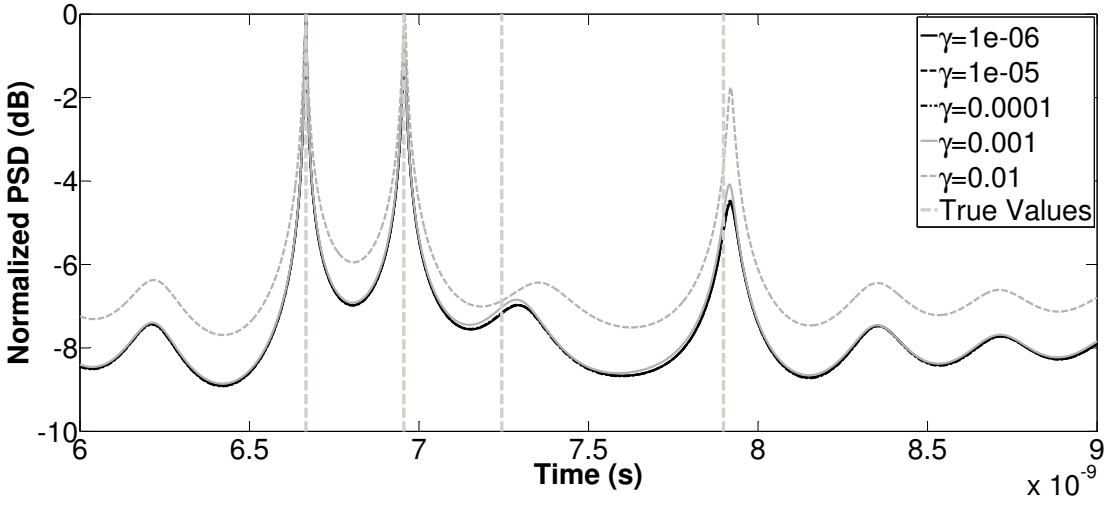

Figure B.3 – PSD of FBLP-SVR for different values of γ. $\epsilon = 0$, $C = 1$, $L = 5$ and SNR = 15 dB.

B.4 Performance versus number of snapshots

The group of parameters ($\epsilon = 0$, $C = 1$ and $\gamma = 10^{-6}$) is tested with 500 Monte Carlo trials. Similarly, both $L = 5$ and $L = 50$ are considered. The means and standard deviations of the three estimates (the three primary echoes) are calculated, which are shown in Table B.1.

Table B.1 – Means and standard deviations of TDE with 5 and 50 snapshots. $\gamma = 10^{-6}$, $\epsilon = 0$, $C = 1$ and SNR = 15 dB.

	True Value	L = 5		L = 50	
		Mean	Standard Deviation	Mean	Standard Deviation
τ_1 (s)	6,667e-09	6,667e-09	1,290e-11	6,667e-09	1,064e-12
τ_2 (s)	6,955e-09	6,956e-09	1,319e-11	6,956e-09	1,205e-12
τ_3 (s)	7,898e-09	7,841e-09	1,859e-10	7,879e-09	1,182e-10

From Table B.1, we can see that the mean values are close to the true values; the standard deviations are small; the results with $L = 50$ are more accurate than that with $L = 5$.

B.5 Performance versus SNR

The performance of FBLP-SVR is also assessed for different values of SNR. The medium is the same as in Section 4.4.1. SVR parameters are fixed as $\gamma = 10^{-6}$, $\epsilon = 0$, $C = 1$ and the number of snapshots $L = 5$. The means and standard deviations of the estimates of the three primary echoes are shown in Figure B.4.

Figure B.4 shows that the mean values of the three estimates are closer to the true values as SNR increases. The standard deviations of the three echoes decrease with the increase of SNR. This group of parameters can work at different SNRs.

B.6 Performance versus thickness

Moreover, we would like to see the performance of the proposed FBLP-SVR for different thicknesses. In this section, one medium composed of two layers is considered, as shown in Figure B.5. Layer 1 is a pavement, and Layer 2 is a semi-infinite pavement.

Two time-delays, i.e., τ_0 and τ_1, are considered. The frequency range of the step frequency radar is $[1.0 - 3.0]$ GHz. The relative permittivities of Layers 1 and 2 are 3 and

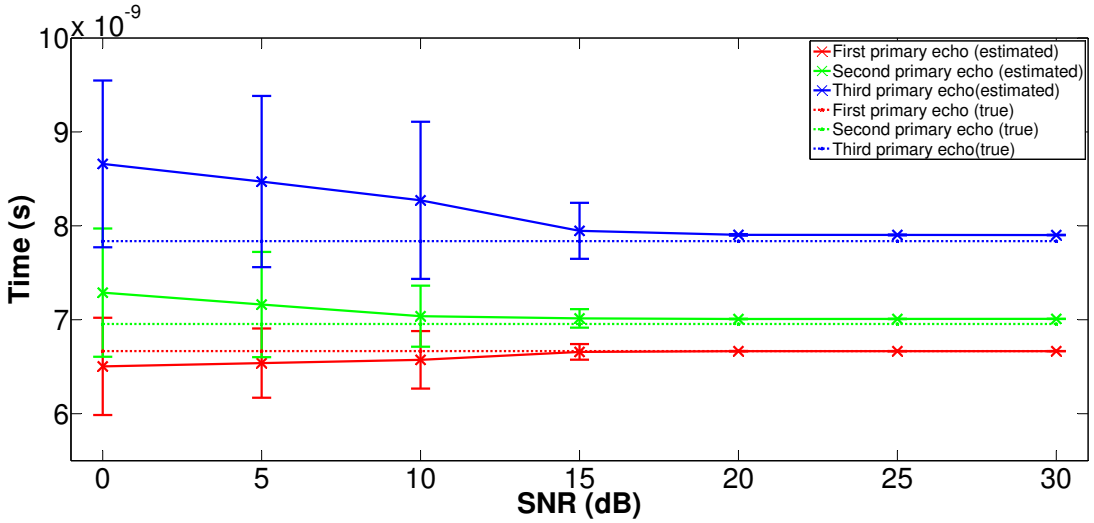

Figure B.4 – Error bar of TDE using FBLP-SVR with 500 Monte Carlo trials and different values of SNR. Data are expressed as mean $\pm$ standard deviation. $\gamma = 10^{-6}$, $\epsilon = 0$, $C = 1$ and $L = 5$.

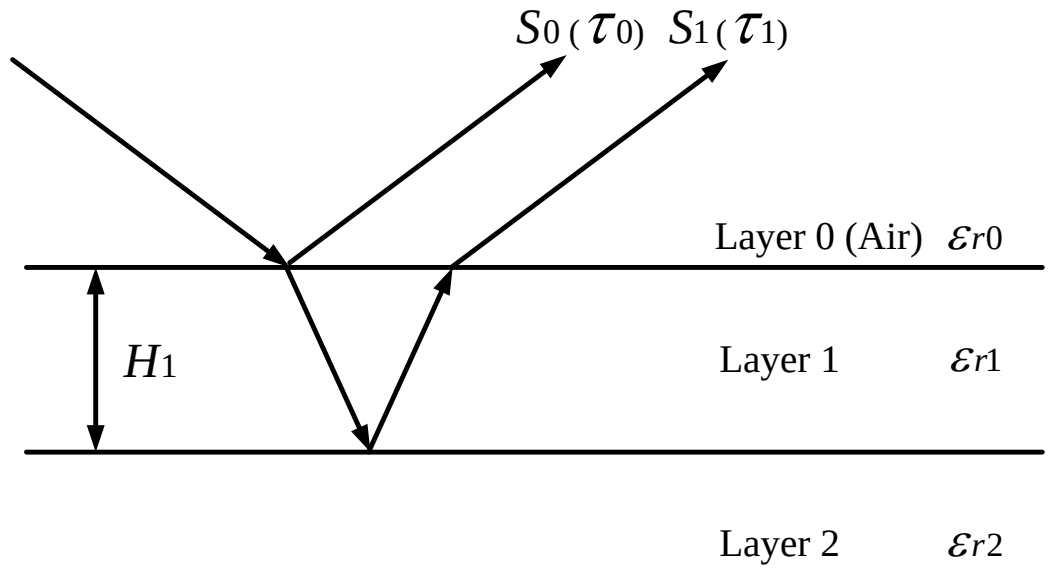

Figure B.5 – Profile of a stratified medium.

8, respectively. The thickness of Layer 1 is set at different values to have different $B\Delta\tau$ ($\Delta\tau = \tau_1 - \tau_0$).

The rate of failures is assessed with 500 Monte Carlo trials. A trial is considered as successful only when the estimates of the two time-delays are within $[\tau_0 - \Delta\tau/2, \tau_1 + \Delta\tau/2]$ [90]. The same group of parameters ($\gamma = 10^{-6}$, $\epsilon = 0$, $C = 1$) is adopted here. $L = 5$ and SNR = 15 dB.

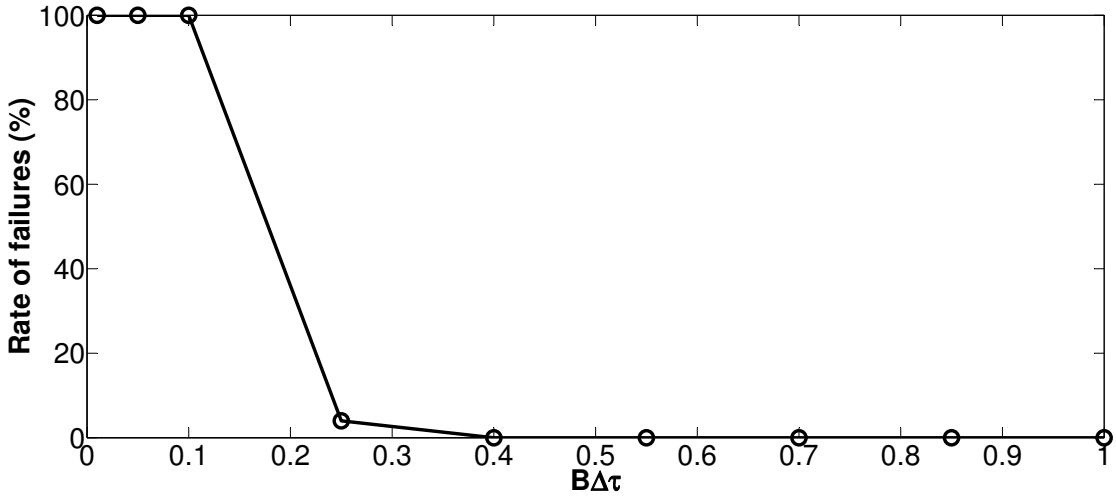

Figure B.6 – Rate of failures using FBLP-SVR with 500 Monte Carlo trials and different thicknesses. $\gamma = 10^{-6}$, $\epsilon = 0$, $C = 1$, $L = 5$ and SNR = 15 dB.

Figure B.6 illustrates the rate of failures of FBLP-SVR for different thicknesses ($B\Delta\tau$). As $B\Delta\tau$ gets larger, i.e., the thickness of Layer 1 gets larger, the rate of failures decreases. The rate of failures reaches 0% when $B\Delta\tau = 0.4$. The proposed FBLP-SVR and the settings of SVR parameters can be used at different thicknesses.

To sum up, the value C controls the trade-off between the model error and the empirical error. Parameter ϵ represents the size of the ϵ-intensive zone, which should not be too large, as shown in Figure B.2. Parameter γ is a small coefficient of an additional regularization term, which is insensitive in our testing. Secondly, the performance of the proposed FBLP-SVR is also analyzed with the same parameter setting ($\gamma = 10^{-6}$, $\epsilon = 0$, $C = 1$) at different numbers of snapshots, different SNRs, and different thicknesses. All the simulations prove the robustness of the proposed FBLP-SVR with the same set of SVR parameters.

C

Wirtinger's calculus and some derivations

C.1 Wirtinger's calculus

Let $g(z)$ be a complex function defined on $\mathbb{C}$, where $z = x + jy$ and j is the imaginary unit. Assume that the partial derivatives of $g(x, y)$, $\frac{\partial g}{\partial x}$ and $\frac{\partial g}{\partial y}$, exist, then the Wirtinger's derivative of function g can be given by:

$$\frac{\partial g}{\partial z} = \frac{1}{2}(\frac{\partial g}{\partial x} - j\frac{\partial g}{\partial y}). \tag{C.1}$$

The conjugate Wirtinger's derivative of g is given by:

$$\frac{\partial g}{\partial z^*} = \frac{1}{2}(\frac{\partial g}{\partial x} + j\frac{\partial g}{\partial y}). \tag{C.2}$$

Wirtinger's calculus can be used to derive gradients of real valued cost functions that are defined in the complex domains [59, 79, 91]. For real-valued functions, the complex gradient is defined as:

$$\nabla g = \frac{\partial g}{\partial z^*}. \tag{C.3}$$

C.2 Derivation of SVR in the complex domain

Since the optimization function of SVR in (4.5) is real-valued, its derivations on the complex vector $\boldsymbol{\omega}_{FBLP}$ can follow the rules of Wirtinger's calculus in (C.3). The partial derivation of L_{pd} with respect to $\boldsymbol{\omega}_{FBLP}$ is deduced in details as follows. Assume $\boldsymbol{\omega}_{FBLP} = \boldsymbol{\omega}_r + j\boldsymbol{\omega}_i$ and the subscripts r and i denote for the real and imaginary parts, respectively.

$$\begin{aligned}
\frac{\partial}{\partial \boldsymbol{\omega}^*_{FBLP}}\|\boldsymbol{\omega}_{FBLP}\|^2 &= \frac{\partial}{\partial \boldsymbol{\omega}^*_{FBLP}}(\boldsymbol{\omega}^H_{FBLP}\boldsymbol{\omega}_{FBLP}) \\
&= \frac{\partial}{\partial \boldsymbol{\omega}^*_{FBLP}}(\boldsymbol{\omega}_r^T\boldsymbol{\omega}_r + \boldsymbol{\omega}_i^T\boldsymbol{\omega}_i) \\
&= \frac{1}{2}[\frac{\partial}{\partial \boldsymbol{\omega}_r}(\boldsymbol{\omega}_r^T\boldsymbol{\omega}_r + \boldsymbol{\omega}_i^T\boldsymbol{\omega}_i) + j\frac{\partial}{\partial \boldsymbol{\omega}_i}(\boldsymbol{\omega}_r^T\boldsymbol{\omega}_r + \boldsymbol{\omega}_i^T\boldsymbol{\omega}_i)] \\
&= \frac{1}{2}(2\boldsymbol{\omega}_r + j2\boldsymbol{\omega}_i) \\
&= \boldsymbol{\omega}_{FBLP}.
\end{aligned} \tag{C.4}$$

$$\begin{aligned}
\frac{\partial}{\partial \boldsymbol{\omega}^*_{FBLP}}\Re(\mathbf{z}_n^H\boldsymbol{\omega}_{FBLP}) &= \frac{\partial}{\partial \boldsymbol{\omega}^*_{FBLP}}\Re((\mathbf{z}_n^r - j\mathbf{z}_n^i)^T(\boldsymbol{\omega}_r + j\boldsymbol{\omega}_i)) \\
&= \frac{\partial}{\partial \boldsymbol{\omega}^*_{FBLP}}((\mathbf{z}_n^r)^T\boldsymbol{\omega}_r + (\mathbf{z}_n^i)^T\boldsymbol{\omega}_i) \\
&= \frac{1}{2}[\frac{\partial}{\partial \boldsymbol{\omega}_r}((\mathbf{z}_n^r)^T\boldsymbol{\omega}_r + (\mathbf{z}_n^i)^T\boldsymbol{\omega}_i) + j\frac{\partial}{\partial \boldsymbol{\omega}_i}((\mathbf{z}_n^r)^T\boldsymbol{\omega}_r + (\mathbf{z}_n^i)^T\boldsymbol{\omega}_i)] \\
&= \frac{1}{2}(\mathbf{z}_n^r + j\mathbf{z}_n^i) \\
&= \frac{1}{2}\mathbf{z}_n.
\end{aligned} \tag{C.5}$$

$$\begin{aligned}
\frac{\partial}{\partial \boldsymbol{\omega}^*_{FBLP}}\Im(\mathbf{z}_n^H\boldsymbol{\omega}_{FBLP}) &= \frac{\partial}{\partial \boldsymbol{\omega}^*_{FBLP}}\Im((\mathbf{z}_n^r - j\mathbf{z}_n^i)^T(\boldsymbol{\omega}_r + j\boldsymbol{\omega}_i)) \\
&= \frac{\partial}{\partial \boldsymbol{\omega}^*_{FBLP}}((\mathbf{z}_n^r)^T\boldsymbol{\omega}_i - (\mathbf{z}_n^i)^T\boldsymbol{\omega}_r) \\
&= \frac{1}{2}[\frac{\partial}{\partial \boldsymbol{\omega}_r}((\mathbf{z}_n^r)^T\boldsymbol{\omega}_i - (\mathbf{z}_n^i)^T\boldsymbol{\omega}_r) + j\frac{\partial}{\partial \boldsymbol{\omega}_i}((\mathbf{z}_n^r)^T\boldsymbol{\omega}_i - (\mathbf{z}_n^i)^T\boldsymbol{\omega}_r)] \\
&= \frac{1}{2}(-\mathbf{z}_n^i + j\mathbf{z}_n^r) \\
&= \frac{j}{2}\mathbf{z}_n.
\end{aligned} \tag{C.6}$$

Finally, we have:

$$\begin{aligned}\frac{\partial L_{pd}}{\partial \boldsymbol{\omega}^*_{FBLP}} &= \frac{1}{2}\boldsymbol{\omega}_{FBLP} - \frac{1}{2}\sum_{n=1}^{N_T} a_n \mathbf{z}_n + \frac{1}{2}\sum_{n=1}^{N_T} \hat{a}_n \mathbf{z}_n - \frac{j}{2}\sum_{n=1}^{N_T} b_n \mathbf{z}_n + \frac{j}{2}\sum_{n=1}^{N_T} \hat{b}_n \mathbf{z}_n \\ &= \frac{1}{2}\boldsymbol{\omega}_{FBLP} - \frac{1}{2}\sum_{n=1}^{N_T} ((a_n - \hat{a}_n) + j(b_n - \hat{b}_n))\mathbf{z}_n \\ &= 0.\end{aligned} \tag{C.7}$$

The derivation result with respect to ω_{FBLP} is summarized in (4.6).

Bibliography

[1] Merrill I Skolnik. Introduction to radar. *Radar Handbook*, 2, 1962. 21

[2] Nadav Levanon. Radar principles. *New York, Wiley-Interscience, 1988, 320 p.*, 1988. 21

[3] T Engin Tuncer and Benjamin Friedlander. *Classical and modern direction-of-arrival estimation*. Academic Press, 2009. 21, 55

[4] Charles Elachi and Jakob J Van Zyl. *Introduction to the physics and techniques of remote sensing*, volume 28. John Wiley & Sons, 2006. 22

[5] Upamanyu Madhow. *Fundamentals of digital communication*. Cambridge University Press, 2008. 22

[6] Stergios Stergiopoulos. *Advanced signal processing handbook: theory and implementation for radar, sonar, and medical imaging real time systems*. CRC press, 2000. 22

[7] David J Daniels. *Ground penetrating radar*. Wiley Online Library, 2004. 22, 69

[8] Andrea Benedetto and Lara Pajewski. *Civil engineering applications of ground penetrating radar*. Springer, 2015. 22, 69

[9] Cédric Le Bastard, Vincent Baltazart, Yide Wang, and Joseph Saillard. Thin-pavement thickness estimation using GPR with high-resolution and superresolution methods. *IEEE Transactions on Geoscience and Remote Sensing*, 45(8): 2511–2519, 2007. 22, 24, 33, 69, 70, 73, 81, 83

[10] Michael Kolawole. *Radar systems, peak detection and tracking*. Elsevier, 2003. 22

[11] Tie-Jun Shan and Thomas Kailath. Adaptive beamforming for coherent signals and interference. *IEEE Transactions on Acoustics, Speech, and Signal Processing*, 33(3): 527–536, 1985. 22

[12] Meng Sun. *Advanced signal processing techniques for GPR by taking into account the interface roughness of a stratified medium*. PhD thesis, Université de Nantes, 2016. 22, 26

[13] Tie-Jun Shan, Mati Wax, and Thomas Kailath. On spatial smoothing for direction-of-arrival estimation of coherent signals. *IEEE Transactions on Acoustics, Speech, and Signal Processing*, 33(4): 806–811, 1985. 24, 25, 26, 39, 55, 87

[14] H Vincent Poor. *An introduction to signal detection and estimation*. Springer Science & Business Media, 2013. 24

[15] Hamid Krim and Mats Viberg. Two decades of array signal processing research: the parametric approach. *IEEE signal processing magazine*, 13(4): 67–94, 1996. 24, 25, 55, 90

[16] Barry D Van Veen and Kevin M Buckley. Beamforming: A versatile approach to spatial filtering. *IEEE assp magazine*, 5(2): 4–24, 1988. 24

[17] Jack Capon. High-resolution frequency-wavenumber spectrum analysis. *Proceedings of the IEEE*, 57(8): 1408–1418, 1969. 25, 35

[18] John Parker Burg. Maximum entropy spectral analysis. In *37th Annual International Meeting, Soc. of Explor. Geophys., Oklahoma City, Okla., Oct. 31, 1967*, 1967. 25

[19] Donald W Tufts and Ramdas Kumaresan. Estimation of frequencies of multiple sinusoids: Making linear prediction perform like maximum likelihood. *Proceedings of the IEEE*, 70(9): 975–989, 1982. 25, 35, 36

[20] S Lawrence Marple and S Lawrence Marple. *Digital spectral analysis: with applications*, volume 5. Prentice-Hall Englewood Cliffs, NJ, 1987. 25

[21] Simon S Haykin. *Adaptive filter theory*. Pearson Education India, 2008. 25, 55

[22] Harry L Van Trees. *Optimum array processing: Part IV of detection, estimation, and modulation theory*. John Wiley & Sons, 2004. 25

[23] Ralph O Schmidt. Multiple emitter location and signal parameter estimation. *IEEE Transactions on Antennas and Propagation*, 34(3): 276–280, 1986. 25

[24] Arthur Barabell. Improving the resolution performance of eigenstructure-based direction-finding algorithms. In *IEEE International Conference on Acoustics, Speech, and Signal Processing ICASSP'83*, volume 8, pages 336–339. IEEE, 1983. 25

[25] Richard Roy and Thomas Kailath. ESPRIT-estimation of signal parameters via rotational invariance techniques. *IEEE Transactions on Acoustics, Speech and Signal Processing*, 37(7): 984–995, 1989. 25

[26] Sylvie Marcos, Alain Marsal, and Messaoud Benidir. The propagator method for source bearing estimation. *Signal processing*, 42(2): 121–138, 1995. 25

[27] Yong Liang Wang, Hui Chen, YN Peng, and Qun Wan. Spatial spectrum estimation theory and algorithm. *Tsinghua University, Beijing*, 2004. 25, 35, 55, 58, 73

[28] Amina El Gonnouni, Manel Martinez-Ramon, José Luis Rojo-Álvarez, Gustavo Camps-Valls, Aníbal Ramón Figueiras-Vidal, and Christos G Christodoulou. A support vector machine MUSIC algorithm. *IEEE Transactions on Antennas and Propagation*, 60(10): 4901–4910, 2012. 25, 28, 58, 71

[29] JE Evans. High resolution angular spectrum estimation technique for terrain scattering analysis and angle of arrival estimation. In *1st IEEE ASSP Workshop Spectral Estimat., McMaster Univ., Hamilton, Ont., Canada, 1981*, pages 134–139, 1981. 26

[30] S Unnikrishna Pillai and Byung Ho Kwon. Forward/backward spatial smoothing techniques for coherent signal identification. *IEEE Transactions on Acoustics, Speech, and Signal Processing*, 37(1): 8–15, 1989. 26, 40, 87

[31] Darel A Linebarger, Ronald D DeGroat, and Eric M Dowling. Efficient direction-finding methods employing forward/backward averaging. *IEEE Transactions on Signal Processing*, 42(8): 2136–2145, 1994. 26

[32] Weixiu Du and Rodney Lynn Kirlin. Improved spatial smoothing techniques for DOA estimation of coherent signals. *IEEE Transactions on signal processing*, 39(5): 1208–1210, 1991. 26

[33] Chongying Qi, Yongliang Wang, Yongshun Zhang, and Ying Han. Spatial difference smoothing for DOA estimation of coherent signals. *IEEE Signal Processing Letters*, 12(11): 800–802, 2005. 26

[34] Jinqiang Wei, Xu Xu, Dawei Luo, and Zhongfu Ye. Sequential DOA estimation method for multi-group coherent signals. *Signal Processing*, 130: 169–174, 2017. 26

[35] Mati Wax and Jacob Sheinvald. Direction finding of coherent signals via spatial smoothing for uniform circular arrays. *IEEE transactions on antennas and propagation*, 42(5): 613–620, 1994. 26

[36] Fang-Ming Han and Xian-Da Zhang. An ESPRIT-like algorithm for coherent DOA estimation. *IEEE Antennas and Wireless Propagation Letters*, 4(1): 443–446, 2005. 26

[37] Zhongfu Ye and Xu Xu. DOA estimation by exploiting the symmetric configuration of uniform linear array. *IEEE Transactions on Antennas and Propagation*, 55(12): 3716–3720, 2007. 26

[38] Y-D Huang and Mourad Barkat. Near-field multiple source localization by passive sensor array. *IEEE Transactions on antennas and propagation*, 39(7): 968–975, 1991. 26, 47, 87

[39] Emmanuele Grosicki, Karim Abed-Meraim, and Yingbo Hua. A weighted linear prediction method for near-field source localization. *IEEE Transactions on Signal Processing*, 53(10): 3651–3660, 2005. 26, 87, 101, 102

[40] Wanjun Zhi and Michael Yan-Wah Chia. Near-field source localization via symmetric subarrays. In *IEEE International Conference on Acoustics, Speech and Signal Processing, ICASSP 2007*, volume 2, pages II–1121. IEEE, 2007. 27, 48, 87

[41] Jian Xie, Haihong Tao, Xuan Rao, and Jia Su. Comments on "near-field source localization via symmetric subarrays". *IEEE Signal Processing Letters*, 22(5): 643–644, 2015. 27, 49

[42] Jin He, MNS Swamy, and M Omair Ahmad. Efficient application of MUSIC algorithm under the coexistence of far-field and near-field sources. *IEEE Transactions on Signal Processing*, 60(4): 2066–2070, 2012. 27, 49, 87

[43] Hongyang He, Yide Wang, and Joseph Saillard. Near-field source localization by using focusing technique. *EURASIP Journal on Advances in Signal Processing*, 2008. 27, 51, 87, 88

[44] Adnan Sahin. *Near field forward scattering, and object-based localization algorithms for subsurface objects*. PhD thesis, Northeastern University Boston, 1998. 27, 87

[45] Simone Meschino, Lara Pajewski, and Giuseppe Schettini. A SAP-DOA method for the localization of two buried objects. *International Journal of Antennas and Propagation*, 2013, 2013. 27, 87

[46] Raghu N Challa and Sanyogita Shamsunder. High-order subspace-based algorithms for passive localization of near-field sources. In *Signals, Systems and Computers, 1995. 1995 Conference Record of the Twenty-Ninth Asilomar Conference on*, volume 2, pages 777–781. IEEE, 1995. 27

[47] Junli Liang and Ding Liu. Passive localization of mixed near-field and far-field sources using two-stage MUSIC algorithm. *IEEE Transactions on Signal Processing*, 58(1): 108–120, 2010. 27

[48] Jianzhong Li. *Investigation on Near-field Source Localization and the Corresponding Applications*. PhD thesis, UNIVERSITE DE NANTES, 2017. 27

[49] Wolfram Pannert. Spatial smoothing for localized correlated sources–its effect on different localization methods in the near-field. *Applied Acoustics*, 72(11): 873–883, 2011. 27

[50] Vladimir Vapnik. *Statistical learning theory. 1998*. Wiley, New York, 1998. 27, 42, 55

[51] Matteo Pastorino and Andrea Randazzo. A smart antenna system for direction of arrival estimation based on a support vector regression. *IEEE Transactions on Antennas and Propagation*, 53(7): 2161–2168, 2005. 28, 40

[52] Matteo Pastorino and Andrea Randazzo. The SVM-based smart antenna for estimation of the directions of arrival of electromagnetic waves. *IEEE transactions on instrumentation and measurement*, 55(6): 1918–1925, 2006. 28, 40, 43

[53] Ruokun Wang, Biyang Wen, and Weimin Huang. A support vector regression-based method for target direction of arrival estimation from HF radar data. *IEEE Geoscience and Remote Sensing Letters*, 2018. 28, 40

[54] Cédric Le Bastard, Yide Wang, Vincent Baltazart, and Xavier Derobert. Time delay and permittivity estimation by ground-penetrating radar with support vector regression. *IEEE Geoscience and Remote Sensing Letters*, 11(4): 873–877, 2014. 28, 40, 43

[55] Cesar C Gaudes, Ignacio Santamaria, Javier Via, Enrique Masgrau Gómez, and Talesa Sese Paules. Robust array beamforming with sidelobe control using support vector machines. *IEEE Transactions on Signal Processing*, 55(2): 574–584, 2007. 28, 56

[56] Nan Xu. *Applications of support vector machines in electromagnetic problems*. PhD thesis, 2011. 28, 70

[57] José Luis Rojo-Álvarez, Gustavo Camps-Valls, Manel Martínez-Ramón, Emilio Soria-Olivas, A Navia-Vázquez, and Aníbal R Figueiras-Vidal. Support vector machines framework for linear signal processing. *Signal Processing*, 85(12): 2316–2326, 2005. 28, 70

[58] José Luis Rojo-Álvarez, Manel Martínez-Ramón, Mario de Prado-Cumplido, Antonio Artés-Rodríguez, and Aníbal R Figueiras-Vidal. Support vector method for robust

ARMA system identification. *IEEE transactions on signal processing*, 52(1): 155–164, 2004. 28, 55, 70

[59] Pantelis Bouboulis, Sergios Theodoridis, Charalampos Mavroforakis, and Leoni Evaggelatou-Dalla. Complex support vector machines for regression and quaternary classification. *IEEE transactions on neural networks and learning systems*, 26(6): 1260–1274, 2015. 28, 70, 71, 72, 109

[60] Jingjing Pan, Yide Wang, Cédric Le Bastard, and Tianzhen Wang. DOA finding with support vector regression based forward–backward linear prediction. *Sensors*, 17(6): 1225, 2017. 29, 30

[61] Jingjing Pan, Cédric Le Bastard, Yide Wang, and Meng Sun. Time-delay estimation using ground-penetrating radar with a support vector regression-based linear prediction method. *IEEE Transactions on Geoscience and Remote Sensing*, 2018. 29, 30

[62] Lele Qu, Qiang Sun, Tianhong Yang, Lili Zhang, and Yanpeng Sun. Time-delay estimation for ground penetrating radar using ESPRIT with improved spatial smoothingtechnique. *IEEE Geoscience and remote sensing letters*, 11(8): 1315–1319, 2014. 33

[63] Jian Li and Renbiao Wu. An efficient algorithm for time delay estimation. *IEEE Transactions on Signal Processing*, 46(8): 2231–2235, 1998. 33

[64] Alex J Smola and Bernhard Schölkopf. A tutorial on support vector regression. *Statistics and computing*, 14(3): 199–222, 2004. 42

[65] Manel Martínez-Ramón and Christos Christodoulou. Support vector machines for antenna array processing and electromagnetics. *Synthesis Lectures on Computational Electromagnetics*, 1(1): 1–120, 2005. 43, 55, 71

[66] Ilan Ziskind and Mati Wax. Maximum likelihood localization of multiple sources by alternating projection. *IEEE Transactions on Acoustics, Speech, and Signal Processing*, 36(10): 1553–1560, 1988. 46

[67] Yuexian Wang, Matthew Trinkle, and Brian W-H Ng. DOA estimation under unknown mutual coupling and multipath with improved effective array aperture. *Sensors*, 15(12): 30856–30869, 2015. 55, 63

[68] Jingmin Xin and A Sane. Linear prediction approach to direction estimation of cyclostationary signals in multipath environment. *IEEE Transactions on Signal Processing*, 49(4): 710–720, 2001. 55

[69] Yuan-Hwang Chen and Ching-Tai Chiang. Kalman-based spatial domain forward-backward linear predictor for DOA estimation. *IEEE transactions on aerospace and electronic systems*, 31(1): 474–479, 1995. 56

[70] Petre Stoica, Erik G Larsson, and Alex B Gershman. The stochastic crb for array processing: A textbook derivation. *IEEE Signal Processing Letters*, 8(5): 148–150, 2001. 63, 101

[71] Jianzhong Li, Cédric Le Bastard, Yide Wang, Gang Wei, Biyun Ma, and Meng Sun. Enhanced gpr signal for layered media time-delay estimation in low-SNR scenario. *IEEE Geoscience and Remote Sensing Letters*, 13(3): 299–303, 2016. 69

[72] Meng Sun, Cédric Le Bastard, Yide Wang, and Nicolas Pinel. Time-delay estimation using ESPRIT with extended improved spatial smoothing techniques for radar signals. *IEEE Geoscience and Remote Sensing Letters*, 13(1): 73–77, 2016. 69, 75, 81, 83

[73] Iraklis Giannakis, Antonios Giannopoulos, and Craig Warren. A realistic FDTD numerical modeling framework of ground penetrating radar for landmine detection. *IEEE Journal of Selected Topics in Applied Earth Observations and Remote Sensing*, 9(1): 37–51, 2016. 69

[74] Piet van Genderen and Ioan Nicolaescu. Imaging of stepped frequency continuous wave GPR data using the Yule-Walker parametric method. In *Radar Conference, 2005. EURAD 2005. European*, pages 77–80. IEEE, 2005. 69, 70

[75] KC Ho and Paul D Gader. A linear prediction land mine detection algorithm for hand held ground penetrating radar. *IEEE transactions on geoscience and remote sensing*, 40(6): 1374–1384, 2002. 69

[76] Ahmet Burak Yoldemir and Mehmet Sezgin. Adaptive linear prediction based buried object detection with varying detector height. In *13th International Conference on Ground Penetrating Radar (GPR)*, pages 1–4. IEEE, 2010. 69

[77] Christopher R Ratto, Kenneth D Morton, Leslie M Collins, and Peter A Torrione. Analysis of linear prediction for soil characterization in GPR data for countermine applications. *Sensing and Imaging*, 15(1): 86, 2014. 69

[78] Christopher Ratto, Peter Torrione, and Leslie Collins. Estimation of soil permittivity through autoregressive modeling of time-domain ground-penetrating radar data. In *IEEE International Conference on Wireless Information Technology and Systems (ICWITS)* , pages 1–4. IEEE, 2010. 70

[79] Pantelis Bouboulis and Sergios Theodoridis. Extension of Wirtinger's calculus to reproducing kernel Hilbert spaces and the complex kernel LMS. *IEEE Transactions on Signal Processing*, 59(3): 964–978, 2011. 70, 72, 109

[80] J-M Simonin, Vincent Baltazart, Cédric Le Bastard, and Xavier Derobert. Progress in monitoring the debonding within pavement structures during accelerated pavement testing on the fatigue carousel. In *8th RILEM International Conference on Mechanisms of Cracking and Debonding in Pavements*, pages 749–755. Springer, 2016. 83

[81] Shuo Xu, Xin An, Xiaodong Qiao, Lijun Zhu, and Lin Li. Multi-output least-squares support vector regression machines. *Pattern Recognition Letters*, 34(9): 1078–1084, 2013. 98

[82] Piya Pal and PP Vaidyanathan. Nested arrays: A novel approach to array processing with enhanced degrees of freedom. *IEEE Transactions on Signal Processing*, 58(8): 4167–4181, 2010. 98

[83] Palghat P Vaidyanathan and Piya Pal. Sparse sensing with co-prime samplers and arrays. *IEEE Transactions on Signal Processing*, 59(2): 573–586, 2011. 98

[84] Steven M Kay. Fundamentals of statistical signal processing, volume I: estimation theory. 1993. 101

[85] Petre Stoica and Arye Nehorai. Performance study of conditional and unconditional direction-of-arrival estimation. *IEEE Transactions on Acoustics, Speech, and Signal Processing*, 38(10): 1783–1795, 1990. 101

[86] Vladimir Cherkassky and Yunqian Ma. Practical selection of SVM parameters and noise estimation for SVM regression. *Neural networks*, 17(1): 113–126, 2004. 103

[87] Chih-Wei Hsu, Chih-Chung Chang, Chih-Jen Lin, et al. A practical guide to support vector classification. 2003. 103

[88] Shih-Wei Lin, Kuo-Ching Ying, Shih-Chieh Chen, and Zne-Jung Lee. Particle swarm optimization for parameter determination and feature selection of support vector machines. *Expert systems with applications*, 35(4): 1817–1824, 2008. 103

[89] Olivier Chapelle, Vladimir Vapnik, Olivier Bousquet, and Sayan Mukherjee. Choosing multiple parameters for support vector machines. *Machine learning*, 46(1-3): 131–159, 2002. 103

[90] Cédric Le Bastard, Yide Wang, and Vincent Baltazart. Algorithmes haute résolution linéaires pour l'estimation des temps de retard dans un contexte de bruit quelconque. 2008. 108

[91] Songchuan Zhang, Youshen Xia, and Weixing Zheng. A complex-valued neural dynamical optimization approach and its stability analysis. *Neural Networks*, 61: 59–67, 2015. 109

UNIVERSITE BRETAGNE LOIRE / MATHSTIC

UNIVERSITÉ DE NANTES

Titre : Estimation des temps de retard et localisation de sources avec des systèmes Radar

Mots clés : Localisation de sources, estimation des temps de retard, sources cohérentes, radar, méthode de régression à base de vecteur support

Résumé : La localisation de sources (en champ lointain ou en champ proche) et l'estimation des temps de retard ont de nombreuses applications pratiques. Pour localiser une source en champ lointain à partir d'un réseau de capteur, seule la direction d'arrivée (DDA) de la source est nécessaire. Quand les sources se situent dans une situation de champ proche, le front d'onde du signal est sphérique et deux paramètres sont nécessaires pour localiser les sources : la direction d'arrivée et la distance entre la source et le réseau de capteurs. Dans cette thèse, on se focalise sur la localisation de sources (en champ lointain et en champ proche) ainsi sur l'estimation des temps de retard dans le contexte où les signaux sont cohérents, mélangés et avec un faible nombre de réalisation.

Tout d'abord, nous proposons de combiner la théorie de la méthode SVR (Support vector regression qui est une méthode de régression à base d'apprentissage supervisée) avec la théorie de la prédiction linéaire avant-arrière. La méthode proposée, appelée FBLP-SVR, est développée pour deux applications : la localisation de sources en champ lointain et l'estimation des temps de retard des échos radar en champ lointain. La méthode développée est évaluée par des simulations et des expérimentations. Nous proposons également une méthode de localisation de sources en champ proche dans le contexte où les signaux sont cohérents et mélangés. La méthode proposée est basée sur une technique de focalisation, de moyennage en sous-bande et sur une méthode à sous-espaces pour l'estimation des DDAs. Ensuite, les distances entre les sources et le réseau de capteur sont estimées avec la méthode du maximum de vraisemblance.

Title : Time-delay estimation and source localization in radar systems

Keywords : Source localization, time-delay estimation, coherent sources, radar, support vector regression

Abstract : Source localization (in far-field or in near-field) and time-delay estimation have many practical applications. To locate a far-field source from a sensor array, only the direction of arrival (DOA) of the source is necessary. When the sources are in a near-field situation, the wavefront of the signal is spherical and two parameters are needed to locate the sources: the direction of arrival and the distance between the source and the sensors. In this thesis, we focus on the localization of sources (both in far-field and near-field) as well as the estimation of time-delay in the context where the signals are coherent, overlapped and with a small number of snapshots.

First, we propose to combine the theory of the SVR method (support vector regression, which is a supervised learning-based regression method) with the theory of forward-backward linear prediction (FBLP). The proposed method, called FBLP-SVR, is developed for two applications: far-field source localization and time-delay estimation by using ground penetrating radar. The proposed method is evaluated by simulations and experiments. We also propose a near-field source localization method in the context where the signals are coherent and overlapped. The proposed method is based on a focusing technique, a spatial smoothing preprocessing, and a subspace method in the estimation of DOA. Then, the distances between the sources and sensors are estimated with the maximum likelihood method.